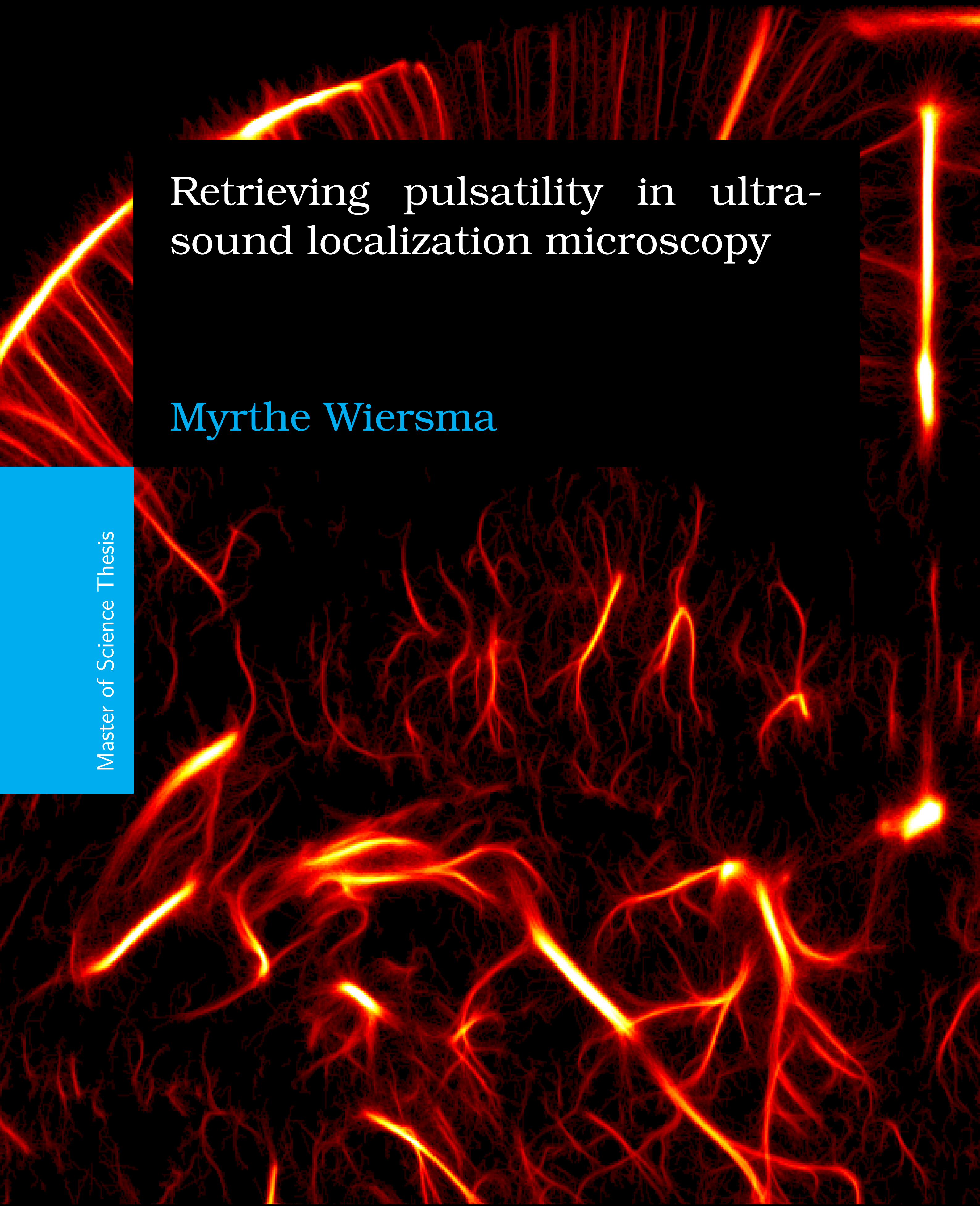

Retrieving pulsatility in ultrasound localization microscopy

Myrthe Wiersma

Master of Science Thesis

Delft Center for Systems and Control

Retrieving pulsatility in ultrasound localization microscopy

MASTER OF SCIENCE THESIS

For the degree of Master of Science in Systems and Control at Delft
University of Technology

Myrthe Wiersma

May 6, 2022

Faculty of Mechanical, Maritime and Materials Engineering (3mE) · Delft University of
Technology

The cover image was constructed from data of an *in vivo* ULM acquisition of the rat brain by [1].

Copyright © Delft Center for Systems and Control (DCSC)
All rights reserved.

Delft University of Technology
Department of
Delft Center for Systems and Control (dcsc)

The undersigned hereby certify that they have read and recommend to the Faculty of Mechanical, Maritime and Materials Engineering (3mE) for acceptance a thesis entitled

Retrieving pulsatility in ultrasound localization microscopy

by

Myrthe Wiersma

in partial fulfillment of the requirements for the degree of

Master of Science Systems and Control

Dated: May 6, 2022

Supervisor(s):

dr. C.S. Smith

dr. D. Maresca

Reader(s):

dr. R. van de Plas

dr. G. Verbiest

Abstract

The resolution of conventional ultrasound imaging is fundamentally limited by wave diffraction. Ultrasound localization microscopy (ULM) is a vascular imaging method capable of retrieving a 10-fold improvement of resolution compared to the classical diffraction limit. It relies on the detection, localization, and tracking of intervascular injected synthetic microbubbles (MB) of sub-wavelength size. The localization of sparse MBs with sub-wavelength precision is the key factor enabling super-resolution in ULM. Blood flow velocity measurements are obtained by tracking the MBs over consecutive frames. As a result, tracked MBs act as moving blood flow sensors. Super resolved images of the microvasculature and its average bloodflow are recovered by accumulating the MB tracks on a fine grid. Because typical ULM acquisitions accumulate large numbers of MB tracks over hundreds of cardiac cycles, transient hemodynamic variations such as pulsatility get averaged out. Here we introduce two independent processing methods that leverage the high temporal sampling of MB tracks to retrieve pulsatility in ULM data. The first method relies on filtering single track velocity measurements to reduce the presence of noise resulting from MB localization error. This method was shown able to recover the blood flow velocity over a pulsatile cycle. The pulsatility fraction, defined as the relative velocity deviation during a pulsatile cycle, was successfully retrieved with a root mean squared error (RMSE) of 3.3% in simulated data. The second reported method is based on the accumulation of velocity measurements by a stationary observer. From theoretical derivation, it was found that pulsatility leads to bimodality in the velocity distribution, which was only observed for sufficient localization precision. We showed that the pulsatility fraction can be retrieved from the location of the two velocity distribution peaks, which correspond to the maximum and minimum velocity during a pulsatile cycle. The method was validated in simulation resulting in a pulsatility fraction estimation with an error of 5.2%. Together, our results show that MB track data contains more information on the hemodynamics of the blood flow than is represented by conventional ULM image reconstruction.

Keywords: *ultrasound localization microscopy, pulsatility, localization precision, velocity distribution*

Table of Contents

Acknowledgements **xiii**

1 Introduction **1**
- 1-1 Ultrasound imaging . . . 2
  - 1-1-1 Ultrasound waves . . . 2
  - 1-1-2 Tissue interaction . . . 3
  - 1-1-3 Image formation . . . 6
  - 1-1-4 Spatial resolution . . . 9
  - 1-1-5 Temporal resolution . . . 10
- 1-2 Ultrasound localization microscopy . . . 11
  - 1-2-1 Introduction to the technique . . . 11
  - 1-2-2 Spatial resolution . . . 13
  - 1-2-3 Temporal resolution . . . 14
- 1-3 Thesis motivation . . . 14
- 1-4 Outline . . . 15

2 Ultrasound localization microscopy image processing **17**
- 2-1 Detection . . . 18
  - 2-1-1 Retrieval of microbubble signal . . . 18
  - 2-1-2 Extraction of regions of interest . . . 21
- 2-2 Localization . . . 21
  - 2-2-1 Peak detection . . . 21
  - 2-2-2 Weighted average . . . 22
  - 2-2-3 Gaussian fitting . . . 22
  - 2-2-4 Radial symmetry . . . 22
- 2-3 Tracking . . . 23
  - 2-3-1 Local search methods . . . 23

2-3-2 Combinatorial methods 24
2-4 Rendering 26
2-4-1 Trajectory smoothing 26
2-4-2 Spatial interpolation 27
2-4-3 Density reconstruction 27
2-4-4 Velocity reconstruction 27
2-5 Motion correction 28

3 Retrieving pulsatility in ultrasound localization microscopy 29
3-1 Introduction 30
3-2 Methods 30
3-2-1 Ultrasound localization microscopy simulator design 31
3-2-2 Pulsatility retrieval methods 32
3-3 Results 34
3-3-1 Simulated ultrasound localization microscopy reconstructions 34
3-3-2 Method I: filtered single-track velocities 34
3-3-3 Method II: velocity distribution 34
3-4 Discussion 36
3-5 Conclusion 38
3-6 Backmatter and appendices 39

4 Conclusion 45
4-1 Summary 45
4-2 Discussion 46
4-3 Outlook 47

A The womersley solution for pulsatile flow in rigid pipes 49

B Conversion between RMSE and σ 55

Bibliography 57

Glossary 63
List of Acronyms 63
List of Symbols 63

List of Figures

1-1 Two brain images reported with an interval of nearly 80 years. (a) Dussik's "hyperphonogram", the first reported ultrasound image of the body (1942). A sagittal slice of the human brain was imaged through a transcranial acquisition. From [2] (b) An ultrasound localization microscopy reconstruction of a coronal slice of the rat brain (2018). Positive and negative blood flow velocities u represent up- and downwards direction. From [3] 1

1-2 The pulse-echo principle is found both in nature and technical applications. The surroundings are perceived by transmitting a pulse and capturing echoes resulting from object interactions. (a) Dolphins apply the pulse-echo principle for echolocation of their prey. Obtained from https://navalunderseamuseum.org (b) In ultrasound imaging the pulse-echo principles is utilized to image internal tissue structures. Lines represent the wavefront. 2

1-3 Illustration of the transmitted wave and its tissue interactions in ultrasound imaging. (a) Two types of acoustic waves. Particles vibrating in longitudinal or transverse direction w.r.t. the direction of propagation for respectively compressional and shear waves. (b) The ultrasound transducer consists of multiple piezo electric elements. By firing the elements in a delay pattern, transmit pulses of arbitrary shape can be constructed. (c) Specular reflection occurs when an incident wave of pressure p_i encounters a smooth interface. Part of the pressure is reflected (p_r) and the remainder is transmitted (p_t). θ_i=θ_r. (d) Diffuse reflection occurs when an incident wave encounters a rough interface. (e) Rayleigh scattering by a small particle results in a sperical echo of pressure p_s. 4

1-4 An illustration of the ultrasound data acquisition process in successive steps. (a) The ultrasonic probe emits a plane wave pulse, depicted by lines of equal phase (blue), by firing the piezo-electric transducer elements simultaneously. Two scatterers are located in the homogeneous tissue. (b) The transmit beam travels in z-direction through the tissue and encounters a scatterer (orange dot). (c) Rayleigh scattering of the first scatterer. (d) The echo (red) arrives at the probe and is detected by the yellow element. (e) Due to a difference in TOF the echo is detected by the elements in an hyperbolic shape. 7

1-5 Finding the pixel intensity of the pixel centered around (x, z). The beamforming grid is overlayed in gray. (a) A plane wave (blue) at an angle α travels a distance d_{TX} towards the pixel center. The resulting echo resulting from scatterers within the pixel travels a distance d_{RX} back to transducer element i. (b) An illustration of DAS beamforming to retrieve the pixel intensity from the recorded RF signal. Due to a difference in d_{RX} the echo reaches the transducer elements (gray) in a hyperbolic shape. IQ demodulation is applied to find the complex envelope of the transducer signal. At the appropriate delay, the values of the IQ demodulated signals are read out and added to find the pixel intensity. 8

1-6 The point spread function (PSF) shows the blurring caused by diffraction. (a) Simulated image of the PSF, created by simulating a point scatterer (black cross) located at (0.25,0.25) mm expressed in the local coordinates of the extracted patch. Transmit frequency $f = 17.86$ MHz, wavelength $\lambda = 86.2$ μm, $\#f = 1$, beamformed pixel size $dx = 10$ μm. (b) The cross-section of the PSF along $z = 0.25$mm. Dotted line gives the location of its peak. 9

1-7 Objects closer than the Rayleigh resolution limit can not be individually distinguished. Here $R = 105$ μm (a-c) Simulated B-mode images of two point scatterers (black cross) with separation distances of respectively: 100 μm, 110 μm and 120 μm. Transmit frequency $f = 17.86$ MHz, wavelength $\lambda = 86.2$ μm, f-number $= 1$, beamformed pixel size $dx = 10$ μm. (d-f) Pixel intensity values along the line $z = 0.4$mm. 10

1-8 Individual ultrasound imaging of point scatterers. (a)-(c) Ultrasound simulations of three scenarios respectively: two scatterers at 0.36 mm and 0.46 mm, a single scatterer at 0.36 mm, a single scatterer at 0.46 mm. Transmit frequency f =17.86MHz, wavelength $\lambda = 86.2$ μm,f-number= 1. Simulation created on a 10 μm grid. (d)-(f) The pixel intensity values along the line $z = 0.4$mm. The dotted line gives the x value at which the maximum is achieved. 11

1-9 The process of creating a ULM reconstruction from input B-mode frames visualized. During a ULM acquisition, microbubbles (MB) are injected in the vasculature and a large number of B-mode frames is acquired over time. Static tissue signal is filtered out, resulting in MB frames that highlight the nonlinear image contribution of the microbubbles. MB events are detected and localized with sub-wavelength precision. The temporal dimension is collapsed by linking estimated MB positions over consecutive frames. The MB tracks are accumulated to find the ULM reconstruction. In the ULM density map displayed here vessels of diameter far below the wavelength can be distinguished. Scalebar: $\lambda = 102$ μm. Data from [4]. . . . 13

2-1 A detailed depiction of the ultrasound localization microscopy processing pipeline. Input are the B-mode frames $I(x, z, n)$. The outputted super resolved reconstruction can be either a density map, a velocity map or a flow orientation map. The main four steps are: detection, localization, tracking and rendering. The motion correction processing step is optional. 18

2-2 The input B-mode images are reorganized into the spatiotemporal Casorati matrix S. Each B-mode frame corresponds to one column in S. N_z, N_z and N_f are the number of pixels in z, the number of pixel in x and the number of B-mode frames of the inputted set. Data from [4]. 19

2-3 The PI and AM techniques are capable of isolating the nonlinear MB response by altering the imaging sequence. A sequence of transmit pulses are utilized (blue). From the recombination of the measured echo signals (red) the nonlinear part of the echo signal can be retrieved (orange). The resulting nonlinear part is beamformed to $I_{MB}(x, z, n)$ 21

2-4 An illustration of localization algorithms commonly used in ULM. (a) Peak detection method without interpolation. (b) Peak detection method with Lanczos interpolation. (c) Weighted average method. (d) 2D Gaussian fitting. (e) Radial symmetry method. 22

2-5 The MB tracking problem visualized. (a) MB tracking is performed by linking MB positions of consecutive frames. (b) In local search methods the linking is performed one-by-one. For each MB position in frame $n-1$ a close MB position in the next frame is sought. (c) Combinatorial methods rely on linking the MBs frame-to-frame. The linking of all MB positions of two consecutive frames is considered at the same time allowing to find a solution that minimizes the total linking cost. C_{ij} denotes the cost of linking node i of frame $n-1$ to node j of frame n. 24

2-6 The rendering of MB trajectories consists of three steps: smoothing, interpolation and accumulation. (a) A MB trajectory is formed by linking localizations of consecutive frames. The maximum linking distance is applied at this stage in the process. From the found track, raw velocity measurements $v_{\mathrm{R}}(n)$ are obtained. (b) Smoothing of the trajectory by a moving average filter of span $s=3$. (c) Spatial interpolation of the trajectory results in additional data points (red dot). (d) From the accumulation of all trajectories super resolved ULM reconstructions can be found. 26

3-1 Simulation study pipeline. (a) Our simulator enabled two simulation scenarios: Localization and No-Localization. (b) Simulated ground truth flow $u_n^{\mathrm{GT}}(0)$ at the centerline ($r=0$) for three values of P_f and a pulsatility frequency of 5 Hz. Flow profiles extracted from [5]. (c) A rigid vessel with a parabolic flow profile is assumed. r and l are respectively the axial and lateral coordinates. Flow is independent of l. (d) Two steps of US simulation: first the point spread functions (PSF) of the MBs are simulated. Second, a B-mode image is generated by adding speckle. Estimation of the MB position in a region of interest (ROI). The ground truth MB position (x,z) and the estimated position $(\hat{x},\hat{z})$ are given by the black and red cross respectivel. (e) In the No-Localization scenario a localization error $(\Delta x, \Delta z)$ is sampled from two normal distributions and added to the ground truth MB position (x,z) to obtain the estimated MB position $(\hat{x},\hat{z})$. Localization precision σ is controlled. (f) The double vessel and single vessel configurations showing a vein (blue) and arteries (red). Simulation parameters in Table 3-1. The local coordinates are defined at the inlet of the vessel. The vessel orientation angle θ is defined with respect to the x-axis in the counter clockwise direction. 31

3-2 Pulsatility retrieval method based on the accumulation of velocity measurements. (a) For derivation purposes, the steady-state and pulsatile flow case were considered. In the former the flow $u^{\mathrm{GTss}}(r)$ is independent of the time index n. (b) Illustration of two MB positions l_n and l_{n-1} localized with localization errors Δl_n and Δl_{n-1} respectively. Only the localization error along the axial coordinate l is considered. (c) Derivation of the distribution U^{f}. The distribution U^{GTf} is found by the histogram of the smoothed ground truth flow $u_n^{\mathrm{GTf}}(0)$ at the centerline of the vessel. By convolution with the smoothed velocity error distribution ΔU^{f} we derive U^{f}. Here, the derivation is performed for the single vessel configuration for three different values of P_f and with $\sigma = 5$ μm and $s=21$. The maximum and minimum flow can be detected by the peaks in U^{f}. 33

3-3 Simulation of the double vessel configuration with the designed ULM simulator shows its ability to simulate the full ULM processing pipeline and achieve super-resolution. Length of all scalebars $= \lambda$ (a) The simulated average bloodflow $\bar{u}_n^{\mathrm{GT}}(r)$ serves as the ground truth with which the ULM velocity map is to be compared. (b) A patch of a simulated B-mode image with 3 MBs at position (x, z) beamformed at 50 μm $\approx \lambda/2$. In the regions of interest, the MB position estimates $(\hat{x}, \hat{z})$ are found using the radial symmetry localization algorithm. (c) Diffraction-limited Power Doppler rendering with cross- sections 1,2 and 3 at which the vessels have a separation distance of respectively 45, 30 and 15 μm. (d) ULM density rendering. (e) ULM velocity rendering. (f) ULM orientation rendering. (g) Cross-sections (1)-(3) of the ULM density rendering and Power Doppler image. (h) Cross-sections (4)-(6) of the ULM velocity rendering (i) Histograms for measured localization errors Δx and Δz for a total of 29417 localized MBs. 35

3-4 Pulsatility can be retrieved by filtering single-track velocity measurements. (a)-(b) Three tracks at different lateral positions r_1, r_2, and r_3 in the two vessels are highlighted. Scalebar $= \lambda$ (c) The smoothed velocity measurements at r_2 show a periodical disturbance. (d) The frequency spectrum of the raw velocity measurements at r_2 shows a peak at frequencies corresponding to the frequency range f_{dx} (grey). (e) The frequency filtered velocity measurements $u_n^{\mathrm{f}}(r)$ follow the simulated ground truth velocity $u_n^{\mathrm{GT}}(r)$. Multiple tracks for each lateral location are shown. (f) From the filtered measurements of (e) P_f is estimated. 36

3-5 Pulsatility fraction can be retrieved from the bimodal shape of the velocity distribution. The results shown here correspond to the parameters of the single vessel configuration. (a) The derived velocity distributions for different values of σ with fixed $s = 21$. $\hat{P}_f$ can be found from the location of the two peaks in the distribution. Centroids of the distribution are given by asterisks and represent the conventional ULM measurement. (b)-(c) Similar derivation for $P_f = 0.2$ and $P_f = 0$ respectively. (d) The derivation of (a) was repeated for $s = 51$. (e) The effect of localization precision σ on $\hat{P}_f$ for fixed s. The line stops when no two peaks could be detected. (f) The effect of s on $\hat{P}_f$ for a fixed σ. The different lines correspond to different σ values. A maximum (cross) can be found corresponding to the optimal value of s. Derivation was performed up to $s = 51$. 37

3-6 Validation of the velocity distribution pulsatility retrieval method in simulation. (a) The histograms were constructed by collecting velocity measurements along the centerline of the vessel in the single vessel configuration for the No-Localization scenario. The theoretical location of the peak was extracted from derived U^{f} of Fig. 3-5(a). Bin size $= 0.5$ mm/s. (b) The acquired histograms for the double-vessel configuration with Localization. The same data set as in Fig. 3-4 was used. Bin size $= 0.1$ mm/s. 38

3-7 The periodical grid-based artifact found in single-track velocity measurements is not eliminated by increasing the span s (in number of frames). The smoothed velocity values of $s = 111$ still show the artifact while their shape is heavily altered by the heavy smoothing, resembling the effect shown in Fig. 3-10(a). 41

3-8 The frequency spectra of the raw single-track velocity measurements $u_n(r)$ are shown for simulations in which beamforming was perfomed on different pixel sizes dx. f_{dx} corresponds to the range of frequencies at which a MB passes a pixel. In the top row with $dx = 100$ μm, peaks lie within the frequency range f_{dx} for localization performed with a radial symmetry algorithm and with Gaussian fitting. In the bottom row a peak is visible in the f_{dx} range for $dx = 50$ μm. For $dx = 10$ μm $\sim$ $1/10\lambda$ the frequency range was not found to align with a distinct peak in the spectrum. On the right an illustration of the grid-based artifact is included. The distance between the estimated MB positions $(\hat{x}, \hat{z})$ is dependent on the ground truth MB location within (x, z) a beamformed pixel. 41

3-9 The grid-based artifact in a PSF simulation without speckle and without application of a SVD filter. (a) The frequency spectrum shows a peak corresponding with the f_{dx} region. Additionally, an increase in frequency content is found at $\sim 2f_{dx}$. (b) The track velocity measurements smoothed by a moving average filter with a span of 51 frames. A clear sawtooth-like behavior is found. 42

3-10 The span of the moving average filter has a large influence on the obtained distribution u^{f}. (a) The simulated ground truth pulsatile cycle $(s = 1)$ is smoothed for different values of the span s. A full cycle (200 frames) is displayed here. (b) The histograms of U^{GTf} change shape for different value of s. (c) The velocity error distribution ΔU^{f} narrows for increased span. The scenario of $\sigma = 20$ μm is derived here. The width of ΔU^{f} for the non smoothed case (black) extends far outside of the interval given here. (d) The resulting velocity distribution U^{f} from the convolution of the results of (b) and (c). The two peaks are barely noticable for $s = 21$. Increasing the span to $s = 51$ improves the retrieval of the two peaks. The peaks move inwards with increasing s. 42

3-11 For specific scenarios the pulsatility fraction P_f can have an effect on the RMSE of the ULM velocity reconstruction. (a) Velocity RMSE and the fraction of tracked MBs is plotted against the localization precision σ for different simulated values of P_f. Left and right differ on the value of the maximum linking distance (ULM) used in ULM processing. A shaded area was added to indicate the 95% confidence interval as found from 1000 bootstrapped samples. (b) The non-smoothed velocity distribution U for three values of P_f and $\sigma = 5$ μm is shown. The MLD of 25 μm truncates the distributions at 25 mm/s causing the centroids of the distributions to shift to the left. The average velocity of the truncated distribution as measured in a ULM reconstruction is given in the legend for the different P_f. 43

3-12 Violin plots displaying the spread in reconstructed velocities along a cross-section of a 100 μm vessel. A total of 2000 cross-sections of ULM velocity reconstructions were acquired to construct the violins. The colorbars below show the average number of MBs that passed that lateral location in the vessel. In all six cross-sections a localization precision of 5 μm was simulated. P_f varies along the columns and the two rows show the results for MLD = 25 μm and 50 μm. Median velocities obtained at the centerline for MLD= 25 μm and $P_f = 0$, 0.2 and 0.4 are respectively 18.69, 17.95 and 16.90 mm/s. 44

A-1 Illustration of the difference between pulsatile flow in rigid and elastic vessels. (a) Cylindrical coordinates in a blood vessel with the flow velocities u and v in the axial and lateral direction respectively. (b) Fully developed axisymmetrical flow in a rigid vessel. The velocity profile is constant along l, even for time varying pressure gradient. (c) In a vessel with elastic walls, the velocity profiles vary along the vessel for changing pressure gradient in time. 50

List of Tables

1-1 Comparison between ULM and SMLM 12

3-1 Simulation configuration parameters 32
3-2 List of Symbols 40
3-3 US simulation parameters 40
3-4 ULM processing parameters 40
3-5 Hardware specifications 41

Acknowledgements

With this thesis, I conclude my time as a student at the TU Delft. It has been both an exciting and challenging year in which I have had support from various people. First of all, I would like to thank my entire team of supervisors Carlas Smith, David Maresca, Baptiste Heiles, and Dylan Kalisvaart. Little over a year ago, the project started with a lively discussion between Carlas and myself exploring optional research directions. Your enthusiasm struck me from day one and helped me during several stages of the project, thank you for that.

I want to thank David for his endless positivism and the kindness with which he welcomed me into the lab. You are great at facilitating a pleasant working environment. I have really felt part of the team.

Furthermore, I want to thank Baptiste for always being available to help me. We have had some frustrating moments, in which all we touched on the lab computer decided to crash. Luckily you could always find a way to joke about it. Especially during the last months of my thesis, we have had interesting discussions, which really helped shaping my research.

Last but not least, I would like to thank Dylan for all our regular monday morning meetings. You were of great support during my entire graduation process. In our often lengthy discussions (I guess we have that in common) there was always room to discuss more than only science. Additionally, your detailed feedback on my work helped me to deliver my best.

In addition, I would like to thank my family and friends. Quinten, you have been a constant factor of love and moral support for me, even at times you were thousands of kilometers away. Missing you was challenging at times, but I think we all understand that the Suez canal does not unclog itself! I would like to thank all my roommates for all the coffee walks, long conversations, hard study sessions, parties, and all the fun that we had together over the last few years. You have a talent for always finding a reason to celebrate!

Finally, I would like to thank my family for all their love and support. I am instantly relaxed when being around you and your humor has brought me lots of joy! I look forward to the coming years and all the new memories we will make together.

Rotterdam
May 6, 2022

Myrthe Wiersma

“De gestage drup holt de steen.”

Chapter 1

Introduction

Ultrasound imaging is currently one of the dominant imaging modalities used in diagnostic medicine [6]. By transmitting ultrasonic acoustic waves into the tissue and recording the backscattered echoes, it is capable of real-time imaging of deep-lying internal tissue structures in a noninvasive way and without making use of harmful radiation [7]. The first ultrasound image of the body was reported in 1942 by Dr Karl Dussik. Together with his brother he created the transcranial image displayed in Figure 1-1(a) and named it a "hyperphonogram" [6]. Their transducer measurement were read out through optically recording the light intensity of a connected light bulb that shined proportional to the transducer signal [6]. Comparison with the ultrasound localization microscopy image of the rat brain in Figure 1-1(b) illustrates the enormous advances in medical ultrasound imaging since 1942.

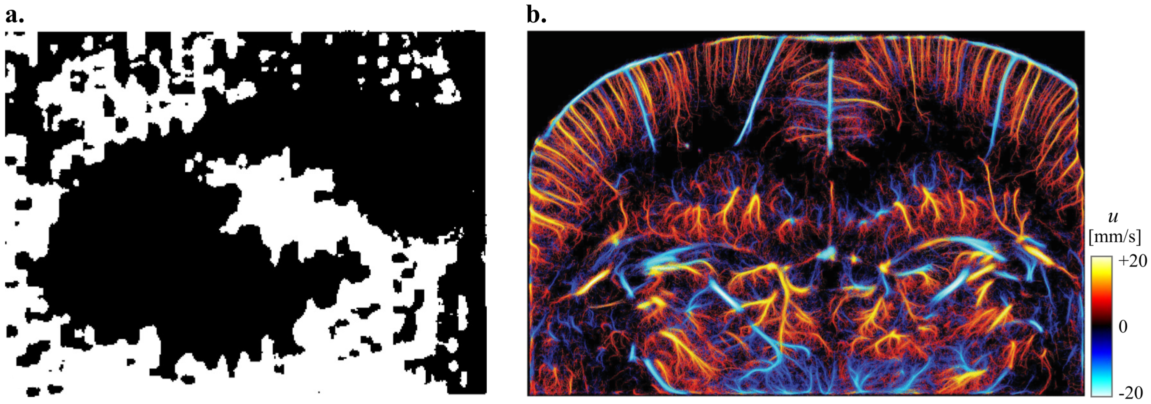

Figure 1-1: Two brain images reported with an interval of nearly 80 years. (a) Dussik's "hyperphonogram", the first reported ultrasound image of the body (1942). A sagittal slice of the human brain was imaged through a transcranial acquisition. From [2] (b) An ultrasound localization microscopy reconstruction of a coronal slice of the rat brain (2018). Positive and negative blood flow velocities u represent up- and downwards direction. From [3]

This chapter introduces the theory needed for an understanding of the problem statement. In Section 1-1 the basic principles of ultrasound imaging are discussed. Section 1-2 introduces the super resolution technique of ultrasound localization microscopy. The motivation for the research performed in this thesis is included in Section 1-3. Lastly, Section 1-4 provides the outline of this text.

1-1 Ultrasound imaging

The pulse-echo principle on which ultrasound imaging relies, is found both in nature where animals use it to retrieve their location and in other imaging applications such as sonar and radar, see Figure 1-2 for a visualization. It consists of three main parts: 1. A wave pulse is transmitted to the area that is to be examined. 2. It encounters objects or obstacles with which it interacts. This results in echoes travelling back to the observers location, where the echoes are measured. 3. The measured echo signal provides information about the objects encountered by the pulse. In particular the time of flight (TOF) is a measure of the distance to an object. Processing of this signal is necessary to recover an image of the surroundings.

In this section the basic principles of conventional ultrasound imaging are described following these three steps of the pulse-echo principle. Which kind of pulse is used in ultrasound imaging? How does it interact with the tissue? And how is an image reconstructed from the measured echoes? The section will conclude with stating the spatial and temporal resolution limits of conventional ultrasound imaging.

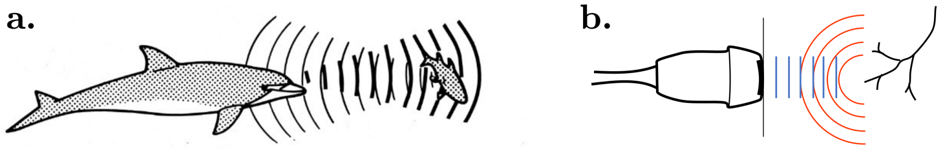

Figure 1-2: The pulse-echo principle is found both in nature and technical applications. The surroundings are perceived by transmitting a pulse and capturing echoes resulting from object interactions. (a) Dolphins apply the pulse-echo principle for echo-location of their prey. Obtained from https://navalunderseamuseum.org (b) In ultrasound imaging the pulse-echo principles is utilized to image internal tissue structures. Lines represent the wavefront.

1-1-1 Ultrasound waves

Ultrasound waves are defined as acoustic waves with frequencies above the audible range. In medical ultrasound applications frequencies of 2 MHz to 18 MHz are typically used [8]. These waves travel through tissue, causing vibration of particles around their resting position with acoustic particle velocity v_p (in m/s) in either the longitudinal or the transverse direction, resulting in compressional or shear waves respectively, see Figure 1-3(a). In the remainder of this text, we will consider only compressional waves, which is the type of wave used in Ultrasound Localization Microscopy (ULM).

The particle displacements in longitudinal direction result in a fluctuating particle density and thus a fluctuating pressure. Therefore, the compressional waves are also referred to as pressure waves. The sound pressure p (in Pa) is given by [9]

$$p = \rho c v_p = Z v_p \tag{1-1}$$

where ρ and Z are respectively the density (in kg·m^{-3}) and acoustic impedance (in Rayls or Pa·s/m) of the propagation medium and c the speed of sound (in m/s) of the longitudinal wave in the medium. The acoustic impedance is a measure for the amount of resistance a tissue presents to the acoustic wave. The speed of sound of the ultrasonic wave depends on the medium through which it travels and is given by

$$c = \sqrt{\frac{\chi}{\rho}} \approx 1540\,\mathrm{ms}^{-1} \tag{1-2}$$

where χ is the bulk modulus (in Pa) of the propagation medium. The bulk modulus of a tissue is a measure of its resistance to compression. The given approximate value corresponds to propagation in soft biological tissues [10]. The resulting wavelength λ of the ultrasound wave can be computed as [9]

$$\lambda = \frac{c}{f} \tag{1-3}$$

Where f is the frequency of the wave and c the speed of sound in the medium. The medical ultrasound frequency range of 2 MHz to 18 MHz corresponds to wavelengths of 770 to 85 μm respectively. Instead of illuminating the tissue with a continuous pressure wave, a short transmit pulse is applied, with typical duration of one cycle [11] up to a couple of cycles [12].

An ultrasound probe is capable of transmitting such a pulse by its use of piezo-electric transducer elements, which can convert electric pulses to pressure pulses and vice versa. A linear alignment of 128 elements is a typical transducer configuration [6]. In transmit, wavefronts of arbitrary shape can be constructed by adjusting the timing at which each individual element fires . Two common wave shapes used in ultrasound imaging are the plane wave and the focused beam, displayed in Figure 1-3(b) [13].

In receive, the transducer element capture the backscattered echoes by measuring the pressure variations. Here the piezo-electric elements are utilized in the reversed direction, i.e. converting a pressure difference into an electrical signal. The signal measured by the transducer elements is referred to as the radio frequency (RF) signal.

1-1-2 Tissue interaction

As acoustic waves propagate, interactions with the propagation medium occur. In general an interaction occurs when the wave encounters an object that has echogenic properties that deviate from those of the propagation medium. Two types of tissue interactions will be introduced here: reflection and Rayleigh scatter, see Figure 1-3(c). A distinction between the two can be made based on the characteristic size a of the object it encounters relative to the wavelength λ.

$$\text{Type of tissue interaction:} \begin{cases} \text{Reflection,} & \text{if } a >> \lambda \\ \text{Rayleigh scattering,} & \text{if } a << \lambda \end{cases} \tag{1-4}$$

As a result of tissue interactions the pressure amplitude of the ultrasonic pulse decreases as it propagates through tissue. This effect is called attenuation.

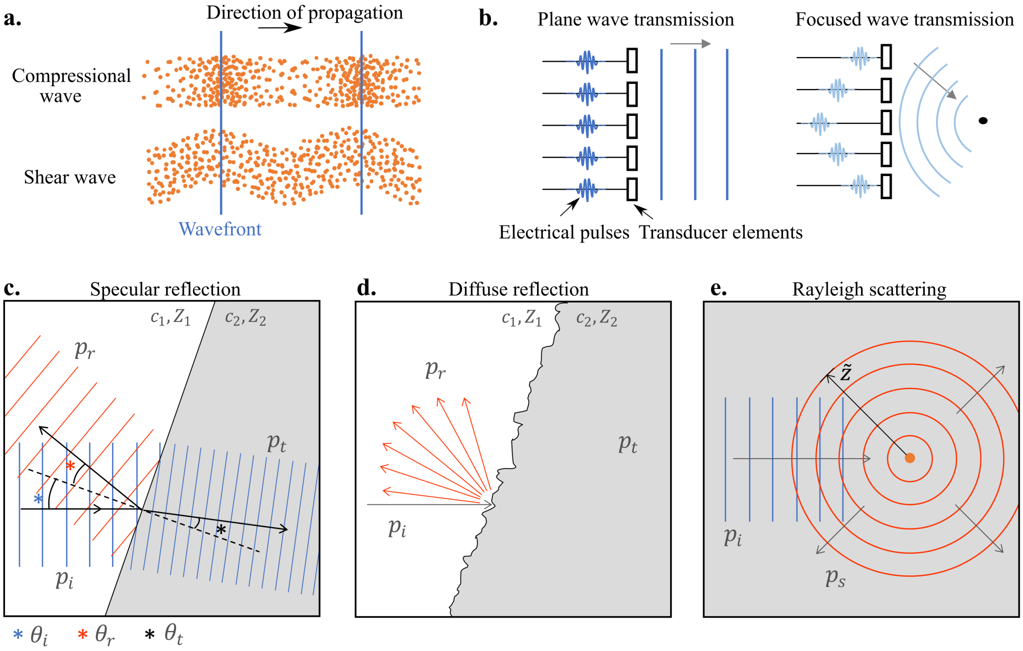
a.
Direction of propagation
Compressional wave
Shear wave
Wavefront
b.
Plane wave transmission
Focused wave transmission
Electrical pulses
Transducer elements
c.
Specular reflection
c_1, Z_1
c_2, Z_2
p_r
p_t
p_i
$* \theta_i$ $* \theta_r$ $* \theta_t$
d.
Diffuse reflection
c_1, Z_1
c_2, Z_2
p_r
p_t
p_i
e.
Rayleigh scattering
$\tilde{z}$
p_i
p_s

Figure 1-3: Illustration of the transmitted wave and its tissue interactions in ultrasound imaging. (a) Two types of acoustic waves. Particles vibrating in longitudinal or transverse direction w.r.t. the direction of propagation for respectively compressional and shear waves. (b) The ultrasound transducer consists of multiple piezo electric elements. By firing the elements in a delay pattern, transmit pulses of arbitrary shape can be constructed. (c) Specular reflection occurs when an incident wave of pressure p_i encounters a smooth interface. Part of the pressure is reflected (p_r) and the remainder is transmitted (p_t). $\theta_i = \theta_r$. (d) Diffuse reflection occurs when an incident wave encounters a rough interface. (e) Rayleigh scattering by a small particle results in a sperical echo of pressure p_s.

Reflection

Reflection generally occurs at a transition from one tissue to another, e.g. at blood vessel walls, organ boundaries or other objects with characteristic size a that is large with respect to the wavelength [6]. The mismatch between the acoustic impedances Z of the surrounding materials determines the amount of reflection and transmission. The reflection and transmission coefficients are given respectively [9]

$$\begin{aligned} r &= \frac{Z_2 \cos\theta_i - Z_1 \cos\theta_t}{Z_2 \cos\theta_i + Z_1 \cos\theta_t} = \frac{p_r}{p_i} \\ t &= \frac{2Z_2 \cos\theta_i}{Z_2 \cos\theta_i + Z_1 \cos\theta_t} = \frac{p_t}{p_i} \end{aligned} \tag{1-5}$$

where Z_1 and Z_2 are the acoustic impedances of material in which the wave was travelling and of the new material it encounters, see Figure 1-3. p_i, p_r and p_t are the incident, reflected and transmitted pressure respectively and θ_i and θ_t are the incident and transmittance angles respectively, as defined in Figure 1-3(c). The transmittance angle follows from Snell's law as $\sin(\theta_i)/\sin(\theta_t) = c_1/c_2$ and the law of reflection dictates that $\theta_i = \theta_r$ [9]. Since most biological interfaces are somewhat rough, the wave is generally not reflected into a single direction (specular reflection), but to a range of directions. This is referred to as diffuse reflection and is visualized in the second panel of Figure 1-3(d).

Rayleigh scattering

Rayleigh scattering occurs when the pressure wave encounters scatterers with a characteristic length that is small compared to the wavelength. This scatterer then re-emits a spherical wave. The echo contribution of Rayleigh scatter is typically smaller than that of reflection [9]. The ratio between the scattered pressure p_s and incident pressure p_i is given by [6]

$$\frac{p_s}{p_i} = \frac{1}{\tilde{z}}\sqrt{\frac{\sigma}{4\pi}} \tag{1-6}$$

where $\tilde{z}$ is the distance from the scatterer to the point at which p_s is to be calculated and σ is the scattering cross section of the scatterer (in m^2). The magnitude of the scattering cross section depends on several parameters such as the particle size and the contrast in density and bulk modulus between the material of the scatterer and that of the surrounding material [14]. Furthermore, it scales with the fourth power of the excitation frequency $\sigma \propto f^4$. Therefore, the scattered pressure scales with squared frequency $\frac{p_s}{p_i} \propto f^2$ [6]. In contrast to reflection, Rayleigh scattering is frequency dependent.

Speckle

A detrimental consequence of Rayleigh scattering is speckle, which can be recognized in an ultrasound image by the grainy texture. Due to its spatial randomness, speckle can be confused with noise. However, it is a deterministic interference pattern due to the Rayleigh scattering of multiple small inhomogeneities contained in the same image pixel [7]. The dominance of either constructive or destructive interference results respectively in an increased or decreased reconstructed pixel intensity [15]. As a result, the image will contain seemingly random areas of higher or lower brightness.

Since speckle is associated with a deterministic process, it does not have noise characteristics [16]. Indeed, two images taken under exactly identical circumstances (note that this is practically impossible) will result in the same speckle pattern and therefore the same image [17]. However, to model the noise-like behaviour of speckle, the Nakagami-m distribution can be used [18].

Attenuation

Attenuation describes any losses in amplitude of acoustic waves when propagating through tissue [6]. It originates from several causes such as reflection, scattering and absorption. In the latter, the wave energy is converted to thermal energy and dissipates in the tissue [13]. Generally, attenuation is modeled by an exponential decay. The pressure amplitude of the ultrasound wave over the travelled distance z is then given by

$$p(z) = p_0 e^{-a(f)z} \tag{1-7}$$

where p_0 is the initial pressure amplitude of the wave as emitted by the ultrasonic probe, $a(f)$ is the frequency dependent attenuation coefficient (in m^{-1}). For biological tissues $a(f)$ can be assumed to linearly depend on the frequency f [9]. Note that for pulse echoes, attenuation is both relevant for the path of the transmitted pulse and for the return path of the echo. Therefore, the round-trip attenuation is found from applying ((1-7)) twice.

Tissue attenuation introduces a limitation on the attainable penetration depth of the ultrasound image. As we try to image deeper into the tissue, the received echoes are more heavily attenuated resulting in increasingly lower amplitude and corresponding poorer signal to noise ratio (SNR). This effect becomes more stringent for increasing transmit frequencies, due to the increased attenuation coefficient.

1-1-3 Image formation

An example of an ultrasound data acquisition is visualized in Figure 1-4. The ultrasound transmit pulse can be recognized by the blue wavefront. In this example two scattering events occur resulting in spherical echoes. The echoes are captured by the individual transducer elements and stored as radio frequency (RF) data, visualized by the red pulses in Figure 1-4(d) and Figure 1-4(e). The different time of flights (TOF) of the echo to the different transducers causes the echo to be detected along a hyperbolic profile in the (x,t)-plane, where t is time [19].

The raw RF data has to be processed to acquire a brightness mode (B-mode) image of the internal tissue structure. Multiple processing steps are applied: IQ demodulation to reduce the frequency of the RF data [20], beamforming to create an image [19] and multiple post-processing steps such as (optional) filtering operations, envelope detection and log-compression to increase readability [16]. The process of beamforming is highlighted in the remaining, since it is the crucial step for going from data expressed on the (x,t)-plane to an image expressed in the (x,z)-plane

Beamforming

The RF signals $s_i(t)$ measured by the individual transducer elements i itself lack interpretability, they simply are a measurement of the pressure over time that reaches transducer element

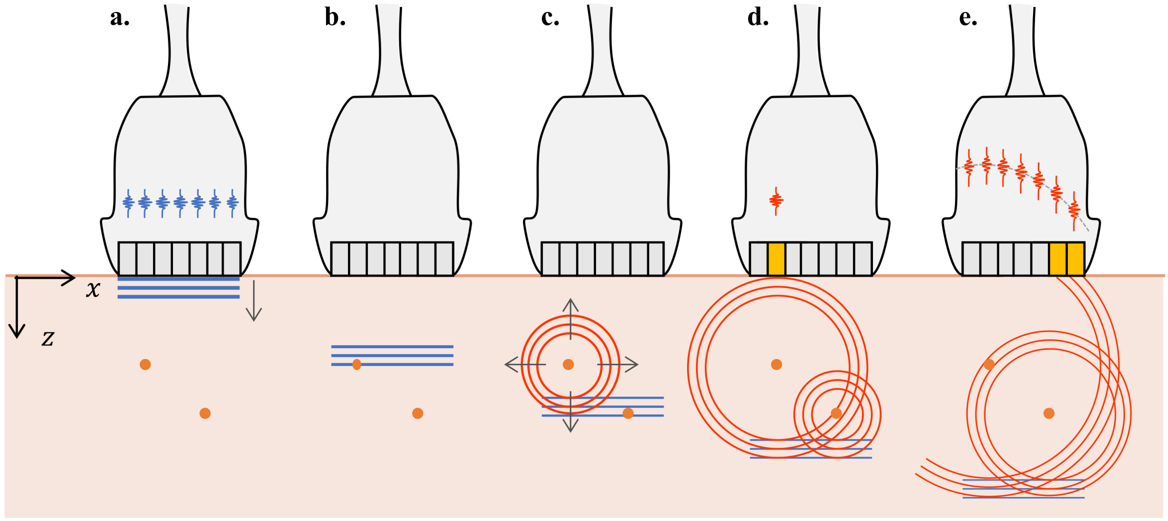

Figure 1-4: An illustration of the ultrasound data acquisition process in successive steps. (a) The ultrasonic probe emits a plane wave pulse, depicted by lines of equal phase (blue), by firing the piezo-electric transducer elements simultaneously. Two scatterers are located in the homogeneous tissue. (b) The transmit beam travels in z-direction through the tissue and encounters a scatterer (orange dot). (c) Rayleigh scattering of the first scatterer. (d) The echo (red) arrives at the probe and is detected by the yellow element. (e) Due to a difference in TOF the echo is detected by the elements in an hyperbolic shape.

i. An image can be created from the RF signal by identifying the amount of tissue interaction that took place at each pixel location.

Beamforming permits to define the image grid during processing of the data, in contrast to optical imaging where the image grid is predefined by the sensor grid. Typically B-mode images are reconstructed with a beamformed pixel size of λ or $\lambda/2$.

Delay and Sum (DAS) beamforming differentiates between the signal contributions of different scattering locations based on their time of flight. The round-trip travel time corresponding to pixel location (x, z) and transducer element i given by [19]

$$\tau_i\left(x, z\right) = \frac{d_{\mathrm{TX}}\left(x, z\right) + d_{\mathrm{RX}}\left(x, z, i\right)}{c} \tag{1-8}$$

where $d_{\mathrm{TX}}(x, z)$ is the travelled distance from the transducer to (x, z) and $d_{\mathrm{RX}}(x, z, i)$ the distance back to transducer element i, see Figure 1-5(a). These distances can be computed respectively as [21]

$$\begin{aligned} d_{\mathrm{TX}} &= z\cos(\alpha) + x\sin(\alpha) \\ d_{\mathrm{RX}} &= \sqrt{z^2 + (x - x_i)^2} \end{aligned} \tag{1-9}$$

where x_i is the x-coordinate of the transducer element i. Since d_{RX} is dependent on i, the echo from a scatterer reaches the individual elements at different time instances, resulting in a hyperbolic signature [19].

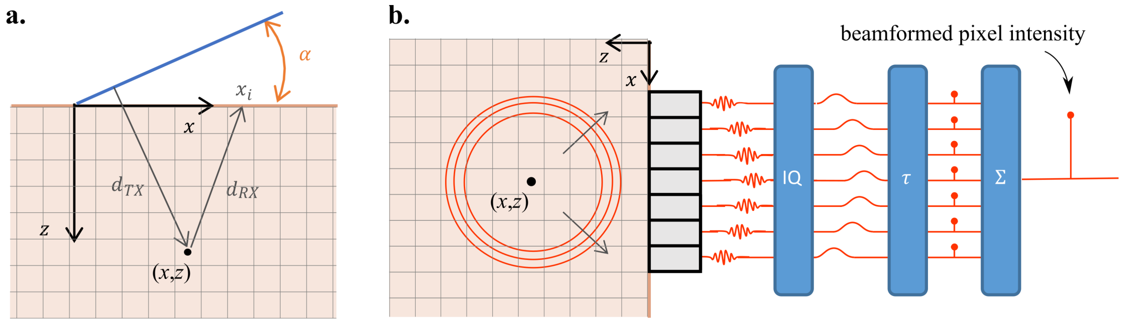

Figure 1-5: Finding the pixel intensity of the pixel centered around (x, z). The beamforming grid is overlayed in gray. (a) A plane wave (blue) at an angle α travels a distance d_{TX} towards the pixel center. The resulting echo resulting from scatterers within the pixel travels a distance d_{RX} back to transducer element i. (b) An illustration of DAS beamforming to retrieve the pixel intensity from the recorded RF signal. Due to a difference in d_{RX} the echo reaches the transducer elements (gray) in a hyperbolic shape. IQ demodulation is applied to find the complex envelope of the transducer signal. At the appropriate delay, the values of the IQ demodulated signals are read out and added to find the pixel intensity.

To find the pixel value of location (x, z) the echo signals $s_i(t)$ are first delayed by $\tau_i(x, z)$ to account for the hyperbolic shape and then summed. This has to be repeated for each pixel location, resulting in the beamformed image

$$s_{\mathrm{bf}}(x, z) = \sum_{i=1}^{N_{\mathrm{e}}} s_i(\tau_i(x, z)) \tag{1-10}$$

where N_e is the number of transducer elements. Since $s_i(t)$ is sampled at discrete points in time and $\tau_i(x, z)$ is a continuous value, interpolation is necessary to obtain $s_i(\tau_i(x, z))$ [19].

Due to the directivity of the transducer elements, the amplitude of the echo signal $s_i(t)$ achieves its maximum at the top of the hyperbolic signature, i.e. at the transducer elements of similar x coordinate as the pixel [19]. Moving further away along the hyperbola, the signal amplitude decreases resulting in a decreased SNR. Therefore, one can choose to only select the top of the hyperbola in beamforming by using the f-number $f_{\#}$. The f-number describes the ratio between the size of the receive aperture and the imaging depth as [19]

$$f_{\#} = \frac{z}{\text{Aperture size}} \tag{1-11}$$

were z corresponds again to the z-coordinate of the pixel to be reconstructed. Instead of summing over the total number of elements N_e in (1-10), a selection of the elements centered around x is made. Only the RF signal measured by this new set of elements is used to compute the pixel intensity as in (1-10).

The process of DAS beamforming is illustrated in Figure 1-5(b, where an additional step is recognized: in-phase quadrature (IQ) demodulation. The high frequency RF signal is IQ demodulated to find its low frequency complex envelope [19]. One can interpret the process of IQ demodulation as the separation of the signal of interest from the carrier signal, here the high frequency pulse [16].

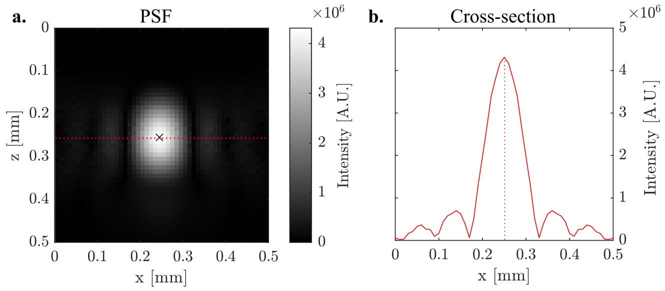

Figure 1-6: The point spread function (PSF) shows the blurring caused by diffraction. (a) Simulated image of the PSF, created by simulating a point scatterer (black cross) located at (0.25,0.25) mm expressed in the local coordinates of the extracted patch. Transmit frequency $f = 17.86$ MHz, wavelength $\lambda = 86.2$ μm, $\#f = 1$, beamformed pixel size $dx = 10$ μm. (b) The cross-section of the PSF along $z = 0.25$mm. Dotted line gives the location of its peak.

1-1-4 Spatial resolution

Due to its use of waves to image the tissue, the spatial resolution of ultrasound images is limited by diffraction. The blurring effect of diffraction becomes clear when inspecting the point spread function (PSF) of an imaging system, which is given by the systems response to a point source. In Figure 1-6 the PSF of an ultrasound acquisition at 17.86 MHz was simulated using the Verasonics Research Ultrasound Simulator (VRUS) (Verasonics, Kirkland, WA, USA). Instead of a sharp point, the image of the point source has a blob-like spread with a full width at half maximum (FWHM) along x of 78 μm.

Generally, the formation of an image I of object O is described by the convolution [22, 23]

$$I = \text{PSF} * O \tag{1-12}$$

where $*$ is the convolution operator. This convolution of the object with the PSF of the imaging system creates a blurring of the image. The convolution operation can be interpreted by using a thick marker with the shape of the PSF to draw a detailed image. The size of the PSF is proportional to the used wavelength. For the PSFs considered in the remainder of this text, its main lobe will be assumed to have a Gaussian shape.

The blurring caused by the PSF creates a fundamental limit on the obtainable spatial resolution, i.e. the diffraction limit. Spatial resolution is defined as the minimum distance between two objects that still allows the objects to be distinguished. A limit to the spatial resolution of a general imaging system is given by the Rayleigh criterion [24]

$$R = 1.22\lambda\frac{f_\text{L}}{D} \tag{1-13}$$

here R is the resolution limit (in m), f_L the focal length (in m) and D the aperture diameter (in m). For application to ultrasound modalities we can replace the fraction by $f_\#$ resulting in

$$R = 1.22\lambda f_\# \tag{1-14}$$

Point sources that are closer together than R can not be individually resolved, as is visualized in Figure 1-7, where R equals 105 μm. The two point scatterers at 100 μm interdistance appear as a single blur on the US frame.

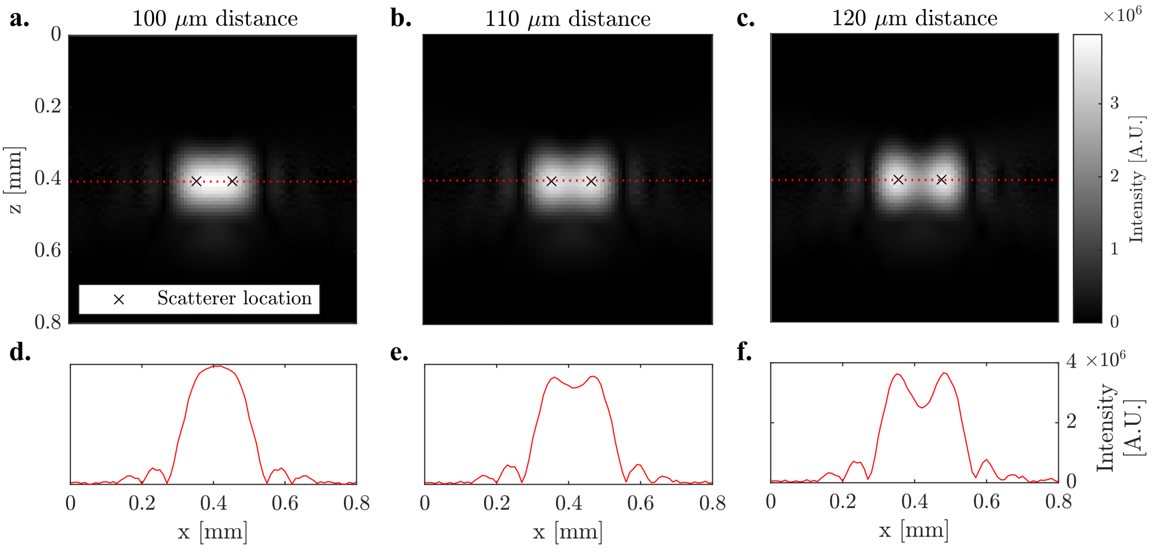

Figure 1-7: Objects closer than the Rayleigh resolution limit can not be individually distinguished. Here $R = 105$ μm (a-c) Simulated B-mode images of two point scatterers (black cross) with separation distances of respectively: 100 μm, 110 μm and 120 μm. Transmit frequency $f = 17.86$ MHz, wavelength $\lambda = 86.2$ μm, f-number $= 1$, beamformed pixel size $dx = 10$ μm. (d-f) Pixel intensity values along the line $z = 0.4$mm.

Due to this spatial resolution limit and typical US wavelengths of $\sim$ 100 μm, many small anatomical structures of the human body remain imperceptible. Increasing the transmit frequency results in an improved resolution due to a shorter wavelength. However, the high frequency wave experiences an increased attenuation, as modeled by (1-7), resulting in a lower attainable penetration depth of the imaging modality. Therefore, in conventional diffraction-limited ultrasound imaging a trade-off between spatial resolution and penetration depth exists.

1-1-5 Temporal resolution

The frame rate at which consecutive B-mode images can be acquired is limited by the round-trip travel time of the pulse-echo. As a result the temporal resolution decreases for imaging deeper tissues.

In the previous sections, the examples show a plane wave illumination, where the entire field of view (FOV) is illuminated with a single transmit pulse. Using plane wave imaging, a full image can be created from a single transmission. This makes plane wave imaging significantly faster than the traditional focused beam method that creates only a single line of the image for every transmission. To improve the resolution of the low quality plane wave images, Montaldo *et al.* [21] proposed to coherently compound several images acquired with plane wave illuminations at varying angles. This method was shown able to regain spatial resolution while remaining superior in temporal resolution as compared to focused beam imaging. The coherent plane-wave compounding method has been an important breakthrough. Its improved temporal resolution enabled the development of multiple ultrasound modalities such as functional ultrasound imaging (fUS) [25] and ULM [12, 26].

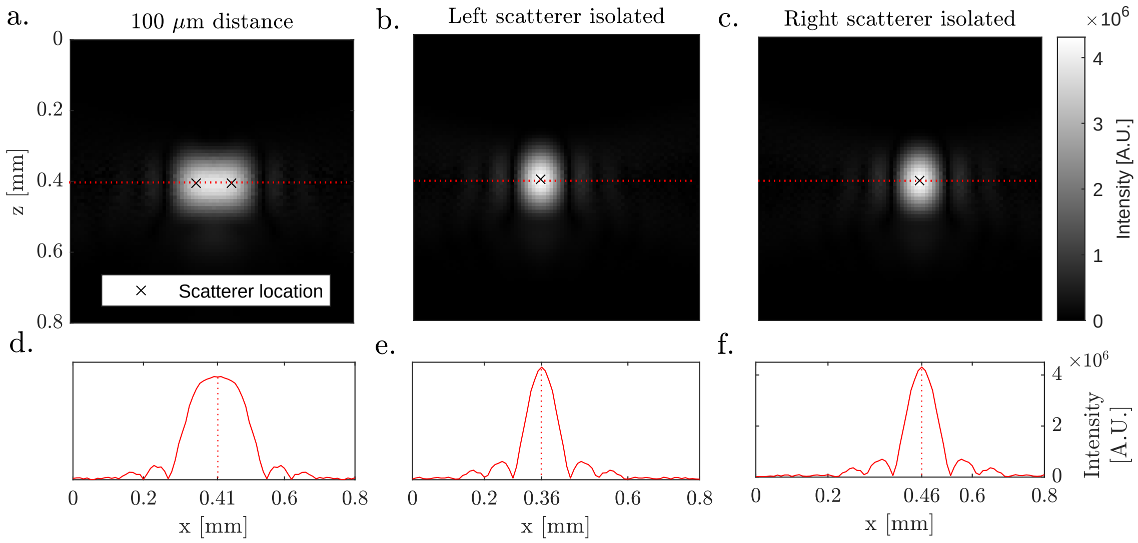

Figure 1-8: Individual ultrasound imaging of point scatterers. (a)-(c) Ultrasound simulations of three scenarios respectively: two scatterers at 0.36 mm and 0.46 mm, a single scatterer at 0.36 mm, a single scatterer at 0.46 mm. Transmit frequency f =17.86MHz, wavelength $\lambda = 86.2$ μm,f-number$= 1$. Simulation created on a 10 μm grid. (d)-(f) The pixel intensity values along the line $z = 0.4$mm. The dotted line gives the x value at which the maximum is achieved.

1-2 Ultrasound localization microscopy

1-2-1 Introduction to the technique

ULM is a super resolution ultrasound technique to image the vasculature. To break the classical diffraction limit, it was inspired by its optical counterpart single molecule localization microscopy (SMLM) [27]. Both methods rely roughly on the same steps. Sources of sub-wavelength size are isolated such that their response is unaffected by interference. These sources, considered as point sources, are individually imaged and their location is estimated with a sub-wavelength precision. The localizations of a large number of frames is accumulated to create the final super resolution image.

The effect of this individual imaging of point sources is visualized in Figure 1-8, where the simulation with the VRUS of two point scatterers at 100 μm is repeated. The two point scatterers were found unresolvable when imaged simultaneously. If able to capture the response of one point source at a time, the two point sources can be distinguished. Both ULM and SMLM rely on the isolation of point sources to improve resolution.

The invention of SMLM in 2006 formed a breakthrough enabling the field of super-resolution microscopy to enter the nanometer realm [27, 28]. Eric Betzig and William E. Moerner who developed the principles of SMLM were awarded the Noble price for their work [29, 30]. In 2010 Couture *et al.* [31] proposed to apply the concept of SMLM in ultrasound imaging, it marked the start of the ULM research field. In Table 1-1 a comparison between several basic characteristics of the two techniques is made. In the remainder we will solely focus on ULM.

Table 1-1: Comparison between ULM and SMLM

	ULM	SMLM
Imaging wave	Ultrasonic wave	Optical wave
λ	~100 μm	~ 500 nm
Penetration depth	~10 mm	~100 nm
Imaged sources	Gas-encapsulated microbubbles (MB)	Fluorescent molecules
Motion of sources	Moving with blood flow	Static
Application	*in-vivo* imaging of the vasculature and its blood velocity	*in-vitro* imaging of cells or proteins

Microbubbles (MB): the point sources in ultrasound localization microscopy

In ULM, a low concentration of gas-encapsulated microbubble (MB) of size 3-8 μm is injected into the vasculature. Due to their small size compared to the ultrasonic wave length, microbubbles can be considered as point sources in ultrasound imaging and their response resembles the system's PSF [32, 33]. Meanwhile their size is too large to permit the perfusion into the tissue, causing the MBs to stay intravascular untill they collapse.

The ULM process is based on the detection of the MBs in the input B-mode frames by filtering out static tissue signal, the localization of the MBs with sub-wavelength precision, and the tracking of MBs over consecutive frames, see Figure 1-9. The acquired MB tracks are accumulated on a fine grid to construct a ULM reconstruction. ULM images displaying different properties can be constructed: a density map reports the number of MBs that flowed through each pixel, a velocity map represents the average blood flow measured in that pixel, and a flow orientation map reconstructs the flow direction from the MB tracks.

A crucial condition for the working of ULM is that the MBs need to be isolated. Any interference that degrades the localization precision needs to be avoided. A microbubble is considered to be isolated if the localization of its center is not influenced by any other sources originating either from other microbubbles or from tissue.

To ensure that the MBs are isolated from other MBs and their responses do not spatially overlap, the injected concentration is diluted to achieve spatially sparse MBs. To prevent the signal resulting from tissue to influence the MB localization, the MB image contribution is separated from that of tissue by a filtering operation. By exploiting several MB properties this separation is possible.

First, MBs are known to be resonant oscillators in an ultrasonic field. The compressed gas acts as a spring and the surrounding aqueous solution as a mass, together forming a mass-spring system [34]. Due to this resonance, the scattering cross section of the MB drastically increases around its resonant frequency, as was shown by [14]. The increased scattering cross section of MBs makes for a stronger echo than echoes resulting from Rayleigh scatter in the surrounding tissue. Secondly, the resonance of the MB also gives rise to nonlinear echoes, containing subharmonic and superharmonic frequencies [35]. Since surrounding tissue generally has a linear ultrasonic response, the MBs can be distinguished by their non-linear

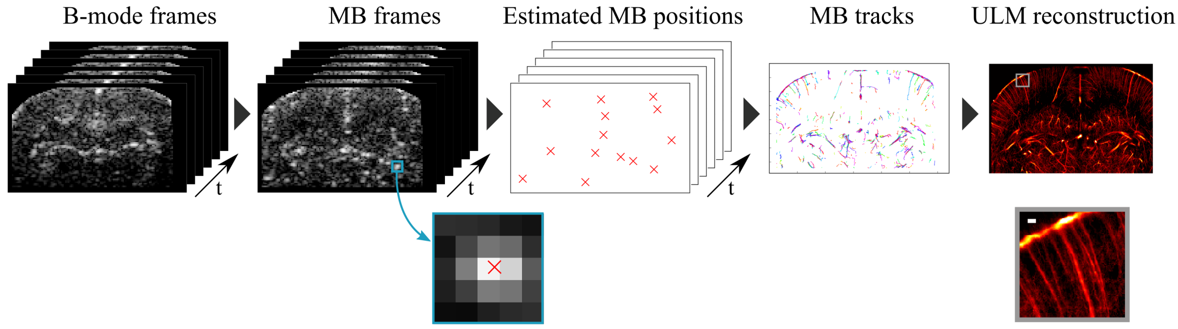

Figure 1-9: The process of creating a ULM reconstruction from input B-mode frames visualized. During a ULM acquisition, microbubbles (MB) are injected in the vasculature and a large number of B-mode frames is acquired over time. Static tissue signal is filtered out, resulting in MB frames that highlight the nonlinear image contribution of the microbubbles. MB events are detected and localized with sub-wavelength precision. The temporal dimension is collapsed by linking estimated MB positions over consecutive frames. The MB tracks are accumulated to find the ULM reconstruction. In the ULM density map displayed here vessels of diameter far below the wavelength can be distinguished. Scalebar: $\lambda = 102\ \mu$m. Data from [4].

behaviour. Lastly, in contrast to tissue that is mostly static, MBs move along with the blood flow. Due to this difference in spatiotemporal coherence the MB signal can be distinguished from that of tissue. These MB properties are exploited by the methods described in that aim to retrieve MB signal from the input B-mode frames.

Chapter 2 elaborates on each of the individual steps in the ULM data processing pipeline: detection of MB signal, localization of MB position, tracking of the MBs, rendering the MB tracks to ULM reconstructions and motion correction.

1-2-2 Spatial resolution

By the localizing the MBs with a sub-wavelength precision, ULM is able to image microvessels that would not be resolvable with diffraction limited ultrasound imaging. The obtained experimental spatial resolution in ULM is often reported as the smallest vessel that can be resolved or the smallest separation distance between vesles. The full width at half maximum (FWHM) should not be used to represent the diameter of the reported vessels, due to the absence of a PSF in ULM reconstructions [3]. In contrast, the full width should be reported since each acquired MB track was assumed to lie within a vessel.

Since the diffraction limit is proportional to the wavelength λ, the spatial resolution is often expressed in wavelengths, allowing an easier comparison between experiments. Resolutions up to $\lambda/10$ were reported [12]. A theoretical bound on the obtainable spatial resolution in ULM is given by the localization precision with which the center of the MB is estimated [12].

Even though there is a consensus on the fact that ULM is able to achieve sub-wavelength resolution, one should adapt a critical attitude towards reported resolution values in ULM [34, 3]. ULM is not always able to reliably reconstruct the vasculature. The accumulation of MB tracks travelling through a particular vessel does not directly represent the actual underlying structure. For instance, the diameter of a vessel can be heavily underestimated when it is occupied by relatively little trajectories [34]. The super resolution grid size on which the reconstruction is displayed (generally $\lambda/10$) is a relevant factor here.

1-2-3 Temporal resolution

To construct a super resolved ULM image, hundreds of thousands of conventional B-mode images are needed, which heavily increases the acquisition time (typically ~ 100 s). In fact, one could state that in order to obtain a high spatial resolution image, ULM sacrifices temporal resolution.

There are multiple factors that limit the temporal resolution of ULM. First of all, to enable a sub-wavelength localization, MBs need to be isolated. To obtain spatially isolated MBs, a low concentration is injected and only a limited number of MBs can be detected in each B-mode frame. By developing localization algorithms that can handle higher MB concentration without sacrificing localization precision, the acquisition time can be shortened [33, 36, 37]. Being able to handle a higher concentration, a larger number of MBs per frame can be localized. This decreases the number of necessary frames and equivalently the acquisition time.

A second factor limiting the temporal resolution of ULM is the fact that a minimum number of MBs needs to be tracked in each individual vessel to be able to adequately reconstruct that vessel and prevent an underestimation of its width. Hingot *et al.* [38] showed ULM acquisition time to be dictated by slow flow in the microvasculature. An acquisition time of less than 10 s was found sufficient for the reconstruction of larger vessels (~ 100 μm), while for a full reconstruction of all small capillaries tens of minutes were required.

1-3 Thesis motivation

Due to the large improvement in spatial resolution of ultrasound localization microscopy the microvasculature and its flow can be succesfully retrieved [12, 26, 34]. However, the improved spatial resolution comes at the cost of temporal resolution. Since a large number of MB tracks is accumulated during the long ULM acquisition time, flow fluctuations are averaged out. The final ULM velocity map represents the average velocity during the acquisition, which is not representative of the underlying blood flow. Especially in arteries the blood flow is never stationary, due to the pulsatility induced by the heartbeat [5]. Retrieving flow fluctuations is especially interesting when imaging the brain. Due to neurovascular coupling, the cerebral blood volume in a region of the brain is a measure of its activity [39, 25].

In this thesis, we aim to retrieve pulsatility in the microvasculature by leveraging the high temporal sampling of MB tracks. Two independent methods for pulsatility retrieval are introduced. The first method is based on filtering the velocity measurements obtained from single MB tracks to reduce the noise caused by MB localization error.

Instead of following a single MB track, the second method relies on a static observer. During the acquisition, velocity measurements of passing MBs are accumulated into a velocity distribution. We show that pulsatility leads to bimodality in this distribution. The minimum and maximum flow during the pulsatile cycle are extracted from the found distribution.

We validate both methods in simulated data that incorporates pulsatility. To our best knowledge all previously reported ULM simulators assumed the blood flow to be stationary [36, 37, 40]. We design a ULM simulator that: simulates pulsatile flow, propagates MB through that flow, simulates B-mode images and performs ULM processing.

1-4 Outline

This chapter has covered the basics of ultrasound imaging and ultrasound localization microscopy (ULM) and it introduced the thesis motivation. In Chapter 2 the ULM processing pipeline is described. It covers each of the necessary processing steps for creating a ULM reconstruction based on input B-mode images. Chapter 3 provides the main contribution of this study in a manuscript format. In the manuscript two methods of retrieving pulsatility in ULM data are introduced and a proof of concept is given by application of the methods on simulated data. The manuscript is formatted in the style of *IEEE Open Journal on Ultrasonics, Ferroelectrics, and Frequency Control.* Chapter 4 provides a conclusion of the thesis. It starts with a summary of the findings described in the manuscript. A discussion is added to address additional points of discussion not included in the manuscript. Chapter 4 is concluded by providing recommendations for future research.

Chapter 2

Ultrasound localization microscopy image processing

To create a super resolved ULM reconstruction out of hundreds of thousands of ultrasound B-mode images, multiple processing steps are needed. These can be divided into five categories, as visualized in Figure 2-1.

From the input B-mode images $I(x, z, n)$ with time index n, first the contribution of the microbubble (MB) signal needs to be separated from that of the surrounding tissue. In the resulting MB images $I_{MB}(x, z, n)$ regions of interest (ROI) are detected that are assumed to contain a MB event. These two steps are explained in Section 2-1 on detection.

From the extracted ROIs, the sub-pixel location of the MB is estimated. To find the estimate $(\hat{x}, \hat{z})$ of the MB location, several methods have been developed. The most frequently used methods are explained in Section 2-2.

Microbubbles are not stationary but flow along with the blood flow. The MB tracks T can be found by linking MB localizations of consecutive frames. Section 2-3 describes several tracking methods applied in ULM. From each track, raw velocity estimations u_n can be computed.

The rendering of the trajectories to either a density or a velocity reconstruction is described in Section 2-4. Even though multiple steps are involved, the process of rendering is not well described in literature. The raw velocity measurements are first smoothed to find u_n^{f}. Afterwards the tracks are spatially interpolated and accumulated to find the super resolved (SR) reconstruction $I_{SR}(x_{SR}, z_{SR})$ on the upsampled grid (x_{SR}, z_{SR}).

Finally, motion correction is described in Section 2-5. For *in-vivo* acquisitions this step is very useful to prevent motion artefacts in the reconstructions. In the simulation study described in the remainder of this report no tissue motion was simulated. Therefore this section will function as a short introduction to the topic.

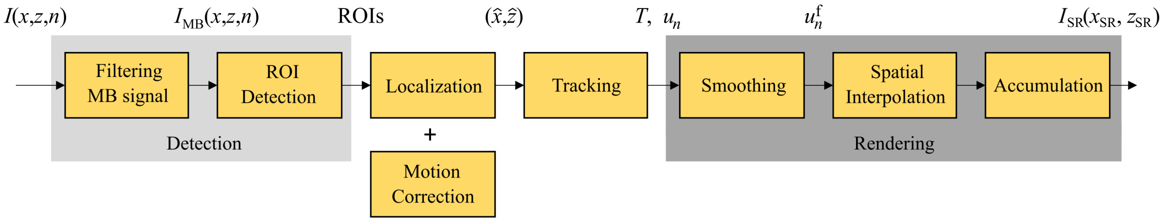

Figure 2-1: A detailed depiction of the ultrasound localization microscopy processing pipeline. Input are the B-mode frames $I(x, z, n)$. The outputted super resolved reconstruction can be either a density map, a velocity map or a flow orientation map. The main four steps are: detection, localization, tracking and rendering. The motion correction processing step is optional.

2-1 Detection

The process of detecting MB events in a B-mode image consists of two steps described in Section 2-1-1 and Section 2-1-2.

2-1-1 Retrieval of microbubble signal

In the first substep of Figure 2-1, the MB image contribution is separated from that of the tissue. The main MB properties which can be exploited for the separation are their nonlinear behaviour, their strong echogenic properties resulting in bright image contribution and the fact that the MBs are moving.

Two approaches are described here that intervene at different steps in the pipeline. First, the separation of the MB signal from the tissue signal can be obtained by filtering the acquired B-mode images $I(x, z, n)$ with a singular value decomposition (SVD) filter. Alternatively, the imaging sequence of ultrasound transmissions can be adjusted to eliminate the tissue signal in the beamformed image.

Singular value decomposition (SVD) filter

The images $I(x, z, n)$ can be filtered on a spatiotemporal basis by application of the SVD filter. The input $I(x, z, n)$ is decomposed on a spatiotemporal basis into multiple parts each corresponding to one of its singular values. Demené *et al.* [41] found the image contributions from static tissue signal, moving scatterers and noise to correspond to different singular values. Therefore, a filter is constructed by only attaining the image contributions of the singular values corresponding to the MB signal.

Proposed by Demené *et al.* [41] the approach was initially focused on the separation of blood signal from tissue signal for application in Power Doppler imaging. They found that the image contribution of the moving scatterers in the blood could be distinguished based on its spatiotemporal characteristics. The temporal coherence of the signal resulting from the moving scatterers is significantly smaller than that resulting from the static tissue. Additionally, it was shown that the spatial coherence of the image contribution of blood scatterers is lower than that of tissue [41]. While the original application focused on the separation of blood

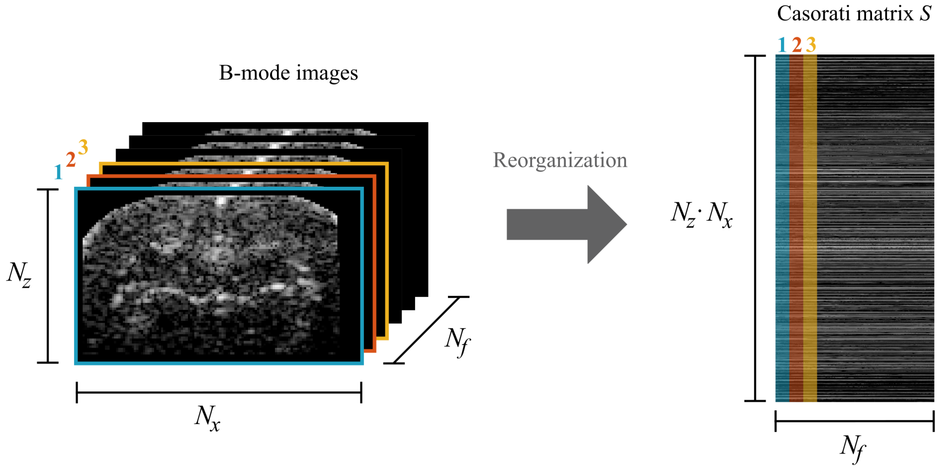

Figure 2-2: The input B-mode images are reorganized into the spatiotemporal Casorati matrix S. Each B-mode frame corresponds to one column in S. N_z, N_z and N_f are the number of pixels in z, the number of pixel in x and the number of B-mode frames of the inputted set. Data from [4].

signal, later papers showed this method to be applicable to the distinction of MB signal as well [12, 42]. To apply the singular value decomposition (SVD) filter, the images have to be reshaped to a Casorati matrix, see Figure 2-2. For each time frame n the corresponding image is reshaped into a column vector. These columns are then concatenated into the 2D space-time Casorati matrix S with dimensions $(N_x N_z, N_f)$, where N_x and N_z are the number of pixels in x and z dimension respectively and N_f is the number of time samples [41]. The full B-mode acquisition is typically split up into chunks of data that are SVD filtered separately [1]. A singular value decomposition of S is performed as [41]

$$S = U \Delta V^H \tag{2-1}$$

where U and V are orthonormal matrices constructed of the spatial and temporal singular vectors of S respectively. Their sizes are respectively $(N_{xz}, N_x N_z)$ and (N_f, N_f). The subscript ^{H} indicates the conjugate transpose and Δ is a non-square diagonal matrix of size (N_{xz}, N_f) containing the ordered singular values σ_i on its diagonal. The first singular values correspond to image contributions of the highest spatiotemporal coherence. An alternative writing of the SVD of (2-1) is given by [41]

$$S = \sum_i \sigma_i A_i = \sum_i \sigma_i U_i \otimes V_i \tag{2-2}$$

where $\otimes$ is the outerproduct and the i^{th} columns of the matrices U and V are respectively given by U_i and V_i, with σ_i being the corresponding singular value. Each of the columns U_i corresponds to an individual spatial image modulated by the temporal signal stored in V_i. If the summation is not performed over all available i but only over the defined interval, a filtered image $I_{MB}(x, z)$ can be reconstructed. Demené et al. showed that the tissue signal is mostly described by the highest singular values. The lower singular values correspond to MB and noise signals. Therefore, removing the signal contribution corresponding to the highest singular values (up to some threshold) rejects the tissue signal. Noise can be filtered out by excluding the contribution of the lowest singular values. The filtered Casorati matrix is given by

$$\tilde{S} = U\tilde{\Delta}V^H \tag{2-3}$$

where $\tilde{\Delta}$ is the truncated matrix containing the singular values that are kept. The singular values corresponding to the eliminated images are set to zero. From the filtered Casorati matrix $\tilde{S}$, the filtered MB images $I_{MB}(x, z, n)$ can be retrieved.

The microbubble and tissue signal proved to be better separable in a spatiotemporal sense than solely on a temporal basis. This was found especially for imaging the microvasculature, which contains slow blood velocities [41]. The SVD filter was shown to be able to dinstinguish MB signal *in vivo* [12].

An extension to this method was proposed by Huang [33] where MB detections were separated into several MB sub-populations by a filtering operation in the spatiotemporal Fourier domain. Each of the resulting images corresponding to a sub-population was then further processed individually by the Ultrasound Localization Microscopy (ULM) pipeline. The method showed to be able to separate spatially overlapping MB signals and therefore to handle higher concentrations of MB reducing the necessary acquisition time. Even though the MB signal could be separated into sub-populations, the interference between two spatially overlapping MB signals can not be fully eliminated by this operation.

Imaging sequences to separate MB signal

The separation between tissue and MB signal can also be made based on the nonlinear MB response. The pulse inversion (PI) [43] and amplitude modulation [6] techniques, are designed to eliminate the linear parts of the echo signal. These techniques intervene at a much earlier stage in the process than the SVD filter. Here the imaging sequence used to acquire the echo signal is altered. The image that is then beamformed from the resulting echo signal corresponds to the nonlinear MB signal. No additional filtering is necessary to obtain the MB image.

To eliminate the linear tissue response, the PI method uses a transmit sequence that consists of two pulses, see Figure 2-3. The second pulse in this sequence, emitted after some suitable delay, is an inverted copy of the earlier emitted pulse [43]. The received echos from both pulses are then added to attain only the nonlinear MB response. The linear parts of the two echos cancel each other out, since by definition the output of a linear system is exactly inverted when an inverted input is applied. Amplitude modulation works in a similar manner. Here the second pulse is not inverted, but its amplitude is altered, an example is given in Figure 2-3.

Note that for both methods, at least two illuminations are needed to acquire the data for one B-mode image. Therefore, one of the main disadvantages of these methods is the reduced frame rate at which the B-mode images are acquired. ULM strongly benefits from a high frame rate. Therefore, the SVD method is more commonly used.

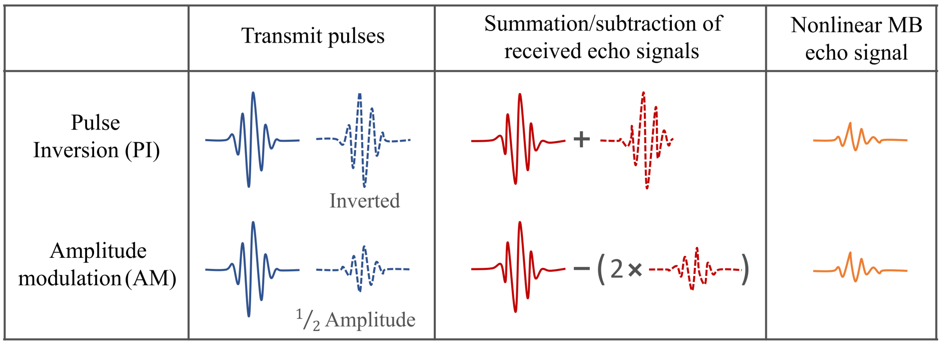

Figure 2-3: The PI and AM techniques are capable of isolating the nonlinear MB response by altering the imaging sequence. A sequence of transmit pulses are utilized (blue). From the recombination of the measured echo signals (red) the nonlinear part of the echo signal can be retrieved (orange). The resulting nonlinear part is beamformed to $I_{MB}(x, z, n)$

2-1-2 Extraction of regions of interest

After the extraction of the MB signal, the individual MB need to be detected. Before sub-pixel localization, the regions of interest (ROI) that contain a MB need to be identified. These ROIs are identified based on their likeness to the expected MB signal, which can be assessed by applying a cross correlation between the image $I_{MB}(x, z, n)$ and a 2D Gaussian shaped PSF [32]. The ROIs can be found from the regions of highest cross correlation score.

An alternative method, is to find the pixels of highest intensity in the MB image and center a ROI around each detected maximum. ROIs that contain more local maxima than a set threshold, are assumed to not contain an isolated MB and are discarded [1].

Additional methods may be applied to eliminate false ROI detections or spatially overlapping ROIs. A threshold can be set on either the intensity or the value found from cross correlation with a Gaussian PSF to reject low-confidence ROIs [33]. Furthermore, to ensure only isolated microbubbles to be included in the remainder of the pipeline, ROIs that are spatially overlapping can be eliminated to prevent potential interference effects [32].

2-2 Localization

The localization of the microbubble location with sub-wavelength precision is the key factor enabling super resolution in ultrasound localization microscopy. In the following subsections the most frequently used localization algorithms are described. See Figure 2-4 for a visual representation of these algorithms.

2-2-1 Peak detection

The most simple localization algorithm consists of selecting the pixel location of highest intensity. However, this would not result in a sub-pixel localization. In this case the spatial resolution of the ULM reconstruction is limited by the beamformed pixel size. Alternatively, interpolation can first be applied before peak detection [32]. The estimated location is then

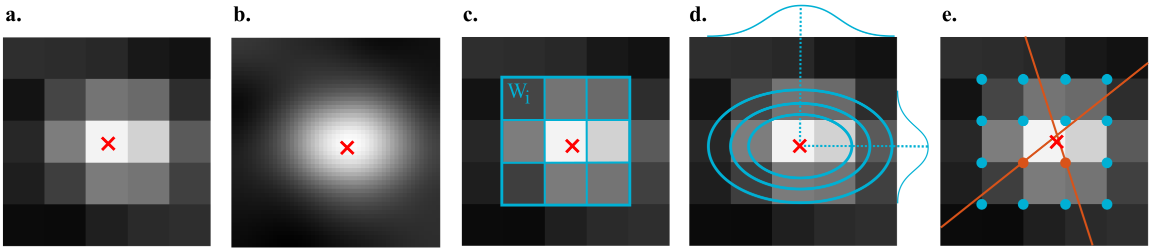

Figure 2-4: An illustration of localization algorithms commonly used in ULM. (a) Peak detection method without interpolation. (b) Peak detection method with Lanczos interpolation. (c) Weighted average method. (d) 2D Gaussian fitting. (e) Radial symmetry method.

given as the highest intensity pixel of the upsampled grid. Multiple interpolation methods can be applied, such as the spline, Lanczos or cubic interpolation [1].

2-2-2 Weighted average

A slightly more advanced method consist of estimating the MB centroid by an intensity weighted average [26, 44]. The MB localization estimate ($\hat{x}$,$\hat{z}$) in a ROI can then be found by

$$(\hat{x}, \hat{z}) = \frac{\sum_{i \in \mathrm{ROI}} w_i(x_i, z_i)}{\sum_{i \in \mathrm{ROI}} w_i}, \qquad \hat{z} = \frac{\sum_{i \in \mathrm{ROI}} w_i z_i}{\sum_{i \in \mathrm{ROI}} w_i} \tag{2-4}$$

where the index i runs over all pixel in the corresponding ROI. Generally, the weights w_i correspond to the pixel intensities.

2-2-3 Gaussian fitting

The Gaussian fitting method estimates the center in a parametric fashion. The 2D Gaussian shape is fitted in a least squares sense by fitting its parameters including the center location in x and z, the standard deviations σ_x and σ_z, the intensity, the tilt angle and the offset. An estimation of the MB position is then retrieved from the summit of the 2D Gaussian [12].

2-2-4 Radial symmetry

Alternatively one could use a localization method that exploits radial symmetry [1, 45]. For a perfect radial symmetric intensity, all lines perpendicular to the gradient intersect at the object's center. The radial method proposed by Parthasarathy exploits this property [45]. At each junction of four pixels, here referred to as grid points (dots in Figure 2-4(e)), the local gradient was computed based on the intensity of the four surrounding pixels and a line was defined in direction of that gradient. The MB position estimate $(\hat{x}, \hat{z})$ was found by the location that minimizes the weighted sum of all distances to the drawn gradient lines. Weights scaled with the intensity gradient found at the grid points and inversely scaled with the distance of the grid points to the MB centroid (found by weighted average method).

Comparison of localization algorithms

In a recent study by Heiles *et al.* [1], the performance of the above mentioned algorithms was assessed on both simulated and *in vivo* data. The Gaussian fitting and radial symmetry method were found to perform the best on separating two converging channels, with attainable separation distances of 0.46 λ and 0.36 λ respectively. Based on the average root mean square localization error (RMSE) Gaussian fitting slightly outperformed the radial symmetry method for low SNR cases. At SNR = 10 the methods achieved an RMSE of 0.27 λ and 0.31 λ respectively. The required computation time was found to be the biggest performance difference between the two algorithms: for the Gaussian fitting method a computation time was required which was 40 times larger than that of the radial symmetry method.

Due to its fast computation and low RMSE in high SNR scenarios, the weighted average method wass found to be a good choice for SNR $>$ 30 dB. However, for scenarios in which the SNR drops below 30 dB, either the Gaussian fitting and radial symmetry method should be applied [1].

2-3 Tracking

MB tracks can be found by linking the estimated MB positions over consecutive frames as illustrated in Figure 2-5(a). Tracking MB in ULM has several benefits. Firstly, measurements of the local blood flow can be obtained from MB trajectories. A raw velocity estimate is simply given by the distance a MB has travelled from one frame to another divided by the time between these frames. Due to tracking, the MBs can be considered as moving blood flow sensors.

Secondly, by rejecting tracks of lengths below some threshold, the effect of false MB detections is limited. It is assumed here that false MB detections are typically found in these short tracks. Trajectories in which a MB is followed for many frames are deemed more reliable.

Finally, the image quality is of the ULM reconstructions is improved by spatial interpolation of the MB locations of the track. By estimating these intermediate locations, the gaps between the tracked MB localizations can be filled. These gaps can become particularly large when MB velocity is high compared to the sampling rate. Section 2-4-2 discusses spatial interpolation of trajectories in more detail.

The MB tracking methods described here are divided into two categories each described in a separate subsection: local search methods and combinatorial methods. Besides the frequently used algorithms comprised by these sections, MB tracking can be performed by alternative methods such as Markov Chain Monte Carlo (MCMC) [46, 47], multiple hypothesis tracking (MHT) [48] or Kalman filtering [49]. Independent of the choice of tracking algorithm, a maximum linking distance (MLD) can be set to reject the linking of MBs that would result in unrealistic flow velocities.

2-3-1 Local search methods

Errico *et al.* [12] and Christensen-Jeffries *et al.* [26] were the first to apply tracking of MBs in ULM to attain velocity information of individual microbubbles. Their methods are have

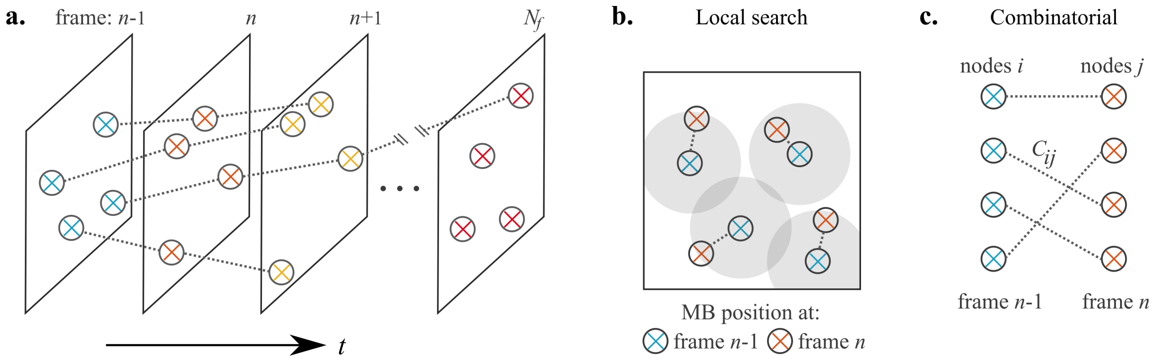

Figure 2-5: The MB tracking problem visualized. (a) MB tracking is performed by linking MB positions of consecutive frames. (b) In local search methods the linking is performed one-by-one. For each MB position in frame $n-1$ a close MB position in the next frame is sought. (c) Combinatorial methods rely on linking the MBs frame-to-frame. The linking of all MB positions of two consecutive frames is considered at the same time allowing to find a solution that minimizes the total linking cost. C_{ij} denotes the cost of linking node i of frame $n-1$ to node j of frame n.

in common that MB linking is performed on a local basis, see Figure 2-5(b).

The method applied by Christensen-Jeffries *et al.* [26] makes use of the cross-correlation between the MB images $I_{MB}(x,z,n-1)$ and $I_{MB}(x,z,n)$ within a local search window. A cross-correlation threshold was determined empirically to identify MB detections of consecutive frames corresponding to the same physical MB.

Errico *et al.* [12] made use of a Nearest Neighbour algorithm to link MBs of consecutive frames. This Nearest Neighbour algorithm selects for each MB the closest MB detection in the next frame to continue the track. The assumption that the closest MB detection in the next frame corresponds to the same target MB is reasonable for slow MB velocities and/or high frame rates [50].

However, in several situations this assumption might fail: high MB velocity or low frame rate, high MB concentration and branching or crossing of vessels. Two vessels that lie within the elevational width of the imaging slice can appear to cross each other on the reconstructed image, while in fact they run in different planes.

Furthermore, these methods do not allow gaps to be present in tracks. A track is terminated when no linking to a detection of the next frame can be made, resulting in short tracks that systematically underestimate MB lifetimes. The main advantage of local search methods is their computational simplicity.

2-3-2 Combinatorial methods

In contrast to local search methods, combinatorial methods perform the MB linking on a frame-to-frame basis. All MB positions are linked at the same time by minimizing a combined cost that is based on the distances between the MBs of consecutive frames [51].

For each set of two frames a linear assignment problem (LAP) is formulated. The MB positions of two consecutive frames can be represented by a bipartite graph with two groups of nodes, see Figure 2-5(c). The LAP consists in assigning each node to a single node of the other set, while minimizing a designed cost function. MB positions of the two frames that are assigned to each other are indicated by an entry of 1 in the assignment matrix A of size (N_{n-1}, N_n), where N_{n-1} and N_n represent the number of MBs in frame $n-1$ and n respectively. The LAP is given by [51]

$$\hat{A} = \arg\min_{A} \sum_{i=1}^{N_{n-1}} \sum_{j=1}^{N_n} A_{ij} C_{ij} \tag{2-5}$$

such that

$$\sum_{i=1}^{N_{n-1}} A_{ij} = 1 \quad \text{and} \quad \sum_{j=1}^{N_n} A_{ij} = 1 \tag{2-6}$$

where C is a cost matrix where the entry C_{ij} gives the cost of linking the i^{th} MB localization of frame $n-1$ with the j^{th} MB localization of frame n. This cost can be given by the distance between the localizations [52] or the squared distance [53]. Additionally, one could include cutoffs in the cost matrix to exclude MB pairing that are physically unlikely. A cutoff can be applied the same for all MBs by assumed a maximum blood flow [52] or it can be customized for each MB by taking into account the previous displacements of the MB [51]. Solving the LAP results in the minimal total cost solution and therefore a spatially global solution is attained. The constraints of (2-6) are added to ensure that each localization of frame $n-1$ is only linked to a single localization of frame n and vice versa.

The Kuhn-Munkres algorithm can be used to efficiently solve balanced assignment problems (i.e. $N_{n-1} = N_n$) for which each node needs to be assigned [54]. Due to its high computational efficiency, the Kuhn-Munkres algorithm both applied in 2D ULM [52] [1] as well as in 3D ULM [53]. However, an extension to the algorithm is needed to allow no-balanced assignment problems, for which the number of nodes in one group does not equal that in the other. Besides that, even if a balanced LAP is attained between two frames, not necessarily all localizations should be paired. The extension should thus allow to terminate and start new tracks.

Song *et al.* [52] proposed a bipartite graph-based assignment algorithm that only assigned two nodes to each other when the corresponding cost was mutually minimal. A localization remained unpaired, ending the track, when no such mutually minimal pairing distance could be found.

Jaqaman *et al.* [51] proposed an two-step algorithm based on LAPs to improve temporal globality. First, small track segments were formed using similar LAPs as introduced above. Second, the track segments were paired on a spatially and temporally global basis by an additional LAP. The initial frame-to-frame linking does not allow gaps in the formed tracks segments, resulting in an underestimation of the track length. The second step was included to allow gaps to be present, improving the temporal globality. Allowing gaps in MB trajectories is especially relevant for *in vivo* acquisitions, where MBs could temporarily move out of the imaging slice or could be undetected for some frames due to a spatial overlap with another MB.

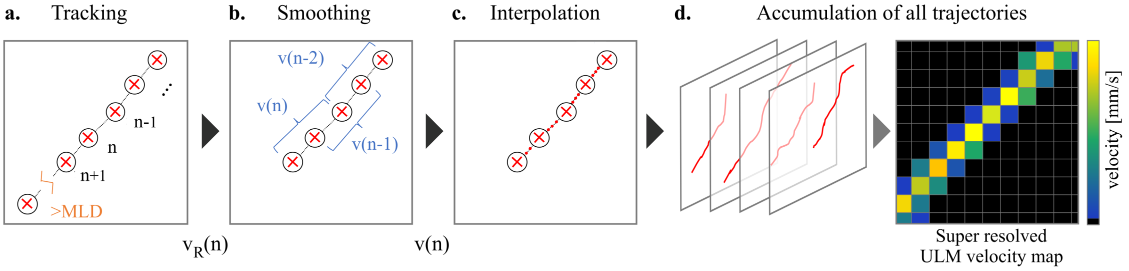

Figure 2-6: The rendering of MB trajectories consists of three steps: smoothing, interpolation and accumulation. (a) A MB trajectory is formed by linking localizations of consecutive frames. The maximum linking distance is applied at this stage in the process. From the found track, raw velocity measurements $v_{\mathrm{R}}(n)$ are obtained. (b) Smoothing of the trajectory by a moving average filter of span $s = 3$. (c) Spatial interpolation of the trajectory results in additional data points (red dot). (d) From the accumulation of all trajectories super resolved ULM reconstructions can be found.

2-4 Rendering

The processing steps applied to render a ULM reconstruction from the found MB trajectories are described by the following subsections, a visualization is added in Figure 2-6.

2-4-1 Trajectory smoothing

From the found trajectories, the raw velocity measurements u_n can be obtained by applying the backward Euler method as

$$u_n = \frac{\sqrt{(\hat{x}_n - \hat{x}_{n-1})^2 + (\hat{z}_n - \hat{z}_{n-1})^2}}{dt} \tag{2-7}$$

where the euclidean distance between the localizations $(\hat{x}_n, \hat{z}_n)$ and $(\hat{x}_{n-1}, \hat{z}_{n-1})$ is divided by the time step dt. Besides the magnitude of the received velocity vector, also its orientation θ can be retrieved. Due to localization errors, the raw velocity measurements generally have a noisy behaviour. Trajectory smoothing is applied to counteract the deteriorating effect of the localization errors. Smoothed velocity measurements u_n^{f} can be obtained by applying the moving average filter as [1]

$$u_n^{\mathrm{f}} = \frac{1}{s} \sum_{i=n-\lfloor s/2 \rfloor}^{n+\lfloor s/2 \rfloor} u_i \tag{2-8}$$

where the span s (in number of frames) is chosen odd and $\lfloor \cdot \rfloor$ represent the floor operation. A more detailed discussion on the moving average filter and its influence on the velocity measurements can be found in Section 3.

An alternative method for smoothing MB trajectories based on the Kalman filter was introduced by Tang *et al.* [49]. The state of the MB given by its position and velocity was recursively estimated for each frame n based on the previous localizations. The localization error distribution was assumed to be zero-mean Gaussian noise. The motion of the MB was approximated with a linear motion model. Performing this state estimation with the Kalman filter resulted in smoothed trajectories, for which both the measured velocity and the MB location was updated.

2-4-2 Spatial interpolation

The sampling rate of the MB trajectories corresponds to that of the acquired B-mode frames. Due to this temporal sampling the intermediate locations between two MB localizations of the same track are not observed. Interpolation of the MB trajectories is used to fill in the corresponding gaps resulting in improved image quality [49].

Note that for increasing MB velocities with respect to the frame rate, the interpolation becomes increasingly beneficial due to the larger gap between consecutive MB locations. Interpolation can be performed on a temporal [38, 52] or spatial basis [49]. Spatial interpolation is preferred for appropriate filling of the gaps caused by MBs travelling at different speeds. Spatial interpolation aims for the interpolated points between two MB localizations to be equally distanced. It thus allows the number of interpolated points to vary according to the travelled distance between two MB localizations. The spatial interpolation factor should be adjusted to the size of the grid at which a super resolved reconstruction is made [49].

2-4-3 Density reconstruction

A super-resolution (SR) density reconstruction can be obtained by accumulating the interpolated MB trajectories on a SR grid of chosen pixel size. The intensity of a SR pixel in the ULM density map is given by the number of MBs that have passed that pixel [38]. If two or more interpolated MB locations of the same track lie within the same pixel, only one is counted in the density reconstruction. Since the density map displays MB count, it can be regarded as a 2D histogram, in which the SR pixel size represents the bin size.

Even though it is tempting to reconstruct the density map on a very fine SR grid to display small details, one should note the following two disadvantages. First, the smaller the reconstructed pixel size, the more MB trajectories are necessary to sufficiently fill the vessel. The minimum number of necessary trajectories is given by the diameter of the vessel over the super resolution pixel size [38]. When inspecting a ULM density map, one should keep in mind that it may not always correctly represent the underlying vessel structure. The diameter of a vessel can be heavily underestimated when it is occupied by relatively little trajectories [34].

Secondly, a very small SR pixel size does not give a correct representation of the localization precision σ with which the ULM localizations are found. In fact, for decreasing SR pixel size one can be less certain that the MB actually passed the corresponding pixel. Since localization precision can not be measured *in vivo* due to the absence of ground truth data, one can rely on previous studies to estimate an expected value [1] or lower bound [12, 55]. A commonly used SR pixel size is 10 μm.

When utilizing a very coarse grid, the potential of the ULM reconstruction to resolve small structures is not fully utilized. In fact it results in a more pixelated version of the ULM reconstruction, in which vessel diameter might be overestimated.

2-4-4 Velocity reconstruction

The velocity reconstruction is found from the smoothed and interpolated trajectories in a similar manner. Instead of counting the number of MBs that passed a pixel, their velocity measurements are averaged [1]. The pixel value in a ULM velocity reconstruction thus corresponds to the average velocity observed in that pixel. It is due to the averaging performed here that pulsatility can generally not be observed in ULM velocity maps. Only when a trajectories is not overlayed by another trajectory, in which case no averaging is performed, a fluctuation in flow could theoretically be discovered in the ULM reconstruction.

2-5 Motion correction

Motion correction is crucial in most *in vivo* acquisitions to eliminate image blurring due to motion artifacts. During acquisition, motion can be prevented by physically restraining the organ to be imaged [34]. This is often done for preclinical brain imaging by stabilizing the animals head by a stereotaxic instrument [56]. However, when imaging organs that are affected by respiratory motion, physical restraint is inapplicable. Tissue motion between two consecutive frames can be detected by inspecting the normalized cross-correlation [50]

$$C(n) = \frac{\sum_x \sum_z I(x,z,n) I(x,z,n+1)^*}{\sqrt{\sum_x \sum_z I(x,z,n) I(x,z,n)^* \cdot \sum_x \sum_z I(x,z,n+1) I(x,z,n+1)^*}} \tag{2-9}$$

Note that (2-9) results in a scalar that represents the similarity between the frames at n and $n+1$. The higher the motion between two frames, the lower their $C(n)$. Frames of high tissue motion can be rejected when their cross-correlation score is below a set threshold, e.g. 0.98 [26]. It is assumed that when large tissue motion is observed through a low cross-correlation score, it will be accompanied by out-of-plane motion. Motion that is directed out of the imaging slice can not be corrected for and therefore the frame can best be discarded. For breathing motion, this results in a cyclic rejection of frames according to the respiratory cycle[50].

In the frames that are kept, the motion between two consecutive frames, or blocks of frames [56] is detected. The offset caused by in-plane rigid tissue motion can be detected by spatial cross-correlation [57]. Alternatively, elastic tissue motion can be detected by fitting an affine transformation between the coordinate frames of two consecutive frames [50, 58]. Once the motion is detected, it can be corrected for by mapping the localizations found in a motion affected frame to the coordinates of a fixed reference frame.

To prevent moving MBs affecting the tissue motion estimation, the SVD method [41] discussed in 2-1 can be used to only preserve the image resulting from tissue signal [56] [50], which is then used in the motion correction methods.

Chapter 3

Retrieving pulsatility in ultrasound localization microscopy

This chapter presents the findings of this study in a manuscript format. The manuscript was formatted in the style of *IEEE Open Journal on Ultrasonics, Ferroelectrics, and Frequency Control*.

Retrieving pulsatility in ultrasound localization microscopy

Myrthe Wiersma[1,2], Baptiste Heiles[1], Dylan Kalisvaart[2], Carlas S. Smith[2*], David Maresca[1*]

***Abstract*—Ultrafast ultrasound localization microscopy (ULM) is a super-resolved vascular imaging method that provides a 10-fold improvement in resolution compared to ultrafast ultrasound Doppler imaging. Because typical ULM acquisitions accumulate large numbers of synthetic microbubble (MB) tracks over hundreds of cardiac cycles, transient hemodynamic variations such as pulsatility get averaged out. Here we introduce two independent processing methods to retrieve pulsatile flow information from MB tracks sampled at kilohertz framerates and demonstrate their potential on a simulated dataset. Our first approach filters out ULM localization grid artifacts and successfully recovers the pulsatility fraction P_f with a root mean square error of 3.3%. Our second approach relies on the derivation of the velocity distribution of MBs as observed from a stationary observer. We show that pulsatile flow gives rise to a bimodal velocity distribution with peaks indicating the maximum and minimum velocity of the cardiac cycle. Measuring the locations of these peaks, we successfully estimated P_f with an error of 5.2%. Last, we evaluated the impact of the MB localization precision σ on our ability to retrieve the bimodal signature of a pulsatile flow. Together, our results demonstrate that pulsatility can be retrieved from high framerate ULM acquisitions and that the estimation of the pulsatility fraction improves with MB localization precision.**

***Index Terms*—ultrasound localization microscopy, pulsatility, localization precision, velocity distribution**

I. INTRODUCTION

THE resolution of conventional ultrasound images is limited by the wavelength (λ) dependent Rayleigh diffraction limit [1] while imaging depth is inversely proportional with λ, leading to a fundamental trade-off between image resolution and investigation depth. Recently, this trade-off has been circumvented by the introduction of ULM. This super-resolution vascular imaging technique relies on the localization of sub-wavelength contrast agent [2]. By accumulating thousands of agent positions with sub-wavelength precision, a vascular image can be reconstructed with a 10-fold resolution improvement compared to conventional ultrasound while retaining the same imaging depth. ULM has been demonstrated in vitro [3]–[6], in preclinical imaging [7]–[11] as well as in the clinic [12]–[14], in 2D and in 3D [15]–[17].

To date, ULM relies on synthetic ultrasound contrast agents made of polydisperse gas-filled microbubbles (MBs). Currently, ULM reconstruction algorithms rely on the hypothesis that individual MBs can be localized with sub-wavelength precision. Individual MBs are typically tracked over frames at kilohertz frame rates. The MB positions in subsequent frames can thus be linked together, forming tracks that reveal the underlying vascular architecture. ULM images are then rendered using either the density of MBs per each pixel, blood velocity measurements, or other metrics associated with morphological features such as tortuosity, vessel orientation, or main flow direction.

Because MB tracks are accumulated over hundreds of cardiac cycles, fast flow fluctuations are averaged out in ULM velocity maps. In other words, the velocity displayed is a measure of the average velocity over the entire ULM acquisition. An intuitive approach to speed up ULM acquisition consists in enabling the localization of dense MB populations as localizing larger numbers of MBs per frame reduces the total number of frames accordingly. However, this poses a new imaging trade-off between acquisition time and MB localization precision. Huang *et al.* [18] proposed to increase the MB sparsity via post-processing methods. They separated MB echoes into subpopulations using a spatiotemporal fourier filter. Each subpopulation was then individually processed using a conventional ULM reconstruction. Alternatively, machine learning-based approaches for MB localization were show to be able to handle higher MB concentrations by disentangling the interference pattern of spatially overlapping MBs [19]–[21].

In this study, we investigated the possibility of retrieving pulsatility from conventional ULM datasets without any change in the acquisition pipeline. Rather than aiming to decrease the acquisition time to reconstruct ULM maps faster, we hypothesized that the high temporal sampling of MB trajectories contains enough information to retrieve pulsatility. We report two methods capable of retrieving pulsatility from raw ULM data. The first method follows a Lagrangian description of the flow. Using a single MB velocity measurement, it relies on filtering to retrieve the pulsatility fraction in the reconstructed tracks. The second method follows a Eulerian description of the flow. The temporal distribution of velocities found at a fixed location in space is calculated. The pulsatility fraction was extracted from the bimodality of the velocity distribution. We validated both methods on simulated data generated using a ULM simulator that incorporates pulsatility waveforms recorded experimentally in rat cortical brain vessels [22].

II. METHODS

The ULM simulation pipeline is described in II-A and pulsatility retrieval methods are described in II-B. We provide a list of symbols in Appendix A.

---

[1] Department of Imaging Physics, Delft University of Technology, Delft, The Netherlands, [2] Delft Center for Systems and Control, Delft University of Technology, Delft, The Netherlands, *these authors contributed equally

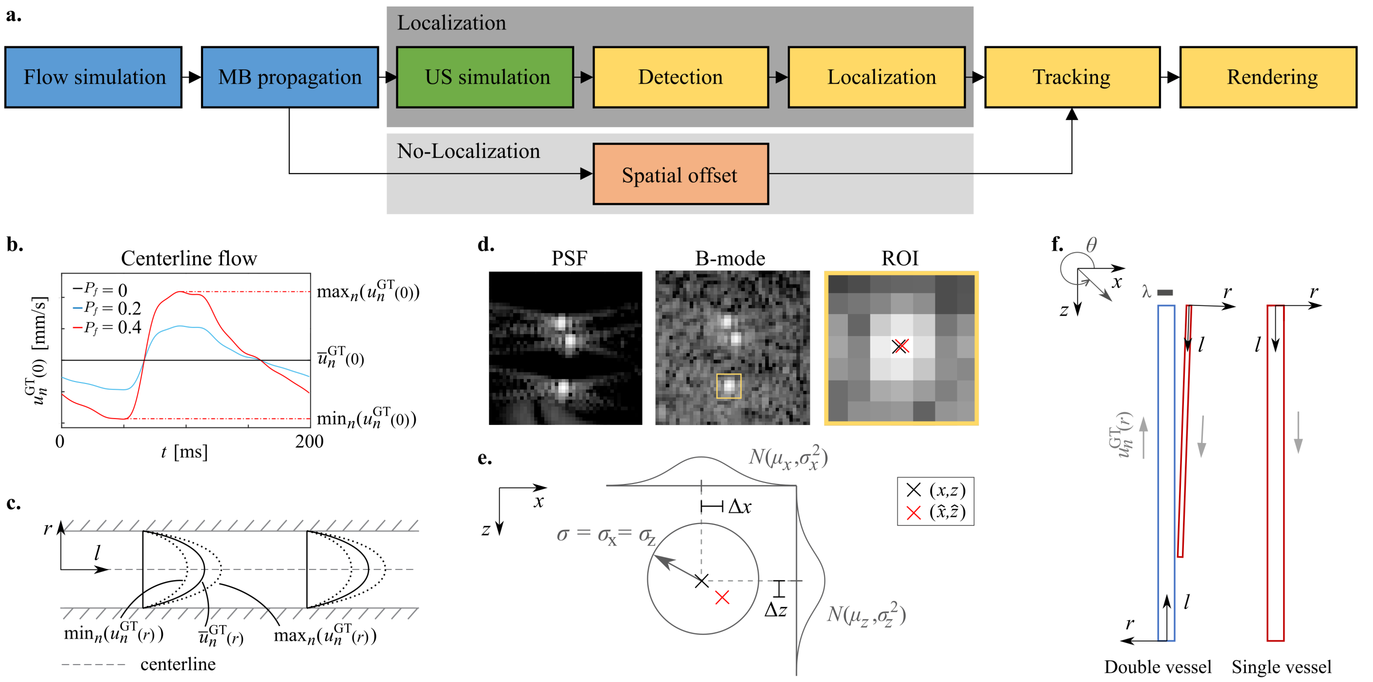

Fig. 1. Simulation study pipeline. (a) Our simulator enabled two simulation scenarios: Localization and No-Localization. (b) Simulated ground truth flow $u_n^{\mathrm{GT}}(0)$ at the centerline ($r = 0$) for three values of P_f and a pulsatility frequency of 5 Hz. Flow profiles extracted from [22]. (c) A rigid vessel with a parabolic flow profile is assumed. r and l are respectively the axial and lateral coordinates. Flow is independent of l. (d) Two steps of US simulation: first the point spread functions (PSF) of the MBs are simulated. Second, a B-mode image is generated by adding speckle. Estimation of the MB position in a region of interest (ROI). The ground truth MB position (x, z) and the estimated position $(\hat{x}, \hat{z})$ are given by the black and red cross respectivel. (e) In the No-Localization scenario a localization error $(\Delta x, \Delta z)$ is sampled from two normal distributions and added to the ground truth MB position (x, z) to obtain the estimated MB position $(\hat{x}, \hat{z})$. Localization precision σ is controlled. (f) The double vessel and single vessel configurations showing a vein (blue) and arteries (red). Simulation parameters in Table I. The local coordinates are defined at the inlet of the vessel. The vessel orientation angle θ is defined with respect to the x-axis in the counter clockwise direction.

A. ULM simulator design

The designed ULM simulator is presented in Fig. 1(a) and can be used for two simulation scenarios: the 'Localization' and 'No-Localization' scenarios.

1) Localization scenario: The Localization scenario mimics all steps of an experimental ULM acquisition (Fig. 1(a)) and consists of three main modules: a module simulating the MB positions (in blue), a module simulating ultrasound frames (in green) and a module performing ULM processing (in yellow).

In the first module, the ground truth flow $u_n^{\mathrm{GT}}(r)$ was simulated by modeling its temporal and spatial characteristics separately, with r the lateral coordinate and n the time index.

The temporal behavior of the flow at the centerline of the vessel ($r = 0$) was modelled following *in vivo* observations by Santisakultarm *et al.* [22] in rat cortical brain vessels (Fig. 1(b)). The pulsatility fraction is defined as the difference between the maximum and minimum flow velocity over the average flow velocity at a fixed location in the vessel

$$P_f = \frac{\max_n(u_n^{\mathrm{GT}}(r)) - \min_n(u_n^{\mathrm{GT}}(r))}{\bar{u}_n^{\mathrm{GT}}(r)} \quad (1)$$

where $\bar{u}_n^{\mathrm{GT}}(r)$ denotes the temporal average. To construct the pulsatile flow at the centerline of the vessel $u_n^{\mathrm{GT}}(0)$ we retrieved the temporal average $\bar{u}_n^{\mathrm{GT}}(0)$, P_f and the shape of the pulsatile cycle from the results reported in [22]. The frequency of pulsatility was fixed at a typical rat heartbeat of 300 bpm. Fig. 1(b) shows the simulation of $u_n^{\mathrm{GT}}(0)$ for three different values of P_f corresponding to a steady-state flow ($P_f = 0$) a pulsatile flow in a vein ($P_f = 0.2$) and in an artery ($P_f = 0.4$).

We calculate the flow $u_n^{\mathrm{GT}}(r)$ for a given temporal sampling $n = {}^{t}/_{dt}$, from $u_n^{\mathrm{GT}}(0)$ following two assumptions on the spatial characteristics of the flow. First, $u_n^{\mathrm{GT}}(r)$ is assumed to be dependent on the lateral coordinate r only, corresponding to the rigid vessel-hypothesis. Second, the flow velocity profile along r is assumed to be parabolic, corresponding to Poiseuille flow [23]. Therefore, $u_n^{\mathrm{GT}}(r)$ is obtained by fitting a parabola to the simulated centerline velocity $u_n^{\mathrm{GT}}(0)$ and the vessel diameter d. We found that simulating flow by modeling the temporal and spatial behavior separately was in good agreement with the Womersley solution for pulsatile flow in rigid pipes [24].

MB positions during the acquisition were simulated by initializing and propagating a fixed number of point scatterers in the vessel. The axial MB coordinate r was uniformly sampled along the vessel length L. The lateral MB coordinate l was sampled from a distribution of parabolic shape found by normalization of the parabolic velocity profile $u_n^{\mathrm{GT}}(r)$. The MBs were propagated to the next frame using the local simulated flow velocity and the timestep dt. An outlet condition was implemented so that once an MB left the vessel, a new MB was initialized at the inlet. The lateral coordinate r of this new MB was drawn from the parabolic distribution while the axial coordinate was drawn from a uniform distribution on the interval $[0, u_n^{\mathrm{GT}}(r)dt)]$.

In the second module, the Verasonics Research Ultrasound Simulator (VRUS, Verasonics, Kirkland, WA, USA) was used to simulate the ultrasound B-mode frames at 1kHz [25]. The L22-14vX probe (Vermon, Tours, France) was simulated to transmit a single plane wave at 0° with pulse duration of 2 cycles and a main frequency of 17.6 MHz. The Verasonics Reconstruction software was used to beamform the Radio-Frequency data. Additional parameters can be found in Appendix A, Table A.2. To improve computational efficiency the frames were constructed in two steps as shown in Fig. 1(d). The speckle patterns were simulated by placing 10^5 weaker scatterers of random intensity at a uniform random position in the field of view. As the simulation time in VRUS depends on the number of scatterers placed in the medium, 3×10^4 simulated speckle frames were generated and microbubble response was simulated *a posteriori*. The MB response was simulated taken as the response of a subwavelength scatterer and was simulated as if the MBs were to flow in a homogeneous medium without speckle, resulting in a frame with a few point spread functions (PSF). A speckle pattern was randomly selected from the set of simulated speckle frames and added to the PSF frame. The signal-to-noise ratio (SNR) of the resulting image can be controlled by setting the intensity of the speckle pattern. An average SNR of 14 dB was simulated.

In the third module, we performed ULM processing on blocks of 1000 simulated frames using the LOTUS toolbox [25]. We optimized ULM parameters based on the visual improvement of the microvessel reconstruction. Their values are provided in Appendix A, Table A.3. We applied an SVD filter to filter the simulated B-mode frames. Since no static tissue is present in our simulation, the SVD filter was solely applied to reduce speckle noise. For localization of the MBs we used the radial symmetry algorithm, due to its high performance and low computation time in mid-to-low-SNR scenarios [25] [26]. We calculated MB tracks using a Kuhn-Munkres assignment [27] and computed the corresponding raw velocity measurements $u_n(r)$ by a backward Euler method [7]. We smoothed MB tracks using a moving average filter to generate the velocity measurements $u_n^{\mathrm{f}}(r)$ [25] and rendered these tracks on a super resolved grid to reconstruct the velocity map. Additionally, a density map was constructed by finding the MB count for each pixel and a flow orientation θ map was constructed, with θ the angle between the x-axis and the direction of flow (in counter clockwise direction).

2) No-Localization scenario: In the No-Localization simulation scenario a spatial offset mimicking a MB localization error is added to the ground truth MB positions simulated by the first module (orange section in Fig. 1(a)). The MB positions with added localization errors are then fed to the tracking module (Fig. 1(e)). The localization errors in x and z direction were assumed independent and identically distributed (IDD) as $\mathcal{N}(0, \sigma^2)$, with σ the localization precision. This simulation scenario allows us to investigate the effect of localization precision on retrieval of pulsatility since σ can be directly controlled. It should be noted that in practice, different localization algorithms lead to different shapes and mean values of localization error distributions [25].

TABLE I

SIMULATION CONFIGURATION PARAMETERS

Parameter	Double vessel configuration		Single vessel configuration
Vessel type	Vein	Artery	Artery
d	100 μm	30 μm	100 μm
L	2mm	1.5 mm	2 mm
θ	$^1/_2\pi$	$^3/_2\pi$ - 0.027	$^3/_2\pi$
$\bar{u}_n^{\mathrm{GT}}(0)$	9 mm/s	8.57 mm/s	20.57 mm/s
P_f	0.2	0.4	0.4
average nr. of MBs	2	1/4	1
Vessel separation distance	50-10 μm		-
Acquisition time	40 s		40 s
Simulation scenario	Localization		No-Localization

3) Simulation configurations: We defined two distinct microvascular configurations as illustrated in Fig. 1(f), with specific simulation parameters provided in Table I. For both configurations the simulated flow characteristics matched that of *in vivo* observations [22].

The double vessel configuration mimics the *in vivo* configuration of cortical brain vessels. Here, the vascular architecture consisted of a straight 30 μm wide descending artery and a straight 100 μm wide ascending vein that converge towards each other. We used this configuration in combination with the Localization simulation scenario to evaluate the performance of our ULM simulator.

The second configuration consisted of a single 100 μm wide straight artery and was used in combination with the No-Localization simulation scenario. This configuration enables us to assess the performance of the pulsatility retrieval methods for different values of the localization precision σ.

B. Methods to retrieve pulsatility in ULM data

In this section, we introduce two methods for pulsatility retrieval in ULM data.

1) Single-track velocity filtering: In this first method to recover pulsatility, the raw velocity measurements of individual MB tracks were filtered. Raw velocity measurements $u_n(r)$ are found by dividing the traveled distance over one frame by the time-step, also known as the backward Euler method [7]. Raw velocity measurements are strongly impacted by the localization errors in the MB positions. We filtered tracks using a moving average filter defined as

$$u_n^{\mathrm{f}}(r) = \frac{1}{s} \sum_{\mathrm{i}=n-\lfloor s/2 \rfloor}^{n+\lfloor s/2 \rfloor} u_{\mathrm{i}}(r) \tag{2}$$

where s is the span of the moving average filter and $\lfloor \cdot \rfloor$ is the floor operation. Note that the span is expressed in number of frames and should be chosen as an odd number such that an equal number of raw velocity measurements before and after frame n are included. It dictates the time window over which the $u_n(r)$ is averaged. Its value is therefore dependent on the imaging frame rate. Here, s should be compared to the 200 frames covering one simulated pulsatile cycle (5Hz, dt=1ms). Grid-based artifacts appear in the velocity measurements when localization is dependent on the MB position within the

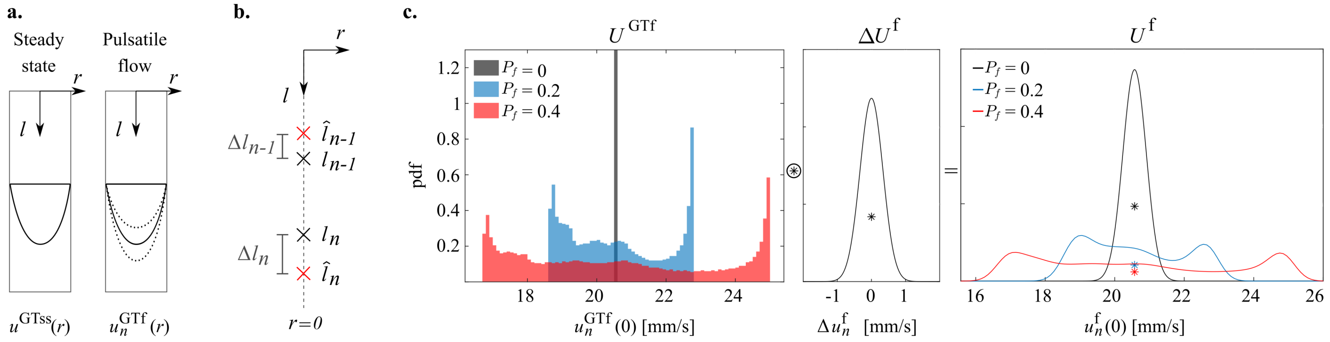

Fig. 2. Pulsatility retrieval method based on the accumulation of velocity measurements. (a) For derivation purposes, the steady-state and pulsatile flow case were considered. In the former the flow $u^{\mathrm{GTss}}(r)$ is independent of the time index n. (b) Illustration of two MB positions l_n and l_{n-1} localized with localization errors Δl_n and Δl_{n-1} respectively. Only the localization error along the axial coordinate l is considered. (c) Derivation of the distribution U^{f}. The distribution U^{GTf} is found by the histogram of the smoothed ground truth flow $u_n^{\mathrm{GTf}}(0)$ at the centerline of the vessel. By convolution with the smoothed velocity error distribution ΔU^{f} we derive U^{f}. Here, the derivation is performed for the single vessel configuration for three different values of P_f and with $\sigma = 5$ μm and $s = 21$. The maximum and minimum flow can be detected by the peaks in U^{f}.

beamformed pixel of size dx. A MB of constant steady-state velocity $u^{\mathrm{ss}}(r)$ passes a beamformed pixel every $dx/u^{\mathrm{ss}}(r)$, i.e. with frequency $f_{dx} = u^{\mathrm{ss}}(r)/dx$. Track velocity measurements should inhibit this same frequency in case of grid-dependent MB localization, since they are computed directly from MB positions. Here, the simulated MBs move along with the pulsatile flow $u_n^{\mathrm{GT}}(r)$. Therefore f_{dx} corresponds to a range of frequencies as

$$f_{dx} = \frac{u_n^{\mathrm{GT}}(r)}{dx} \tag{3}$$

We inspected the frequency spectrum of $u_n(r)$ to assess the presence of these frequency-dependent grid-based artifacts. To filter out the artifacts which could not be eliminated by using the moving average filter, we applied a bandstop filter as a pre-filtering step. We set the stopband corresponding to the derived f_{dx} range. After frequency filtering we applied the moving average filter with span of 51 frames to improve both the retrieval of the velocity extremes as well as the visual appearance of the tracks. We defined the velocity measurements obtained from our designed filtering process as $u_n^{\mathrm{f}}(r)$.

We implemented this pulsatility retrieval method on tracks measured in the double vessel simulation for the Localization scenario. The pulsatility fraction was calculated on the filtered single-track velocity measurements. To retrieve the maximum and minimum velocity measured during a track the average of three points centered around respectively the local maximum and local minimum was taken.

2) Accumulation of track velocities as observed by a stationary observer: We introduce a second method of retrieving pulsatility that relies on the accumulation of measured velocities in a fixed lateral position r in the vessel. As multiple MBs go through the same super-resolution pixel during a ULM acquisition, multiple velocity measurements are found in each pixel. The average of these measurements is reported in a conventional ULM velocity map.

In the following, we calculated the distribution of the measured velocities at a fixed r for a fully one-dimensional flow along the axial coordinate l. For simplicity we start the derivation by considering a steady-state flow, i.e. $u_n^{\mathrm{GT}}(r) = u^{\mathrm{GTss}}(r)$, after which the case of a pulsatile flow is considered, see Fig. 2(a).

For steady-state flow, we assume that the spread in measured velocities is solely caused by error in MB localization. Consider two linked MBs at frame n and $n-1$ as illustrated in Fig. 2(b). Each estimated MB position $\hat{l}_n$ along axial coordinate l is given by the ground truth MB position l_n with an added localization error Δl_n, i.e. $\hat{l}_n = l_n + \Delta l_n$. The raw velocity measurement at frame n is then given as

$$\begin{aligned} u_n(r) &= \frac{\hat{l}_n - \hat{l}_{n-1}}{dt} && (4)\\ &= \frac{l_n - l_{n-1}}{dt} + \frac{\Delta l_n - \Delta l_{n-1}}{dt} && (5)\\ &= u_n^{\mathrm{GT}}(r) + \Delta u_n && (6) \end{aligned}$$

where Δu_n is the velocity error caused by error in MB localization. We assume Δl_n and Δl_{n-1} to be independent and identically distributed (IID) as $\mathcal{N}(0, \sigma^2)$, σ being the localization precision. The distribution of the raw velocity error Δu_n can be found by a combination of the two independent normal distributions, resulting in $\Delta U \sim \mathcal{N}\left(0, \frac{2}{dt^2}\sigma^2\right)$.

The raw velocity measurements of a track are smoothed by a moving average filter. Substitution of (5) in (2) for general odd-numbered s results in the smoothed velocity measurement as

$$\begin{aligned} u_n^{\mathrm{f}}(r) &= \frac{1}{s} \sum_{\mathrm{i}=n-\lfloor s/2 \rfloor}^{n+\lfloor s/2 \rfloor} u_{\mathrm{i}}^{\mathrm{GT}}(r) \\ &\quad + \frac{1}{s\,dt}\left(\Delta l_{n+\lfloor s/2 \rfloor} - \Delta l_{n-\lfloor s/2 \rfloor - 1}\right) \qquad (7)\\ &= u_n^{\mathrm{GTf}}(r) + \Delta u_n^{\mathrm{f}} \end{aligned}$$

where $u_n^{\mathrm{GTf}}(r)$ is the smoothed ground truth flow and Δu_n^{f} the smoothed velocity error resulting from localization error. The distribution of the smoothed velocity error is found to be $\Delta U^{\mathrm{f}} \sim \mathcal{N}(0, \sigma_u^2)$, where $\sigma_u = \frac{\sqrt{2}}{s\,dt}\sigma$. In the steady-state scenario, where the first term of (7) can be replaced by $u^{\mathrm{GTss}}(r)$, we find the smoothed velocity measurements at a fixed lateral location r to be distributed as $U^{\mathrm{f}} \sim \mathcal{N}(u^{\mathrm{GTss}}(r), \sigma_u^2)$.

In a pulsatile flow, the smoothed ground truth flow $u_n^{\mathrm{GTf}}(r)$ does not equal the steady state flow $u^{\mathrm{GTss}}(r)$. The distribution of $u_n^{\mathrm{f}}(r)$ for pulsatile flow is then found to be $U^{\mathrm{f}} \sim \mathcal{N}\left(u_n^{\mathrm{GTf}}(r), \sigma_v^2\right)$. Two effects cause the spread in this distribution. Similar to the steady-state case, the variance σ_u is caused by the localization error. In contrast to the steady-state case, an additional spread due to a varying mean $u_n^{\mathrm{GTf}}(r)$ is caused by the pulsatile flow behaviour. The distribution U^{GTf} of the varying mean can be approximated by creating a histogram of $u_n^{\mathrm{GTf}}(r)$ over one pulsatility cycle, as in Figure 2(c). Assuming $u_n^{\mathrm{GTf}}(r)$ to be independent of Δu_n^{f} we find the distribution of $u_n^{\mathrm{f}}(r)$ in pulsatile flow to be

$$U^{\mathrm{f}} = U^{\mathrm{GTf}} \circledast \Delta U^{\mathrm{f}} \tag{8}$$

where $\circledast$ represents the convolution operation. In Fig. 2(c) the derivation is performed for three different values of P_f for a fixed σ and s. By employing the moving average filter, it is implicitly assumed that $u_n^{\mathrm{GTf}}(r) \approx u_n^{\mathrm{GT}}(r)$. The span s should be small enough compared to the pulsatile period for this assumption to hold.

The minimum and maximum values of $u_n^{\mathrm{GTf}}(r)$ are given by the peaks in the histogram U^{GTf}. After convolution, these peaks appear in U^{f} as well. In ULM acquisitions U^{f} can be found by the accumulation of the smoothed velocities found at a fixed lateral location r. The pulsatility fraction can be estimated by substitution of the found peaks in (1).

III. RESULTS

The results presented here are divided into three sections. We first report the performance of the simulator, then the simulation results of the first pulsatility retrieval method that relies on the filtering of single MB tracks, and finally theoretical and simulation results found from the application of the second method of retrieving pulsatility.

A. The full ULM process is simulated and super-resolution is achieved

An average velocity map was reconstructed from the simulation of the flow in the double vessel configuration in Fig. 3. This average velocity map serves as the ground truth with which the ULM velocity reconstruction should be compared. Fig. 3(b) displays a simulated B-mode image containing three MBs.

Based on the acquired B-mode images, a contrast-enhanced Power Doppler image is computed (Fig. 3(c)), and the ULM pipeline for localization and tracking is implemented resulting in three super-resolved maps displaying density (Fig. 3(d)), velocity (Fig. 3(e)) and orientation (Fig. 3(f)). The cross-sections of the ULM density map and Power Doppler image taken at 3 different positions along the axial direction are plotted in Fig. 3(g). The two vessels can be separated as close as 15 μm ($\sim \lambda/5.8$), well below the wavelength of $\lambda = 86.2$ μm. Separation of the vessels is also possible in the velocity based renderings (Fig. 3(h)). Finally, the orientation map displays a clear separation of the two vessels of opposite flow using a color code for the orientation of the velocity vector, the vein appearing in blue and the artery in red. The root mean square error (RMSE) of the average blood flow velocity and orientation are 1.3 mm/s and 0.23 rad respectively.

Histograms of the found localization errors in Δx and Δz are plotted in Fig. 3(i). The localization precisions σ_x and σ_z were 8.5 μm and 12.7 μm respectively and are within the same range as reported in [25], i.e. $[0.09, 0.23]\lambda = [7.76, 19.83]$ μm.

B. Pulsatility fraction can be recovered from single tracks by filtering out grid-based artifacts

Three lateral vessel locations r_1, r_2 and r_3 were defined, corresponding to the center of the vein, the side of the vein, and the center of the artery in the double vessel configuration. Tracks at these lateral locations were found by controlling the inlet position of simulated MBs, see Fig. 4(a) and (b). ULM parameters were adjusted to recover long tracks that span almost the entire length of the vessels.

The presence the periodical grid-based artifact was noticed upon post-processing via a moving average filter with a span $s = 51$. At the position r_2, this is clearly visible by the sawtooth-like behavior of Fig. 4(c) and was also visible at other positions. Increasing the span s did not result in elimination of this artifact which can be seen in Fig. B.1 of Appendix B.

The frequency spectrum of the track at r_2 was computed with a Fast Fourier Transform (Fig. 4(d)). A frequency peak is clearly visible in the frequency range f_{dx} at which a simulated MB passes a beamformed pixel (computed from (3) and indicated as the gray shaded region). This peak was also found for different beamformed pixel sizes and is always in the f_{dx} frequency range (Fig. B.2 of Appendix B). This artifact is referred to as a beamforming grid-based artifact in the rest of this manuscript.

The filtered velocity measurements found by pre-filtering with the bandstop filter and smoothing with the moving average filter are shown in 4(e). The pulsatility fraction estimates calculated from the found maximum and minimum velocities are given in Fig. 4(f).

The RMSE of the pulsatility fraction estimates at r_1, r_2 and r_3 are 0.022, 0.056 and 0.013, which corresponds to 11%, 28% and 3.3% of the simulated pulsatility fraction respectively.

C. The ability to retrieve pulsatility from the measured velocity distribution is dictated by σ and s

1) Theoretical results: The theoretical velocity distributions corresponding to the single vessel configuration are given in Fig. 5(a). The calculation was performed for different values of σ and a fixed moving average span of $s = 21$. In Fig. 5(b) and 5(c) the calculation was repeated for pulsatility fraction of $P_f = 0.2$ and $P_f = 0$.

Pulsatility introduces a bimodal velocity distribution for sufficiently low σ. For $P_f = 0.4$ two peaks could be retrieved for $\sigma \leq 20$ μm, while for $P_f = 0.2$ this was possible for $\sigma \leq 10$ μm. The maximum and minimum velocity during the pulsatile cycle were retrieved from the location of these peaks and a pulsatility fraction estimate $\hat{P}_f$ as given in Fig. 5(a)-(c) was computed. No bimodality was found in the distribution

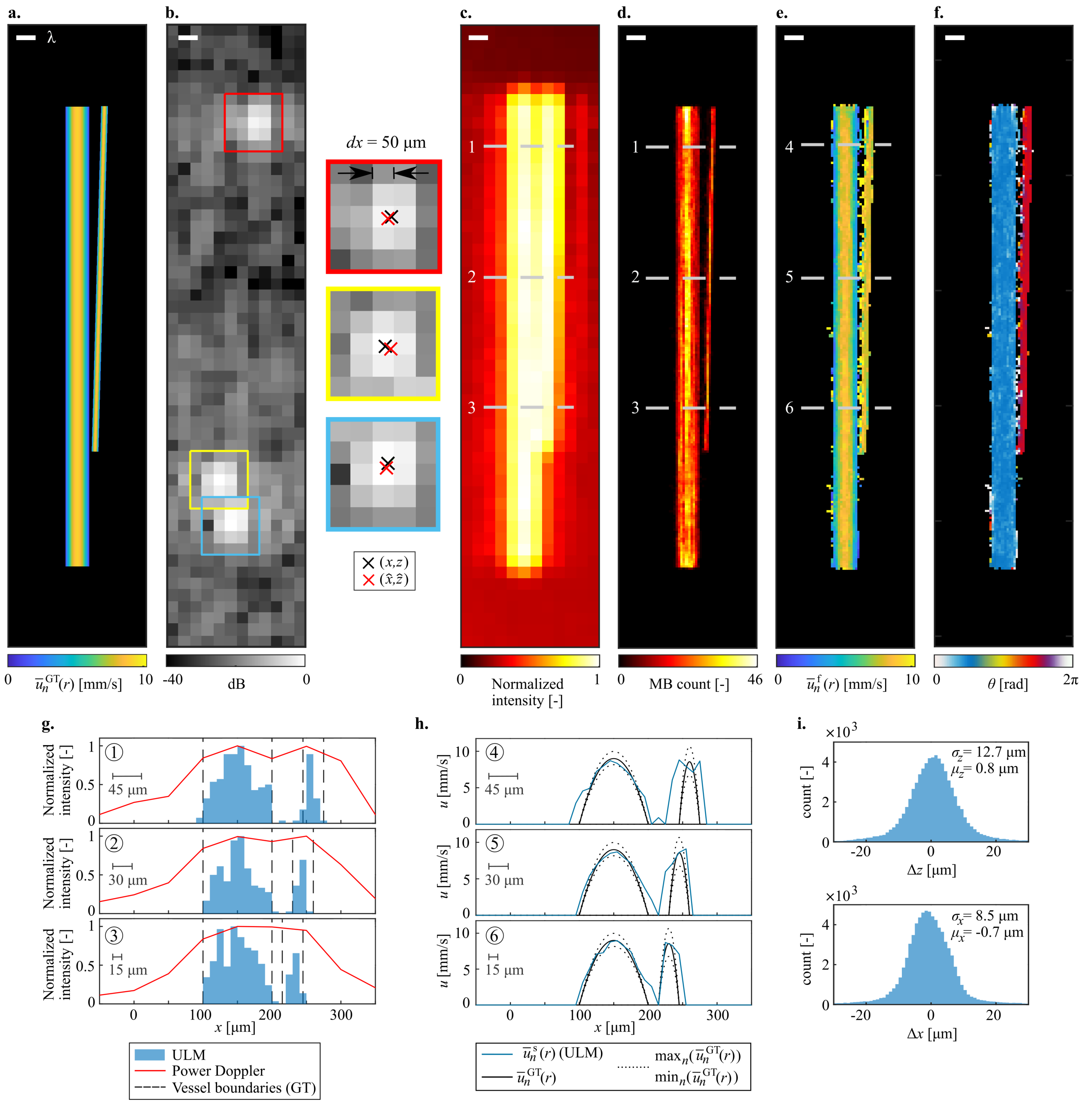

Fig. 3. Simulation of the double vessel configuration with the designed ULM simulator shows its ability to simulate the full ULM processing pipeline and achieve super-resolution. Length of all scalebars = λ (a) The simulated average bloodflow $\bar{u}_n^{\mathrm{GT}}(r)$ serves as the ground truth with which the ULM velocity map is to be compared. (b) A patch of a simulated B-mode image with 3 MBs at position (x, z) beamformed at 50 μm $\approx \lambda/2$. In the regions of interest, the MB position estimates $(\hat{x}, \hat{z})$ are found using the radial symmetry localization algorithm. (c) Diffraction-limited Power Doppler rendering with cross-sections 1,2 and 3 at which the vessels have a separation distance of respectively 45, 30 and 15 μm. (d) ULM density rendering. (e) ULM velocity rendering. (f) ULM orientation rendering. (g) Cross-sections (1)-(3) of the ULM density rendering and Power Doppler image. (h) Cross-sections (4)-(6) of the ULM velocity rendering (i) Histograms for measured localization errors Δx and Δz for a total of 29417 localized MBs.

of the steady-state flow case. The location of the centroid of the distribution (asterisks) indicates the mean $\bar{u}_n^{\mathrm{GTf}}(r)$. When rendering the MB trajectories to a ULM reconstruction this mean value is obtained and displayed in the velocity map. $\bar{u}_n^{\mathrm{GTf}}(r)$ is the same for all distributions given in Fig. 5(a)-(d).

From the derivation in II-B2 it was already found that increasing the span s narrows ΔU^{f}. This effect was also found in U^{f} when comparing Fig. 5(a) with Fig. 5(d) with respectively $s = 21$ and $s = 51$. We find that increasing the span aids the retrieval of the bimodality. In Fig. 5(b) two peaks could still be retrieved for $\sigma = 30$ μm.

The localization precision σ has a large influence on the distributions. For increasing σ we find the peaks to move

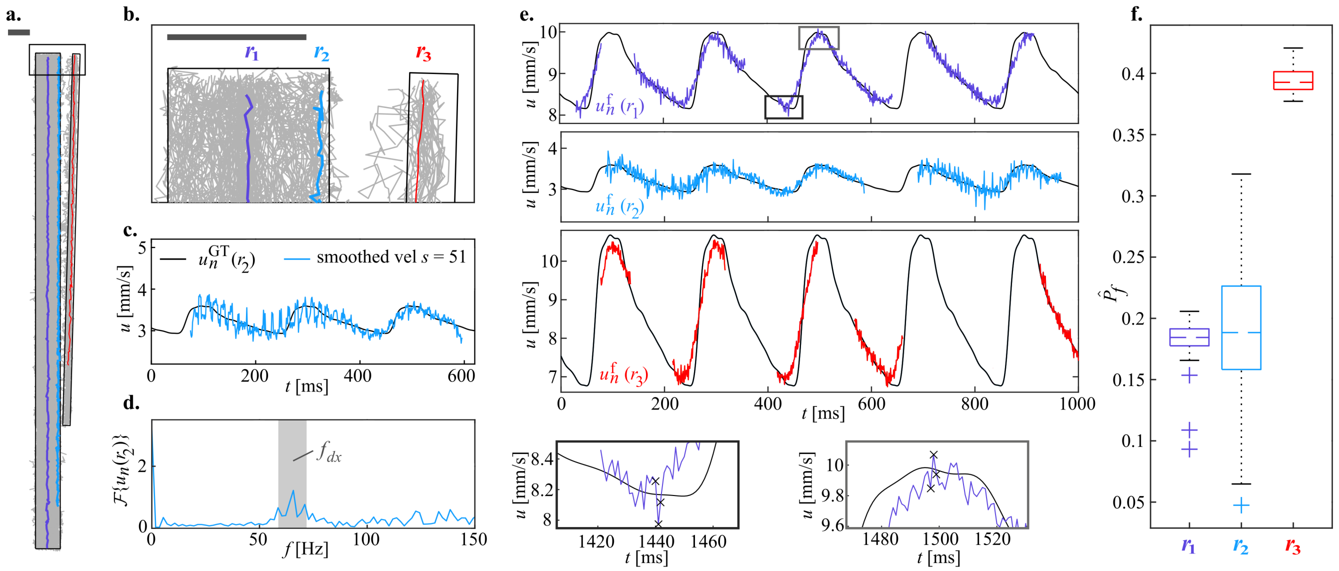

Fig. 4. Pulsatility can be retrieved by filtering single-track velocity measurements. (a)-(b) Three tracks at different lateral positions r_1, r_2, and r_3 in the two vessels are highlighted. Scalebar = λ (c) The smoothed velocity measurements at r_2 show a disturbance with periodical behavior. (d) The frequency spectrum of the raw velocity measurements at r_2 shows a peak at frequencies corresponding to the frequency range f_{dx} (grey). (e) The frequency filtered velocity measurements $u_n^{\mathrm{f}}(r)$ follow the simulated ground truth velocity $u_n^{\mathrm{GT}}(r)$. Multiple tracks for each lateral location are shown. (f) From the filtered measurements of (e) P_f is estimated.

slightly inwards and the distribution to flatten until no two peaks can be detected any longer. To further study this, Fig. 5(e) plots the pulsatility fraction as a function of σ for a fixed value of the span $s = 21$. The theoretical pulsatility fraction is indicated as a dashed line. We find that P_f is always underestimated. A deteriorated localization precision results in a higher underestimation of P_f, well in accordance to what is observed in Fig. 5(a)-(d). For $\sigma > 20$ μm only a single peak was detected and thus, no $\hat{P}_f$ was found.

The span of the moving average filter s has a large influence on the height of the velocity distribution peaks. For increasing s, the peaks are heightened. By comparing Fig. 5(a) and (d) we find the peaks to move inwards for higher s. To further study this, Fig. 5(f) plots the pulsatility fraction as a function of the span s for a fixed value of σ. Multiple lines are included that represent distinct σ values. The calculation was performed up to $s = 51$. Similarly as described in the previous paragraph, $\hat{P}_f$ is underestimated for all the scenarios. The smallest theoretical attainable estimation error is found at the maxima of the curves for each value of σ. With this approach an optimal setting of s can be derived for any obtained localization precision σ, as is shown in Fig. 5(f). The curves show that a lower localization precision (higher σ) requires a larger span s to enable retrieval of the pulsatility fraction.

2) Simulation results: The velocity distributions as derived in Fig. 5(a) were acquired in simulation for $\sigma = 5$, 10 and 20 μm (single vessel No-Localization). The resulting histograms are given in Fig. 6. The peaks of the distributions found in both cases are in good accordance. The simulations for $\sigma = 5$ μm and for $\sigma = 10$ μm result in the same peak locations for the bin size of the histogram used here.

Additionally, the method was applied to the same data set as used in Fig. 4, where the double vessel configuration was simulated with the Localization scenario. Histograms were obtained by accumulation of velocity measurements at the lateral coordinates r_1, r_2 and r_3, see Fig. 6(b). In the center of the vein (r_1), we found $\hat{P}_f = 0.143$ which is an underestimation of 28.6%. It was needed to increase the moving average span to 31 frames for retrieval of bimodality. In the histogram found for r_2 no bimodality could be retrieved despite further increasing the span. In the center of the artery (r_3) a pulsatility fraction estimate of 0.379 corresponding to 5.2% underestimation was found. Bimodality was already achieved at $s = 21$. Using the first method we achieved a RMSE of 3% and 11% for respectively the artery and the vein. We find that pulsatility retrieval is best performed at the centerline of the vessel.

IV. DISCUSSION

In this study, we introduced two methods to retrieve flow pulsatility with ULM. The first method retrieves pulsatility from raw ULM data by filtering out grid-based artifacts from single-track velocity measurements. The second method relies on the accumulation of velocity measurements at a fixed location in the microvessel of interest. With this approach, the pulsatility fraction could be retrieved from the location of the two peaks in the bimodal velocity distribution. To validate these methods, we modelled pulsatility in arteries and veins from experimental data and used the Verasonics Research Ultrasound Simulator to generate ultrasound B-mode frames. The low computation time of this simulator (as reported in Appendix A) compared to k-space-based simulators makes it suitable for large dataset generation. Our results show that ULM datasets contain rich temporal information that can be processed to retrieve pulsatility in addition to conventional ULM image reconstructions. By relying on the high frame

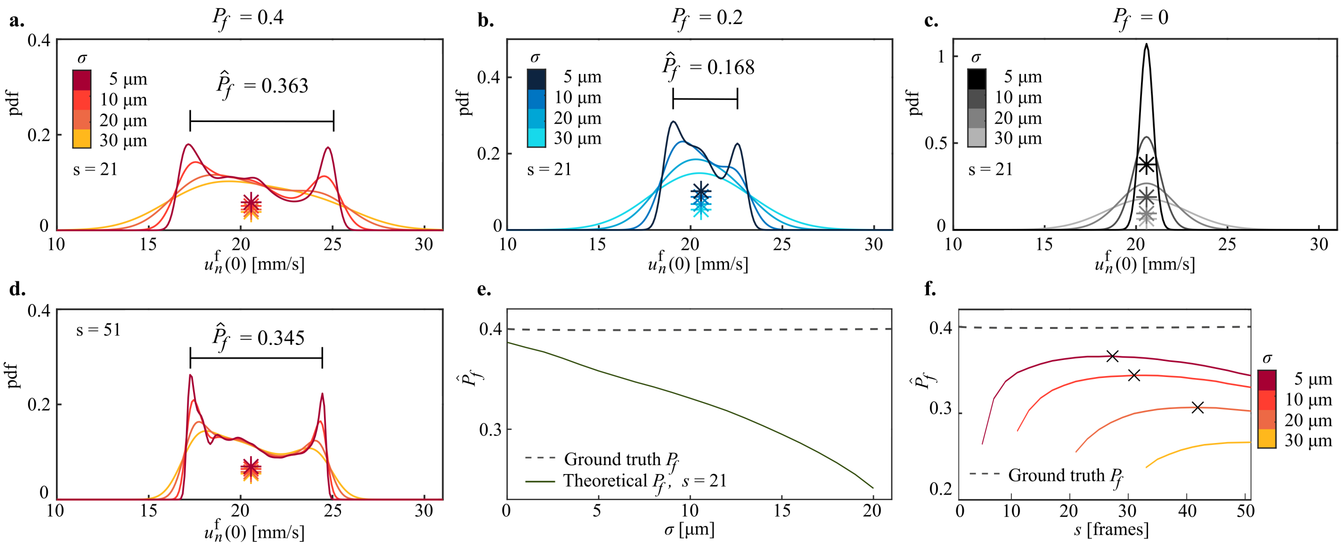

Fig. 5. Pulsatility fraction can be retrieved from the bimodal shape of the velocity distribution. The results shown here correspond to the parameters of the single vessel configuration. (a) The derived velocity distributions for different values of σ with fixed $s = 21$. $\hat{P}_f$ can be found from the location of the two peaks in the distribution. Centroids of the distribution are given by asterisks and represent the conventional ULM measurement. (b)-(c) Similar derivation for $P_f = 0.2$ and $P_f = 0$ respectively. (d) The derivation of (a) was repeated for $s = 51$. (e) The effect of localization precision σ on $\hat{P}_f$ for fixed s. The line stops when no two peaks could be detected. (f) The effect of s on $\hat{P}_f$ for a fixed σ. The different lines correspond to different σ values. A maximum (cross) can be found corresponding to the optimal value of s. Derivation was performed up to $s = 51$.

rate, we were able to retrieve the temporal dynamics induced by pulsatility without changing the localization, concentration, or tracking of the ULM processing pipeline.

Our derived velocity distributions were validated in simulation. The peak loations in the acquired histograms (Fig. 6) closely match those derived theoretically (Fig. 5). The larger presence of high velocities in the histograms acquired from the simulation is expected to be a results of the spatial interpolation of the tracks. A MB of higher velocity travels a longer distance on a frame-to-frame basis, causing its velocity to be accumulated in the velocity distribution of multiple pixels. We hypothesize that this effect is beneficial to the retrieval of pulsatility since it causes the peak corresponding to the maximum velocity to be more prominent. The derivation of U^{f} should be updated to include this effect. Pulsatility induces bimodality in the distribution of smoothed velocity measurements U^{f} (Fig. 5). Localization precision σ dictated both the ability to find a P_f estimate as well as the quality of that estimate. In the derivation of U^{f} the MB localization error was assumed to be normally distributed as $\sim \mathcal{N}(0, \sigma^2)$, which does not generally hold for all localization algorithms [25].

In the first reported method, both the pre-filtering by the bandstop filter and the smoothing by the moving average filter were found critical to retrieve pulsatility from single tracks. In the raw velocity measurements, we observed a large presence of noise resulting from MB localization error. In the simulation of the double vessel configuration, we obtained σ values higher than the average distance traveled by the MBs over one frame, 12.7 μm versus $3.3, 9.0$ and 8.6 μm for r_1, r_2 and r_3 respectively. Additionally, we discovered the presence of beamforming grid-based artifacts in single-track velocity measurements caused by grid-dependent localization, as shown in Fig. 4(c). The presence of these artifacts is consistent for different beamformed pixel sizes dx and for localization using both a radial symmetry and a Gaussian fitting algorithm (Fig. B.2). Applying the single-track filtering method to a data set without speckle for which no SVD filter was applied, validated that the artifacts are indeed a result of beamforming (Fig. B.3).

This first method relies on the temporal sampling of a track. For each track, it will recover a pulsatility fraction using (1). In the case of slow MBs - at the side of the vein for example - trajectories spanning hundreds of consecutive frames could be found (Fig. 4(e)). The main factor limiting the trajectory length in our simulation was the time during which the MB was present in the vessel. Acquisition of long MB tracks is therefore crucial in the first method. The tracks in Fig. 4(e) succeed each other every ∼100 frames. Due to the sparsity of *in vivo* MB data the intervals between two succeeding tracks are expected to be longer.

The second method does not rely on a Lagrangian but an Eulerian description of the flow. Rather than looking at the tracks of each MB, it will explore the distribution of the velocities at a fixed spatial sample. Because it relies on the full acquisition time, we expect less dependency on the frame rate and on the retrieval of long MB tracks than the first method. In the calculation of U^{f} we noticed two possible effects a change in framerate might cause. First, the temporal discretization causes an additional numerical error in (6) that has not yet been taken into account. This numerical error will increase for decreasing frame rates. Second, the time-step dt influences the variance of the smoothed velocity error through $\sigma_u = \frac{\sqrt{2}}{s\ dt}$. When the span of the moving average filter is increased to match the original temporal window, this effect is neutralized.

The moving average filter was found to narrow the velocity

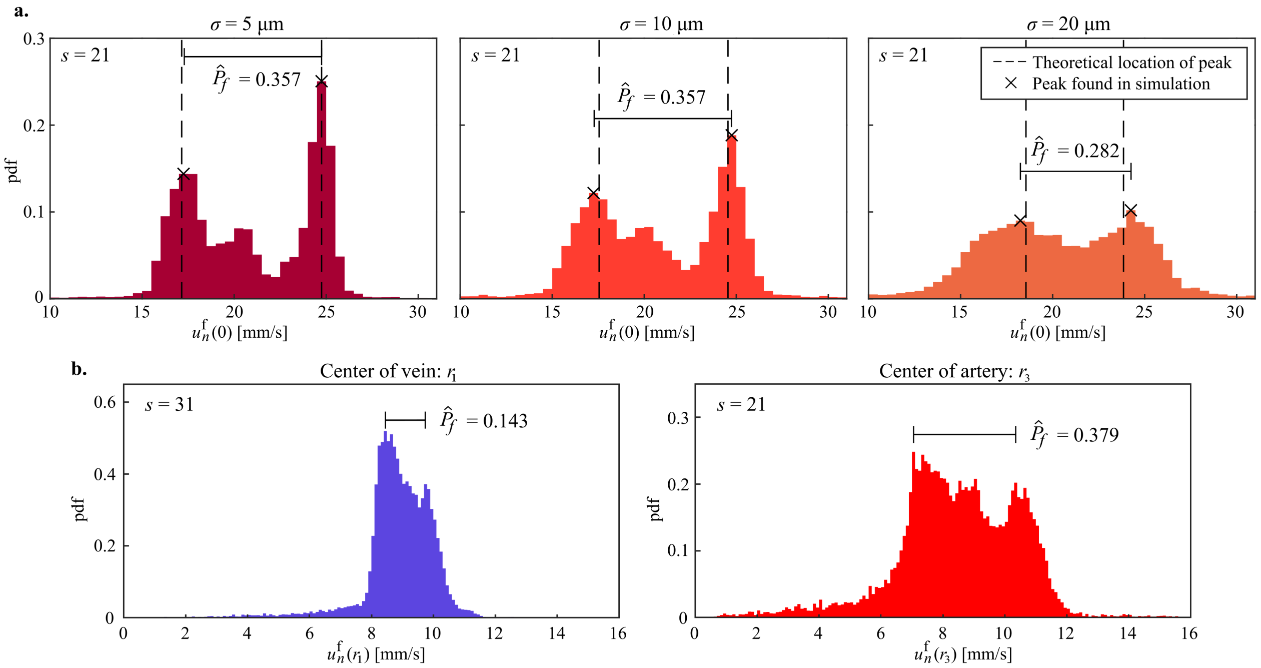

Fig. 6. Validation of the velocity distribution pulsatility retrieval method in simulation. (a) The histograms were constructed by collecting velocity measurements along the centerline of the vessel in the single vessel configuration for the No-Localization scenario. The theoretical location of the peak was extracted from derived U^{f} of Fig. 5(a). Bin size = 0.5 mm/s. (b) The acquired histograms for the double-vessel configuration with Localization. The same data set as in Fig. 4 was used. Bin size = 0.1 mm/s.

error distribution ΔU^{f} by dividing the standard deviation by the value of s. It therefore reduces the adverse effect of localization error on the velocity measurements. For estimation of a steady-state flow it is advised to use a large moving average span. However, beyond a certain point increasing the span has adverse effects on pulsatility retrieval. The heavy smoothing results in an increased underestimation of the pulsatility fraction due to the flattening of the pulsatile cycle (see Appendix C). This underestimation effect of the moving average filter is apparent in Fig. 5(e) where $s = 21$ was applied. Even for perfect localization ($\sigma = 0$ μm) pulsatility fraction was underestimated. Unfortunately,we can not rely on previous research for an appropriate range of s for *in vivo* applications, since these values are usually not reported. The theory introduced here can be used to determine an optimal setting of the moving average span for a specific flow scenario with given localization precision.

The occurrence of false MB pairing by the tracking algorithm will influence both methods. It will cause unexpected behavior of the filtered tracks (Fig. 4(e)) and introduce additional contributions to the measured velocity histogram (Fig. 6). To limit the adverse effect of false MB pairings, an appropriate tuning of the maximum linking distance in ULM tracking is necessary. The theoretical derivation of the velocity distribution performed in this study aids the development of a systematic method to determine the optimal maximum linking distance (Appendix D).

Pulsatility was simulated by our ULM simulator by modelling the spatial and temporal characteristics of the microvascular blood flow separately corresponding to a straight vessel with rigid wall of constant diameter. The ULM simulator could be improved by adapting a vascular architecture corresponding to *in vivo* observations.

By investigating the effect of MB localization precision on the retrieval of pulsatility, we focused on the spatial quality of MB tracks. Future research could focus on the temporal sampling of the MB tracks in relation to pulsatility reconstruction. We expect the minimum frame rate needed for resolving hemodynamics to depend mainly on the time scale of the targeted hemodynamic phenomena, which are usually in the tens of milliseconds to seconds timescale for hemodynamic events. The methods reported here will need to be tested on *in vivo* data. We anticipate specific challenges in an *in vivo* context, such as shorter MB tracks, sparser MB data, and more frequent false MB linkings.

V. CONCLUSION

We have introduced two methods to extract pulsatility from raw ULM datasets. First, by filtering out grid-based artifacts from single track velocity measurements, second, by retrieving the distribution of velocities measured at a fixed location in a vessel of interest. Both methods have been validated on simulated ultrasound beamformed data featuring pulsatility induced flow variations. Our study shows that ULM datasets contain more information on the hemodynamics of the blood flow than that provided by conventional ULM image reconstructions. By looking at reconstructed tracks independently or at the distribution of velocities, more insight can be gained into the hemodynamics experienced by the microbubbles.By reported by vascular anatomy and hemodynamic function, ULM has the potential of becoming a full-fledged ultrasound diagnostic method of unprecedented resolution.

ACKNOWLEDGMENTS

We acknowledge support from the TU Delft AI Labs Initiative, the Medical Delta Program Ultrafast Heart and Brain, and the 4TU program Precision Medicine. Baptiste Heiles is supported by a Marie Skłodowska-Curie postdoctoral fellowship from the European Commission (award number 101032769).

REFERENCES

[1] R.S.C. Cobbold, *Foundations of biomedical ultrasound*, Oxford university press, 2006.

[2] O. Couture, B. Besson, G. Montaldo, M. Fink and M. Tanter, ”Microbubble ultrasound super-localization imaging (MUSLI),” in *2011 IEEE International Ultrasonics Symposium*, pp. 1285-1287, 2011.

[3] O.M. Viessmann, R.J. Eckersley, K. Christensen-Jeffries, M.X. Tang, C. Dunsby, ”Acoustic super-resolution with ultrasound and microbubbles,” *Physics in Medicine and Biology*, vol. 58, no. 18, pp. 6447–6458, 2013.

[4] Y. Desailly, O. Couture, M. Fink, M. Tanter , ”Sono-activated ultrasound localization microscopy”, *Applied Physics Letters*, vol. 103, no. 17, pp. 174107, 2013.

[5] D. Ackermann, G. Schmitz, ”Detection and Tracking of Multiple Microbubbles in Ultrasound B-Mode Images,” *IEEE Transactions on Ultrasonics, Ferroelectrics, and Frequency Control*, vol. 63, no. 1, pp. 72–82, 2016.

[6] M.A. O’Reilly, and K. Hynynen, ”A super-resolution ultrasound method for brain vascular mapping,” *Med. Phys.*, vol. 40, no. 11, pp. 110701, 2013

[7] K. Christensen-Jeffries, R. J. Browning, M. Tang, C. Dunsby and R. J. Eckersley, ”In Vivo Acoustic Super-Resolution and Super-Resolved Velocity Mapping Using Microbubbles,” *IEEE Transactions on Medical Imaging*, vol. 34, no. 2, pp. 433–440, 2015

[8] C. Errico, J. Pierre, S. Pezet, Y. Desailly, Z. Lenkei, O. Couture and M. Tanter, ”Ultrafast ultrasound localization microscopy for deep super-resolution vascular imaging,” *Nature*, vol. 527, pp. 499–504, 2015.

[9] F. Lin F, S.E. Shelton, D. Espíndola, J.D. Rojas, G. Pinton, P. A. Dayton, ”3-D Ultrasound Localization Microscopy for Identifying Microvascular Morphology Features of Tumor Angiogenesis at a Resolution Beyond the Diffraction Limit of Conventional Ultrasound”, *Theranostics*, vol. 7, no. 1, pp. 196–204, 2017.

[10] J. Foiret, H. Zhang, T. Ilovitsh, L. Mahakian, S. Tam and K.W. Ferrara, ”Ultrasound localization microscopy to image and assess microvasculature in a rat kidney,” *Scientific Reports*, vol. 7, no. 1, pp. 13662, 2017.

[11] P. Song, J.D Trzasko, A. Manduca, R. Huang, R. Kadirvel, D.F. Kallmes and S. Chen, ”Improved Super-Resolution Ultrasound Microvessel Imaging With Spatiotemporal Nonlocal Means Filtering and Bipartite Graph-Based Microbubble Tracking,” *IEEE Transactions on Ultrasonics, Ferroelectrics, and Frequency Control*, vol. 65, no. 2, pp. 149–167,2018.

[12] T. Opacic, S. Dencks, B. Theek, M. Piepenbrock, D. Ackermann, A. Rix, T. Lammers, E. Stickeler, S. Delorme, G. Schmitz and F. Kiessling, ”Motion model ultrasound localization microscopy for preclinical and clinical multiparametric tumor characterization,” *Nature Communications*, vol. 9, no. 1, pp. 1527, 2018.

[13] S. Harput, K. Christensen-Jeffries, J. Brown, Y. Li, K.J. Williams, A.H. Alun, R.J. Eckersley, C. Dunsby and M. Tang, ”Two-Stage Motion Correction for Super-Resolution Ultrasound Imaging in Human Lower Limb,” *IEEE Transactions on Ultrasonics, Ferroelectrics, and Frequency Control*, vol. 65, no. 5, pp. 803–814, 2018.

[14] C. Demené, J. Robin, A. Dizeux, B. Heiles, M. Pernot, M. Tanter and F. Perren, ”Transcranial ultrafast ultrasound localization microscopy of brain vasculature in patients,” *Nature Biomedical Engineering*, vol. 5, no. 3, pp. 219—228, 2021.

[15] B. Heiles, M. Correia, V. Hingot, M. Pernot, J. Provost, M. Tanter and O. Couture, ”Ultrafast 3D Ultrasound Localization Microscopy Using a 32 × 32 Matrix Array,” *IEEE Transactions on Medical Imaging*, vol. 38, no. 9, pp. 2005–2015, 2019.

[16] B. Heiles, A. Chavignon, A. Berel, V. Hingot, H. Serroune, D. Maresca, S. Pezet, M. Pernot and M. Tanter, ”Volumetric ultrasound localization microscopy of the whole brain microvasculature,” in *bioRxiv*, 2021.

[17] O. Demeulenaere, A. Bertolo, S. Pezet, N. Ialy-Radio, B. Osmanski, C. Papadacci, M. Tanter, T. Deffieux and M. Pernot, ”In vivo whole brain microvascular imaging in mice using transcranial 3D Ultrasound Localization Microscopy,” *eBioMedicine*, vol. 79, pp. 103995, 2022.

[18] C. Huang, M.R. Lowerison, J.D. Trzasko, A. Manduca, Y. Bresler, S. Tang, P. Gong, U. Lok, P. Song and S. Chen, ”Short Acquisition Time Super-Resolution Ultrasound Microvessel Imaging via Microbubble Separation,” *Scientific Reports*, vol. 10, no. 1, 2020.

[19] R.J.G. van Sloun, O. Solomon, M. Bruce, Z. Z. Khaing, H. Wijkstra, Y. C. Eldar and M. Mishi, ”Super-Resolution Ultrasound Localization Microscopy Through Deep Learning,” *IEEE Transactions on Medical Imaging*, vol. 40, no. 3, pp. 829–839, 2021.

[20] L. Milecki, J. Porée, H. Belgharbi, C. Bourquin, R. Damseh, P. Delafontaine-Martel, F. Lesage, M. Gasse and J. Provost, ”A Deep Learning Framework for Spatiotemporal Ultrasound Localization Microscopy,” *IEEE Transactions on Medical Imaging*, vol. 40, no. 5, pp. 1428–1437, 2021.

[21] N. Blanken, J. M. Wolterink, H. Delingette, C. Brune, M. Versluis and G. Lajoinie, ”Super-Resolved Microbubble Localization in Single-Channel Ultrasound RF Signals Using Deep Learning,” in *IEEE Transactions on Medical Imaging*.

[22] T. P. Santisakultarm, N. R. Cornelius, N. Nishimura, A. I. Schafer, R. T. Silver, P. C. Doerschuk, W. L. Olbricht and C. B. Schaffer, ”In vivo two-photon excited fluorescence microscopy reveals cardiac- and respiration-dependent pulsatile blood flow in cortical blood vessels in mice,” *American Journal of Physiology-Heart and Circulatory Physiology*, vol. 302, no. 7, pp. H1367–H1377, 2012.

[23] Mair Zamir, *Physics of pulsatile flow*, Springer New York, 2000.

[24] J.R. Womersley, ”Method for the calculation of velocity, rate of flow and viscous drag in arteries when the pressure gradient is known,” *The Journal of Physiology*, vol. 127, pp. 553–563, 1955.

[25] B. Heiles, A. Chavignon, V. Hingot, P. Lopez, E.Teston and O. Couture, ”Performance benchmarking of microbubble-localization algorithms for ultrasound localization microscopy”, *Nature Biomedical Engineering, 2022*

[26] R. Partasarathy, ”Rapid,accurate particle tracking by calculation of radial symmetry centers,” *Nature Methods*, vol. 9, no. 7, pp. 724–728, 2012.

[27] H. W. Kuhn, ”The Hungarian method for the assignment problem,” *Naval Research Logistics Quarterly*, vol. 2, no. 1-2, pp. 83–97, 1955.

APPENDIX A

All symbols used in this study are given in Table A.1 along with their definition.

TABLE A.1
LIST OF SYMBOLS

Symbol	Definition
λ	Wavelength (in m)
x	Coordinate parallel to tissue surface (in m)
z	Coordinate perpendicular to tissue surface (in m)
r	Lateral local coordinate (in m)
l	Axial local coordinate (in m)
n	Time index or frame number
d	Vessel diameter (in m)
L	Vessel length (in m)
θ	Vessel or blood flow orientation w.r.t. the x-axis (CCW) (in rad)
dt	Timestep between two B-mode frames (in s)
dx	Beamformed pixel size (in m)
f_{dx}	Frequency range corresponding to a MB passing beamformed pixels (in Hz)
$(\hat{x}, \hat{z})$	Estimated MB position (in m)
Δx, Δz, Δl	MB localization error in x, z and l (in m)
μ_x, μ_z	Mean of localization error in x and z (in m)
σ_x, σ_z	Found localization precision in x and z (in m)
σ	Induced localization precision for simulation in the No-Localization scenario in x and z (in m)
P_f	Pulsatility fraction
$u_n^{\mathrm{GT}}(r)$	Ground truth flow (in m/s)
$u_n^{\mathrm{GTf}}(r)$	Filtered ground truth flow (in m/s)
$u^{\mathrm{GTss}}(r)$	Ground truth flow for steady-state scenario (in m/s)
$u_n(r)$	Raw velocity measurement (in m/s)
$u_n^{\mathrm{f}}(r)$	Filtered velocity measurement (in m/s)
$\Delta u_n(r)$	Error in raw velocity measurement induced by localization error (in m/s)
$\Delta u_n^{\mathrm{f}}(r)$	Error in smoothed velocity measurement induced by localization error (in m/s)
s	Span of moving average filter (in number of frames)
σ_u	Derived standard deviation of $\Delta u_n^{\mathrm{f}}(r)$ (in m)

TABLE A.2
US SIMULATION PARAMETERS

Parameter	Value
Transmit frequency	17.8571 MHz
Speed of sound	1540 m/s
Wavelength	86.2 μm
Frame rate	1 kHz
Probe	Verasonics L22-14v
Nr. of plane waves	1
Angle	0°
Nr. of transmit elements	128
Nr. of receive elements	128
Pitch	100 μm
Beamformed pixel size	50 μm

Total computation time of the ULM simulator was found on average 24 ms/B-mode frame excluding the time needed for computing the speckle frames. Therefore, simulating a ULM reconstruction of 10s acquisition time at 1kHz requires a total average computation time of 240s. The hardware specifications of the computer used in this study are given in Table A.4.

TABLE A.3
ULM PROCESSING PARAMETERS

Parameter	Value
Super resolved pixel size	10 μm
SVD threshold	[5,750]
FWHM	3×3 US pixels
Nr. of allowed local maxima	3
Maximum Linking Distance (MLD)	50 μm
Minimum track length	5 frames
Maximum gap closing distance	0 frames
Moving average span	21

TABLE A.4
HARDWARE SPECIFICATIONS

CPU	Intel Xeon W-2155, 10 cores @ 3.30 GHz
GPU	NVIDIA Quadro P2000, 10.5 GB

APPENDIX B

Increasing the moving average span did not eliminate the beamforming grid-based artifacts (Fig. B.1). Even at a span of 111 frames, which is more than half of the duration of the pulsatile cycle, the artifact is still observed.

The artifact is likely to be a result of MB localization that is dependent on the location in the beamformed pixel. In Fig. B.2 this is illustrated for a MB that moves at constant speed with localization biased towards the center of the pixel. The velocity measurements based on the estimated MB positions (red) will fluctuate between a high value measured for the MB crossing a pixel border and a low value measured for a MB at a central pixel location, see the gray arrows in the illustration.

To conclude that the artifact indeed results from this grid dependent localization, the simulation was performed on three different beamformed pixel sizes dx: 100 μm, 50 μm and 10 μm. The resulting spectra are shown in Fig. B.2 with the f_{dx} range given by the shaded area.

For $dx = 100$ μm and 50 μm a noticable peak is found within the f_{dx} range. In the case of a 10 μm pixel size, this is not observed. Note that this pixel size is approximately $\sim {}^{1}\!/_{10}\lambda$ and typical localization precisions that would be obtained are often larger than 10 μm [25].

To validate that the grid-based artifact does indeed result from beamforming and the applied SVD filter does not induce it, a simulation on PSF frames without any speckle was performed. In processing of this data, no SVD filter was applied. The results in Fig. B.3 show that the grid-based artifact is also present in this data set.

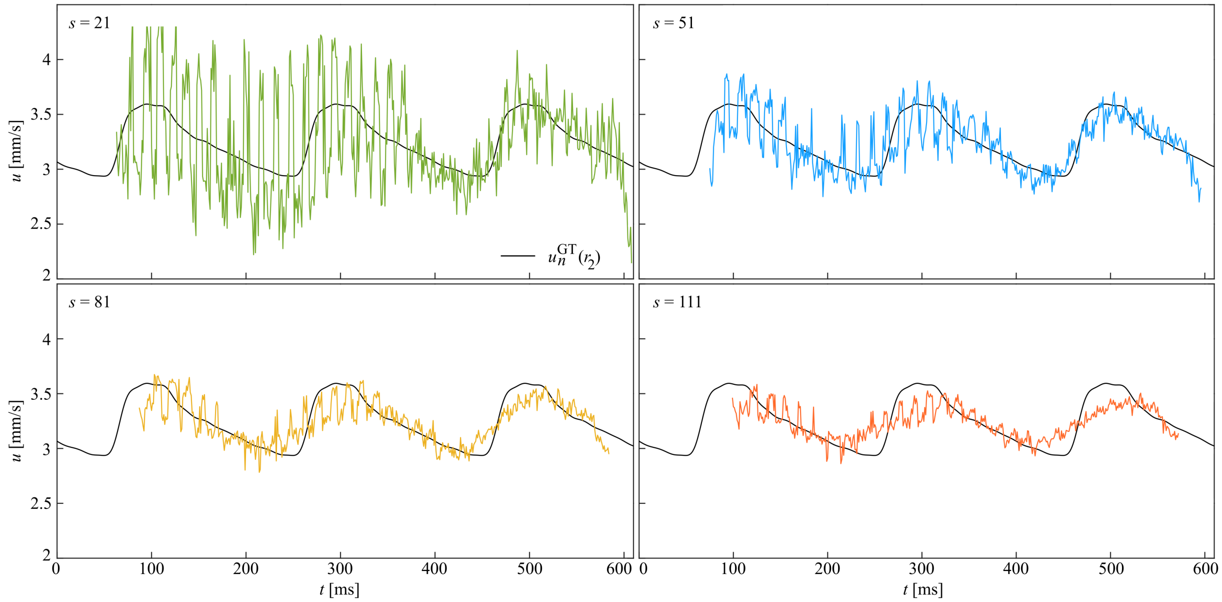

Fig. B.1. The periodical grid-based artifact found in single-track velocity measurements is not eliminated by increasing the span s (in number of frames). The smoothed velocity values of $s = 111$ still show the artifact while their shape is heavily altered by the heavy smoothing, resembling the effect shown in Fig. C.1(a).

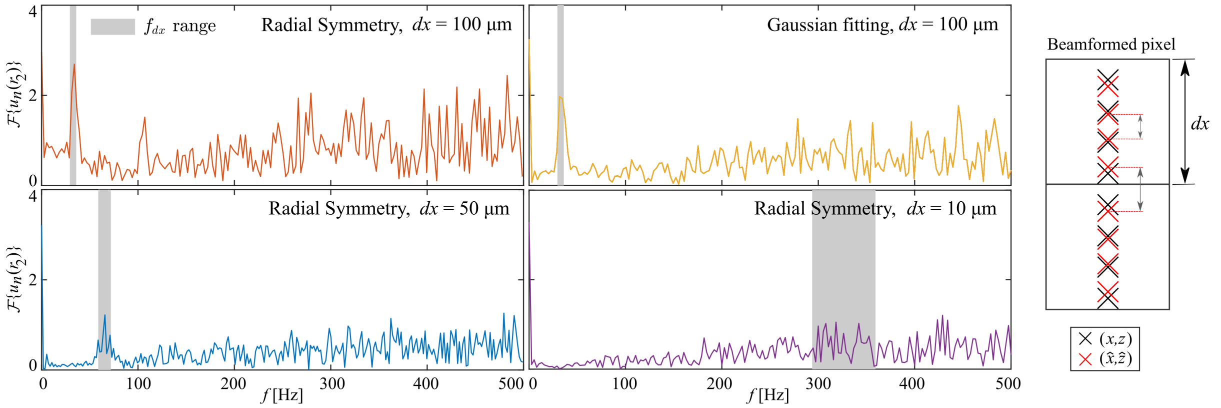

Fig. B.2. The frequency spectra of the raw single-track velocity measurements $u_n(r)$ are shown for simulations in which beamforming was perfomed on different pixel sizes dx. f_{dx} corresponds to the range of frequencies at which a MB passes a pixel. In the top row with $dx = 100$ μm, peaks lie within the frequency range f_{dx} for localization performed with a radial symmetry algorithm and with Gaussian fitting. In the bottom row a peak is visible in the f_{dx} range for $dx = 50$ μm. For $dx = 10$ μm $\sim 1/10\lambda$ the frequency range was not found to align with a distinct peak in the spectrum. On the right an illustration of the grid-based artifact is included. The distance between the estimated MB positions $(\hat{x}, \hat{z})$ is dependent on the ground truth MB location within (x, z) a beamformed pixel.

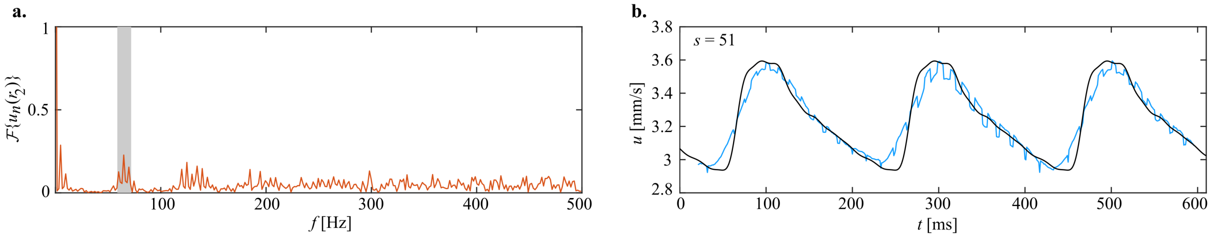

Fig. B.3. The grid-based artifact in a PSF simulation without speckle and without application of a SVD filter. (a) The frequency spectrum shows a peak corresponding with the f_{dx} region. Additionally, an increase in frequency content is found at $\sim 2f_{dx}$. (b) The track velocity measurements smoothed by a moving average filter with a span of 51 frames. A clear sawtooth-like behavior is found.

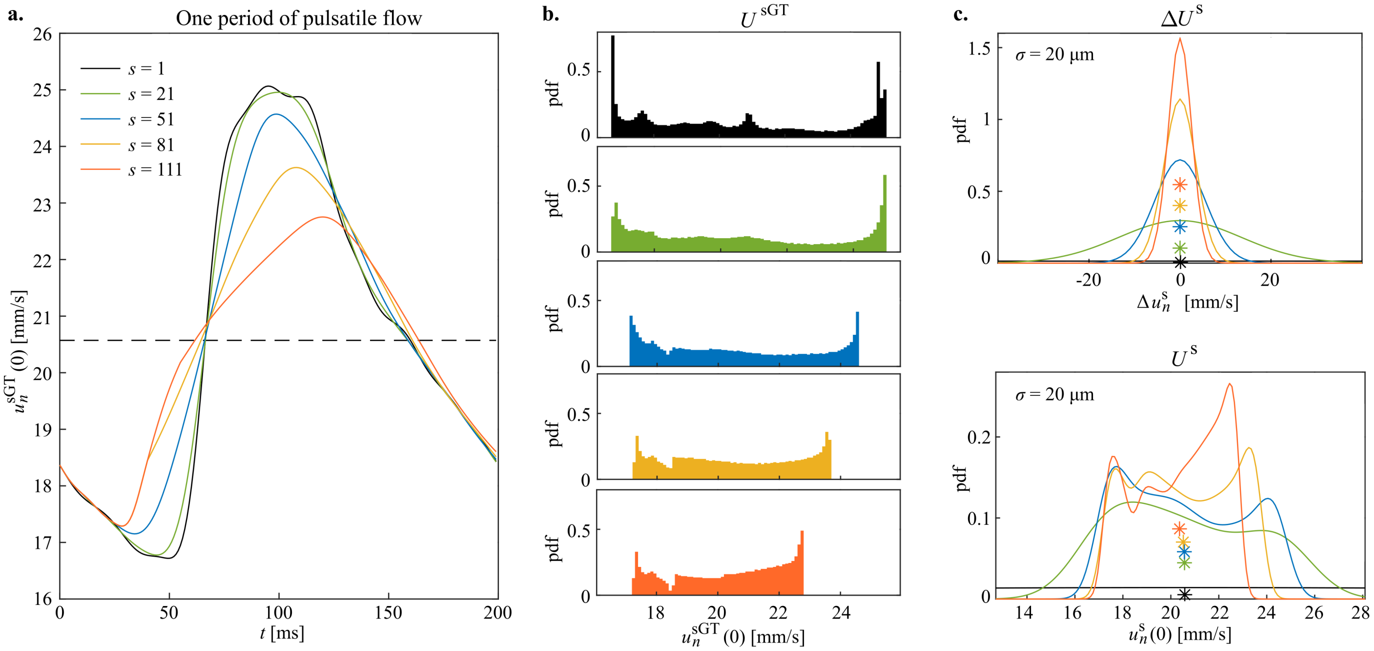

Fig. C.1. The span of the moving average filter has a large influence on the obtained distribution u^{f}. (a) The simulated ground truth pulsatile cycle ($s = 1$) is smoothed for different values of the span s. A full cycle (200 frames) is displayed here. (b) The histograms of U^{GTf} change shape for different value of s. (c) The velocity error distribution ΔU^{f} narrows for increased span. The scenario of $\sigma = 20$ μm is derived here. The width of ΔU^{f} for the non smoothed case (black) extends far outside of the interval given here. (d) The resulting velocity distribution U^{f} from the convolution of the results of (b) and (c). The two peaks are barely noticable for $s = 21$. Increasing the span to $s = 51$ improves the retrieval of the two peaks. The peaks move inwards with increasing s.

APPENDIX C

When increasing the span of the moving average filter, two effects cause the resulting velocity distribution U^{f} to change.

First, as introduced in section II-B2, by employing a moving average filter one implicitly assumes that $u_n^{\mathrm{GTf}}(r) \approx u_n^{\mathrm{GT}}(r)$. This assumption is violated when increasing the span s, as can be seen in Fig. C.1(a). Due to the flattening caused by the moving average filter, the smoothed pulsatile cycle does not resemble the original pulsatile cylce ($s = 1$) any longer. As a result, the shape of the histograms of U^{GTf} changes and their peaks move inwards.

Second, a more beneficial effect of increasing the span is the fact that ΔU^{f} narrows. After convolution with U^{GTf} this gives rise to narrower peaks in U^{f}. For lower localization precision a higher span is needed to be able to resolve two peaks. For example, in Fig. C.1(d) for a localization precision of $\sigma = 20$ μm, the two peaks are more distinct for $s = 51$ than $s = 21$.

APPENDIX D

The ULM simulator was additionally utilized to inspect the influence of the pulsatility fraction on the rendered ULM velocity map. The quality of the reconstruction was assessed by the RMSE of the average velocity prediction at each super resolved pixel compared to the ground truth average velocity (Fig. D.1(a)). Additionally, the ULM velocity reconstructions were inspected along the cross-section (Fig. D.2).

In Fig. D.1(a) the velocity RMSE and the fraction of tracked MBs is plotted against the localization precision for different values of P_f ranging from 0 to 1 and two maximum linking distance (MLD) setting. In tracking, the linking of two MBs is not permitted if the distance between them exceeds the MLD. Generally the RMSE is found to increase for increasing σ. The reported RMSE values become unreliable, as seen by the enlarged 95% confidence interval, when only a very low number of MBs is tracked. The fraction of MBs that is tracked drops for increasing values of σ, since the distance between two MBs becomes more likely to exceed the MLD.

The violins in the cross-sections of Fig. D.2 report the spread in $\bar{u}_n^{\mathrm{f}}(r)$ reported in the ULM velocity rendering at the corresponding lateral position in the vessel. The violins were constructed from 2000 cross-sections out of ULM velocity renderings of a 100 μm vessel for acquisition time of 10s.

Fig. D.1 and Fig. D.2 show that P_f can have a small effect on the ULM velocity reconstructions through two mechanisms. First, for an insufficient maximum linking distance the truncation of the velocity distributions of different P_f result in different values reported in the ULM reconstruction, see MLD $= 25$ μm of Fig. D.1(a) and Fig. D.1(b). We observe that the fraction of MBs tracked varies for different P_f. Fig. D.1(b) displays the non-smoothed velocity distributions U as found from $U^{\mathrm{GT}} \circledast \Delta U$ for $P_f = 0$, 0.2 and 0.4 and a fixed $\sigma = 5$ μm. For a MLD of 25 μm velocities over 25 mm/s can not be measured and the velocity distributions are truncated at that location. The truncation of these distributions by the insufficient setting of the MLD results in different locations of the new centroids, which represent the average velocity $\bar{u}_n^{\mathrm{f}}(r)$ as found in a ULM reconstruction, see the legend for the found values. Note that the non-smoothed velocity distribution is applicable here since the MLD is applied before the moving average filter. Due to the trunctation, the centerline velocity is found to be more underestimated for larger P_f. The theoretical explanation of Fig. D.1 corresponds to the simulation results

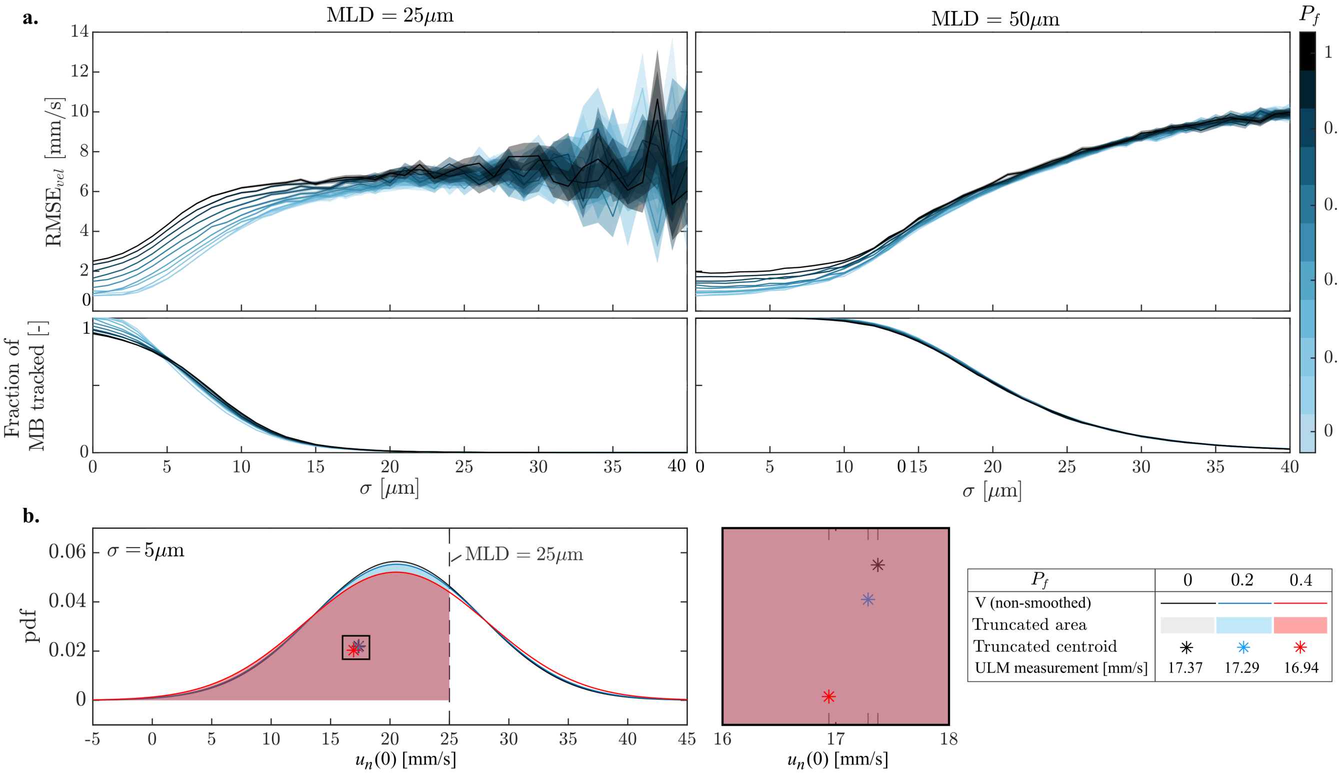

Fig. D.1. For specific scenarios the pulsatility fraction P_f can have an effect on the RMSE of the ULM velocity reconstruction. (a) Velocity RMSE and the fraction of tracked MBs is plotted against the localization precision σ for different simulated values of P_f. Left and right differ on the value of the maximum linking distance (ULM) used in ULM processing. A shaded area was added to indicate the 95% confidence interval as found from 1000 bootstrapped samples. (b) The non-smoothed velocity distribution U for three values of P_f and $\sigma = 5$ μm is shown. The MLD of 25 μm truncates the distributions at 25 mm/s causing the centroids of the distributions to shift to the left. The average velocity of the truncated distribution as measured in a ULM reconstruction is given in the legend for the different P_f.

of Fig. D.2, where the underestimation at the center of the vessel is clearly visible.

Additionally, the effect of insufficient MLD is visible in the average density reconstruction over the cross-section. For MLD = 25 μm the number of MBs tracked drops for the central pixels.

A second effect of P_f on the reported RMSE values is found in the high localization precision range ($\sigma < 10$ μm) even for sufficient MLD setting of 50 μm. This can not be caused by the truncation of the velocity distribution as described above since no loss in tracked number of MBs is found. When inspecting the cross-sections of Fig. D.1 we only observe a slight increase in violin size for larger P_f, which indicates a higher spread of reconstructed velocities in the ULM velocity rendering. We expect this effect to fade for longer acquisitions due to the averaging that is performed in rendering of the reconstruction. To construct these cross-sections, the single vessel configuration was simulated for only a 10s acquisition, while typical *in vivo* acquisition length is > 100s.

To prevent underestimation of the centerline velocities as found in Fig. D.2, the MLD should ideally be set such that it captures the full non smoothed velocity distribution. It should therefore be set significantly higher than the actual maximum blood flow velocity present. Based on our velocity distribution theory new systematic ways of setting the MLD can be formed replacing the trial and error tuning that is currently common.

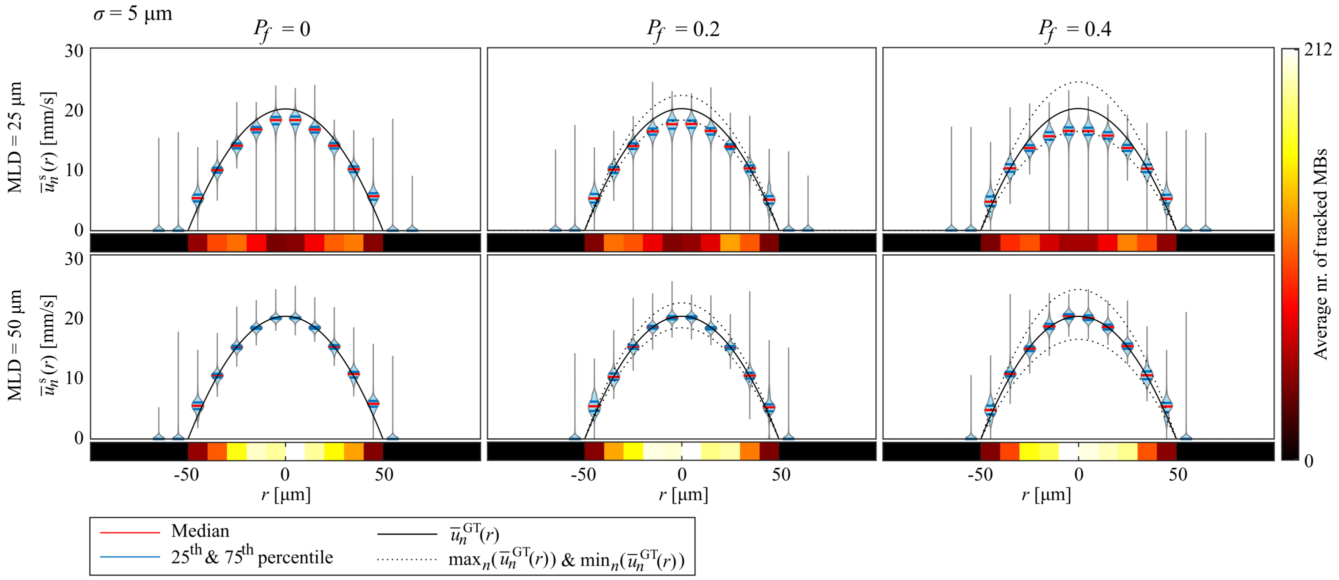

Fig. D.2. Violin plots displaying the spread in reconstructed velocities along a cross-section of a 100 μm vessel. A total of 2000 cross-sections of ULM velocity reconstructions were acquired to construct the violins. The colorbars below show the average number of MBs that passed that lateral location in the vessel. In all six cross-sections a localization precision of 5 μm was simulated. P_f varies along the columns and the two rows show the results for MLD = 25 μm and 50 μm. Median velocities obtained at the centerline for MLD= 25 μm and $P_f = 0$, 0.2 and 0.4 are respectively 18.69, 17.95 and 16.90 mm/s.

Chapter 4

Conclusion

This chapter concludes the thesis. Section 4-1 gives a summary of the main findings and contributions of the study. Section 4-2 provides additional points of discussion that were not included in the manuscript. In section 4-3 we provide an outlook on the retrieval of pulsatility in ultrasound localization microscopy.

4-1 Summary

Ultrasound imaging reveals internal tissue structures in a non-invasive way and is a common imaging modality in clinical practice [6]. It relies on the pulse-echo principle by illuminating the tissue with an acoustic wave and recording the backscattered echoes. Due to its use of ultrasound waves, the resolution of conventional ultrasound imaging is limited by the diffraction limit [24]. Increasing the transmit frequency improves resolution but limits the attainable imaging depth due to increased attenuation of the transmit pulse.

Ultrafast ultrasound localization microscopy (ULM) circumvents the trade-off between resolution and imaging depth as found in conventional ultrasound imaging. It relies on the localization and tracking of a large number of intravascular injected synthetic microbubbles (MB) over several hundreds of thousands of B-mode frames. The isolated MBs are localized with sub-wavelength precision enabling a 10-fold improvement in resolution compared to conventional diffraction limited ultrasound imaging [34]. By tracking of MBs, measurements of the velocity of blood flow are retrieved. Super resolved images of the microvasculature and its average blood flow can be recovered by accumulating the found MB tracks on a fine grid.

ULM requires a long acquisition time of typically hundreds of seconds to acquire sufficient data for reconstruction of the microvasculature [3]. Due to this long acquisition time, transient hemodynamic variations such as pulsatility get averaged out in the ULM velocity reconstruction.

Here two methods to retrieve pulsatility from MB tracks were introduced that leverage the high temporal sampling of MB tracks.

The first method relies on the filtering of single track velocity measurements to retrieve the pulsatile flow behaviour. The moving average filter was found incapable of filtering out newly uncovered grid-based artefacts. Inspection of the frequency spectrum of the velocity measurements validated that the artefacts were caused by MB localization that is dependent on the position within a beamformed pixel. The designed filtering technique consists of two steps. First a bandstop filter was applied to eliminate the grid based artefacts that were found for a specific range of frequencies. Second, a moving average filter was applied to further smooth the velocity measurements. From the filtered single track velocities, the extreme values were extracted and used to obtain a pulsatility fraction estimate. The method was validated in simulation where it was shown to retrieve the pulsatility fraction with an RMSE compared to the ground truth of 3.3%. Since it was found that a larger absolute deviation in flow velocity resulted in lower RMSE, we concluded that pulsatility could best be retrieved at the centerline of a vessel.

The second method reported in this study relies on the accumulation of velocity measurements at a fixed lateral location of the vessel over the full acquisition time. Theoretical derivation showed that a pulsatile flow led to bimodality in the velocity distribution, which could be retrieved for sufficient localization precision. The derivation of the velocity distribution was validated in simulation where the pulsatility fraction was recovered at an RMSE of 5.2%. Additionally, the effect of both the localization precision σ and the span of the moving average filter s on the retrieval of pulsatility were investigated. We found that increasing value of σ, i.e. lower localization precision, leads to larger underestimation of the pulsatility fraction. Based on our theory an optimal selection of s for specific flow scenarios and σ can be found.

To acquire the simulated data sets on which the methods were validated, a new ULM simulator was developed that incorporates pulsatility. The pulsatile flow was simulated by modelling its temporal and spatial characteristics separately and relying on *in vivo* observations [5]. The simulator consists of two simulation scenarios. The first scenario incorporated all steps of a typical ULM acquisition including simulation of B-mode frames and localization of the MBs in these frames. In the second scenario, a spatial offset imitating the localization error was directly added to the simulated MB positions, such that no localization was needed. This approach allowed to control the localization precision.

All together our results show that the recovered track velocity measurements in ULM contain more information on hemodynamics of the blood flow than is represented by conventional ULM image reconstructions. In future research, the reported methods need to be validated *in vivo* and their application for the retrieval of other hemodynamic phenomena could be investigated.

4-2 Discussion

The manuscript of Section 3 included a main discussion of the reported results of this study. It focused on two topics. First, the proposed methods in this study rely on high acquisition frame rates. The effect of the frame rate on the performance of the proposed methods should be investigated by future research. Second, the need for *in vivo* validation of the introduced methods was highlighted. The remainder of this section addresses additional points of discussion, not previously discussed in the manuscript.

Pulsatile flow was simulated by assuming a rigid vessel of constant diameter and modelling the spatial and temporal characteristics separately. Spatially, the flow was assumed independent on the axial vessel coordinate and described by a parabolic profile along the lateral vessel coordinate corresponding to Poisseuille flow [68]. Temporal characteristics were retrieved from *in vivo* observations [5]. An alternative method for simulating pulsatility in rigid pipes is provided by the Womersley solution [69]. It models the flow response to a varying pressure gradient incorporating the lag a flow can experience due to inertial forces. However, the flow in the microvasculature was found to be in phase with the local pressure gradient and can therefore be modelled by deriving the Poisseuille flow for each time instance [71]. This result supports the separation of spatial and temporal flow characteristics as applied in the simulator. Additional information on the rigid vessel assumption, Poisseuille flow and the Womersley solution is included in Appendix A. The rigid vessel assumption does not hold for all vessels in the vasculature. Due to their muscular vessel wall, arterioles can dilate and constrict and therefore regulate the blood flow to the capillaries [72]. This effect was not considered in this study.

Additionally, the likeliness of the simulated data to *in vivo* acquisitions could be improved by measures including: a more realistic vascular architecture based on *in vivo* observations, varying the number of simulated MBs and including tissue structures in the simulation of B-mode images.

Throughout the study, localization error was assumed to be distributed as $\mathcal{N}(0, \sigma^2)$. However, this assumption does not generally hold for all localization algorithms as shown by [1]. Future research could extent the derivation of the velocity distribution for other localization error distributions. Additionally, the presence of the grid-based artefact shows the localization error in our results to be dependent on the MB position within the beamformed pixel for both the radial symmetry and the Gaussian fitting algorithm. Future research could investigate for each localization algorithm what the cause is of this grid-dependent localization. To assess whether the localization precision achieved by our simulator is within an appropriate range, we relied on [1], which reported MB localization RMSE from simulated data at different SNR. The conversion needed to map their reported values from RMSE to localization precison σ is given in Appendix B.

The steps involved in rendering a ULM image from acquired MB tracks are not well described in literature. In this study these steps were described explicitly and their influence on the acquired velocity measurements was shown. Especially the moving average filter step was shown to be of significance: an appropriate setting of the moving average span s was shown to improve retrieval of pulsatility.

4-3 Outlook

The two reported methods were designed to retrieve the pulsatility in a target vessel from track velocity measurements obtained in that vessel. Another angle to approach the task of retrieving hemodynamics would be to aim for drastically reducing the acquisition time of a full ULM reconstruction, i.e. achieving time-resolved ULM. In this scenario a ULM movie would be constructed from which pulsatility could be retrieved.

Sparsity of velocity measurements in a ULM acquisition is expected to be the main challenge for achieving time-resolved ULM in the future. We hypothesize that to be able to attain acquisition times suitable for retrieving hemodynamics, it is insufficient to solely rely on increasing the density of the MB population. Even for acquisitions of increased MB density the challenge remains to infer a full velocity map from sparse velocity measurements found at changing locations.

In the early stages of this project efforts were made to achieve time-resolved ULM by application of a Kalman filter. The idea consisted in capturing the spatiotemporal dynamics of the blood flow by a state-space model derived from the Navier Stokes equations. Based on this model, state estimation of the flow in each pixel could recursively be performed by the Kalman filter for each new set of acquired velocity measurements. Wang *et al.* demonstrated this method for the reconstruction of wall-bounded turbulence [73].

The derivation of a state-space model for a simple straight vessel from the Navier Stokes equations consisted of three steps: simplifications corresponding to flow in a straight rigid vessel, linearization around an assumed average flow profile and discretization. Several reasons resulted in the decision to abort this approach and switch to what later became the methods reported here. First, the derived state-space model was shown to violate the incompressibility condition, since the flow into the vessel did not equal the flow out of the vessel. Second, the method was not expected to generalize well to more complex networks of vessels. Lastly, a large computational demand was expected when applying this method to full ULM images, since the state matrix was found to be of size $(2N \times 2N)$. Where N corresponds to the number of pixels in the super resolved ULM velocity map. We advice future research that aims to apply the Kalman filter to attain time-resolved ULM to resort to a different method to acquire the state-space model.

In contrast to the model-based Kalman filtering approach, Chen *et al.* proposed a learning based method to achieve time-resolved ULM [40]. Their method consisted of training a neural network to map a low number of input B-mode frames to an output velocity reconstruction. The structure of their neural network resembles the U-Net architecture [74]. They report a 16 ms temporal resolution allowing to retrieve pulsatility in an *in vivo* chicken embryo aquisition. This indicate that applying deep learning for pulsatility retrieval is a relevant future research topic. Several opportunities for improvement were identified in their results. First, incorporating a prior velocity map into their network could help resolve the unrealistic flow artefacts and the distortion of the vascular architecture as observed in their reported results. Second, training their network on simulated data that incorporates a pulsatile flow is expected to further improve the retrieval of pulsatility by their proposed method. Additionally, a pulsatile ULM simulator can be used to generate test data that allows the output of the neural network to be compared to a ground truth. The ULM simulator designed in this study could be useful in future research aiming to apply a learning based method to recover pulsatility.

Appendix A

The womersley solution for pulsatile flow in rigid pipes

Before deriving the equations for pulsatile flow, the simpler case of Poiseuille flow is discussed. An incompressible Newtonian fluid and rigid pipes of circular cross-section are assumed in the following sections.

Poisseuille flow

Poiseuille flow denotes a steady state fully developed flow in rigid tubes, which is assumed to be symmetrical about the l axis (no external forces cause the flow to rotate). A fully developed flow is found in pipes after a sufficient distance from the inlet. In this region entry effects are negligible and the flow satisfies $\frac{\partial u}{\partial l} = 0$, see Figure A-1 for the definition of the variables utilized here. For a fully developed flow symmetrical about the l axis, the Navier Stokes equations reduce to [68]

$$\rho \frac{\partial u}{\partial t} + \frac{\partial p}{\partial l} = \mu \left(\frac{\partial^2 u}{\partial r^2} + \frac{1}{r} \frac{\partial u}{\partial r} \right) \tag{A-1}$$

where p is the pressure[Pa], ρ is the fluid's density [kg/m^3] and μ the fluid's viscosity [Pa$\cdot$s]. In a fully developed axisymmetrical flow, the velocity u depends only on r and t and the pressure p on l and t, i.e.

$$u = u(r,t), \qquad p = p(l,t) \tag{A-2}$$

Poiseuille flow is given by the steady state solution $u = u_{ss}(r)$, which has $\frac{\partial u_{ss}}{\partial t} = 0$. This corresponds to a situation in which the pressure gradient that drives the flow is time-independent.

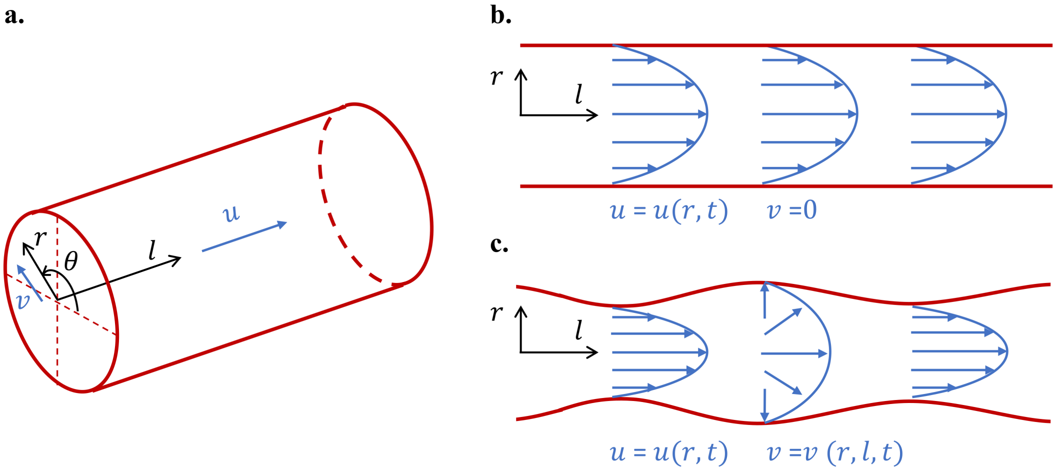

Figure A-1: Illustration of the difference between pulsatile flow in rigid and elastic vessels. (a) Cylindrical coordinates in a blood vessel with the flow velocities u and v in the axial and lateral direction respectively. (b) Fully developed axisymmetrical flow in a rigid vessel. The velocity profile is constant along l, even for time varying pressure gradient. (c) In a vessel with elastic walls, the velocity profiles vary along the vessel for changing pressure gradient in time.

Therefore, $p = p_{ss}(l)$ with $\frac{\partial p_{ss}}{\partial x} = k_{ss}$, where k_{ss} is a constant [Pa/m]. To find the steady state solution $u_{ss}(r)$, (A-1) reduces to

$$\frac{\partial p_{ss}}{\partial l} = \mu \left(\frac{\partial^2 u_{ss}}{\partial r^2} + \frac{1}{r} \frac{\partial u_{ss}}{\partial r} \right) \tag{A-3}$$

when applying the no-slip boundary conditions, the Poiseuille flow u_{ss} is found as

$$u_{ss} = \frac{k_{ss}}{4\mu} \left(r^2 - R^2 \right) \tag{A-4}$$

where R is the radius of the tube [m]. Note that only in rigid tubes it is possible to have a constant flow u while the pressure p varies along the tube. When a tube wall is non-rigid, it expands when encountering a local pressure change, resulting in a change in flow velocity, see Figure A-1(b) and A-1(c).

Pulsatile flow

Due to the beating of the heart, the pressure gradient along a vessel varies in time and the flow in this vessel is pulsatile. This applies mainly to arteries but pulsatility was also found in veins [5]. For slow changes in pressure gradient, the resulting flow velocity will almost be in phase with the changing pressure gradient and we can use the Poiseuille equation to approximate the flow at each instance [68]. However, as the frequency of the pressure oscillation increases, the fluid's inertia causes the flow to lag behind. Due to this lag, the flow is unable to build up to the peak value that it would have reached at the same peak pressure in steady state. Both the lag and the loss in peak flow increase for increasing frequency of pulsation [68]. For pulsatile flow of sufficient frequency the steady state solution described in Section A can not be applied. Another method is needed to solve

$$\rho\frac{\partial u}{\partial t}+\frac{\partial p}{\partial l}=\mu\left(\frac{\partial^2 u}{\partial r^2}+\frac{1}{r}\frac{\partial u}{\partial r}\right) \tag{A-1 revisited}$$

Rigid or elastic tube In order for pulsatile flow in rigid tubes to satisfy the incompressibility conditions, it has to respond in unison to a change in pressure gradient $\frac{\partial p}{\partial l}$ [68]. Since the tube is unable to stretch to a larger diameter and the fluid density is constant, an increased inflow comes hand in hand with an instantaneously increased outflow. A change in pressure gradient is thus assumed to act instantaneously over the full length of the tube, resulting in a constant velocity profile along the axial direction, see Figure A-1(b).

In nonrigid tubes, an increase in pressure causes the tube to stretch locally. Due to its elasticity, the tube then recoils back to its original diameter. The pressure difference travels in a wave motion further down the tube by inducing local stretching and recoiling. The velocity profile in a nonrigid tube changes along the axial direction according to the pressure wave passing, see Figure A-1(c). In the remainder of this text, rigid tubes will be assumed.

Oscillatory flow solution The linearity of (A-1) in both $u(r,t)$ and $p(l,t)$ allows to calculate the steady state and oscillatory part of the flow separately. The velocity, pressure and pressure gradient $k(t)$ are separated in their steady state (ss) and oscillatory (ϕ) parts as

$$\begin{aligned} p(l,t) &= p_{ss}(l)+p_\phi(l,t)\\ u(r,t) &= u_{ss}(r)+u_\phi(r,t)\\ k(t) &= \frac{\partial p}{\partial l}=k_{ss}+k_\phi(t) \end{aligned} \tag{A-5}$$

Substitution in (A-1) results in

$$\begin{aligned} &\left\{\frac{dp_{ss}}{dl}-\mu\left(\frac{d^2u_{ss}}{dr^2}+\frac{1}{r}\frac{du_{ss}}{dr}\right)\right\}\\ +&\left\{\rho\frac{\partial u_\phi}{\partial t}+\frac{\partial p_\phi}{\partial l}-\mu\left(\frac{\partial^2 u_\phi}{\partial r^2}+\frac{1}{r}\frac{\partial u_\phi}{\partial r}\right)\right\}=0 \end{aligned} \tag{A-6}$$

where the first group of terms does not depend on time, while the second group of terms do. Both groups should equal zero for (A-6) to hold. The solution to the steady state part is given by (A-4). The remainder of this section will focus on retrieving the oscillatory flow solution. Rewriting the second term of (A-6) and substituting $\frac{\partial p_\phi}{\partial l}=k_\phi(t)$ results in

$$\mu\left(\frac{\partial^2 u_\phi}{\partial r^2}+\frac{1}{r}\frac{\partial u_\phi}{\partial r}\right)-\rho\frac{\partial u_\phi}{\partial t}=k_\phi(t) \tag{A-7}$$

where we aim to retrieve $u\phi$ from a known pulsatile pressure gradient $k_\phi(t)$. Any periodic $k_\phi(t)$ of arbitrary shape can be represented by a Fourier series as

$$k_\phi(t)=\sum_{n=0}^{\infty}A_n\cos\left(\frac{2n\pi t}{T}\right)+\sum_{n=1}^{\infty}B_n\sin\left(\frac{2n\pi t}{T}\right) \tag{A-8}$$

where T is the period and the Fourier coefficients can be found by

$$\begin{aligned} A_0 &= \frac{1}{T}\int_T k_\phi(t)dt \\ A_n &= \frac{2}{T}\int_T k_\phi(t)\cos\left(\frac{2n\pi t}{T}\right)dt \\ B_n &= \frac{2}{T}\int_T k_\phi(t)\sin\left(\frac{2n\pi t}{T}\right)dt \end{aligned} \tag{A-9}$$

Linearity of (A-7) in u_ϕ allows the evaluations of each Fourier series component individually. Note that an approximation can be obtained by incorporating only the first few Fourier terms in the solution. For simplicity in further derivations, the exponential form of the Fourier series is adapted. It is given as

$$k_\phi(t) = \sum_{n=-\infty}^{\infty} c_n e^{i\omega_n t} \tag{A-10}$$

where $\omega_n = \frac{2n\pi}{T}$ and

$$c_n =\triangleq \begin{cases} a_0/2, & n = 0 \\ \frac{a_n}{2}e^{-i\varphi_n} = \frac{1}{2}\left(a_n - ib_n\right), & n > 0 \\ c^*_{|n|}, & n < 0 \end{cases} \tag{A-11}$$

Substituting one of the Fourier terms of k_ϕ in (A-7) results in

$$\frac{\partial^2 u_\phi}{\partial r^2} + \frac{1}{r}\frac{\partial u_\phi}{\partial r} - \frac{\rho}{\mu}\frac{\partial u_\phi}{\partial t} = \frac{c_n}{\mu}e^{i\omega_n t} \tag{A-12}$$

This equation has to be solved for each Fourier term of $k_\phi(t)$. A solution can be found by separation of variables. $u_\phi(r,t)$ is decomposed as

$$u_\phi(r,t) = U_\phi(r)e^{i\omega_n t} \tag{A-13}$$

Substitution results in

$$\begin{gathered} \frac{d^2 U_\phi}{dr^2} + \frac{1}{r}\frac{dU_\phi}{dr} - \frac{i\Omega^2}{R^2}U_\phi = \frac{k_{ss}}{\mu} \\ \text{where} \qquad \Omega = \sqrt{\frac{\rho\omega_n}{\mu}}R \end{gathered} \tag{A-14}$$

where Ω is the nondimensional Womersley number [69] that describes the relation between pulsatile flow frequency and viscous forces in a fluid. Its value dominates the pulsatile behaviour of the flow. R is the radius of the vessel. Since (A-14) can be recognized as a form of Bessel equation, a standard solution can be found. When applied the no-slip boundary conditions, this standard solution results in

$$U_\phi = \frac{ic_n R^2}{\mu\Omega^2}\left(1 - \frac{J_0(\zeta)}{J_0(\Lambda)}\right) \tag{A-15}$$

where J_0 is the zero order Bessel function of the first kind and

$$\zeta = \Lambda\frac{r}{R}, \qquad \Lambda = \left(\frac{i-1}{\sqrt{2}}\right)\Omega \tag{A-16}$$

See [68] for a step by step derivation of the solution given in (A-15). Consider again our goal to find the flow velocity $u(r,t)$ if we have the periodic pressure gradient given by [69]

$$k(t) = k_{ss} + \mathcal{R}e\left\{\sum_{n=-N}^{N} c_n e^{i\omega_n t}\right\} \tag{A-17}$$

The solution consist of the steady state solution plus the summation of (A-15) for each Fourier term up to N. We find

$$\begin{aligned} u(r,t) &= u_{ss}(r) + u_{\phi}(r,t) \\ &= \frac{k_{ss}}{4\mu}\left(r^2 - R^2\right) + \mathcal{R}e\left\{\frac{ic_n R^2}{\mu\Omega^2}\left(1 - \frac{J_0(\zeta)}{J_0(\Lambda)}\right)\right\} \end{aligned} \tag{A-18}$$

Appendix B

Conversion between RMSE and σ

To determine the relevant range of localization precision σ for our designed simulator, we rely on the RMSE values reported in [1], in which the localization precision attainable with different localization algorithms at varying SNR of the US frames was investigated. The conversion between the reported RMSE values and their corresponding σ values was found as

$$\mathrm{RMSE}((\hat{x},\hat{z})) = \sqrt{2}\sigma \tag{B-1}$$

where $(\hat{x},\hat{z})$ are the MB location estimates and the localization precision σ is given by the standard deviation of the localization error distribution. The RMSE is defined by

$$\begin{aligned} \mathrm{RMSE}((\hat{x},\hat{z})) &= \sqrt{\mathrm{MSE}(\hat{x},\hat{z})} \\ &= \sqrt{\frac{1}{N}\sum_{i}^{N}(\hat{x}_i - x_i)^2 + (\hat{z}_i - z_i)^2} \end{aligned} \tag{B-2}$$

were $(\hat{x}_\mathrm{i},\hat{z}_\mathrm{i})$ is the estimated location of MB i and $(x_\mathrm{i},z_\mathrm{i})$ its ground truth location. First, the relation between the mean squared error MSE and σ is found by

$$\begin{aligned} \mathrm{MSE}((\hat{x},\hat{z})) &= \frac{1}{N}\sum_{i}^{N}(\hat{x}_i - x_i)^2 + (\hat{z}_i - z_i)^2 \\ &= \mathrm{E}\left[(\hat{x}-x)^2 + (\hat{z}-z)^2\right] \\ &= \mathrm{E}\left[(\hat{x}-x)^2\right] + \mathrm{E}\left[(\hat{z}-z)^2\right] \\ &= \mathrm{Var}(\hat{x}) + \mathrm{Bias}(\hat{x})^2 + \mathrm{Var}(\hat{z}) + \mathrm{Bias}(\hat{z})^2 \\ &= 2\sigma^2 \end{aligned} \tag{B-3}$$

where localization error $(\hat{x}_i - x_i)$ and $(\hat{z}_i - z_i)$ were assumed to be independent and identically distributed (IID) as $\sim \mathcal{N}(0,\sigma^2)$.

Finally, taking the square root of (B-3), we find (B-1). The minimum and maximum RMSE values of 0.13λ and 0.32λ for respective SNR of 60 and 10 found in [1] correspond to a localization precision σ of $0.09\lambda = 7.9$ μm and $0.23\lambda = 19.5$ μm respectively.

Bibliography

[1] B. Heiles, A. Chavignon, V. Hingot, P. Lopez, E. Teston, and O. Couture, "Performance benchmarking of microbubble-localization algorithms for ultrasound localization microscopy," *Nature Biomedical Engineering*, 2022.

[2] B. B. Goldberg and B. A. Kimmelman, *Medical diagnostic ultrasound: A retrospective on its 40th anniversary.* New York: Eastman Kodak Company, 1988.

[3] O. Couture, V. Hingot, B. Heiles, P. Muleki-Seya, and M. Tanter, "Ultrasound localization microscopy and super-resolution: A state of the art," *IEEE Transactions on Ultrasonics, Ferroelectrics, and Frequency Control*, vol. 65, no. 8, pp. 1304–1320, 2018.

[4] O. Couture and V. Hingot, "Course on super resolution," 2020.

[5] T. P. Santisakultarm, N. R. Cornelius, N. Nishimura, A. I. Schafer, R. T. Silver, P. C. Doerschuk, W. L. Olbricht, and C. B. Schaffer, "In vivo two-photon excited fluorescence microscopy reveals cardiac- and respiration-dependent pulsatile blood flow in cortical blood vessels in mice," *American Journal of Physiology-Heart and Circulatory Physiology*, vol. 302, no. 7, pp. H1367–H1377, 2012.

[6] T. L. Szabo, *Diagnostic ultrasound imaging: inside out.* Elsevier Academic Press, 2 ed., 2014.

[7] J. M. Sanches, A. F. Laine, and J. S. Suri, *Ultrasound Imaging: Advances and Applications.* Springer, 2011.

[8] A. Carovac, F. Smajlovic, and D. Junuzovic, "Application of ultrasound in medicine," *Acta informatica medica : AIM : journal of the Society for Medical Informatics of Bosnia & Herzegovina : casopis Drustva za medicinsku informatiku BiH*, vol. 19, no. 3, 2011.

[9] P. Laugier and G. Haïat, *Bone Quantitative Ultrasound.* Springer, Dordrecht, 2011.

[10] J. Bercoff, M. Tanter, and M. Fink, "Supersonic shear imaging: a new technique for soft tissue elasticity mapping," *IEEE Transactions on Ultrasonics, Ferroelectrics, and Frequency Control*, vol. 51, no. 4, pp. 396–409, 2004.

[11] C. P. Loizou, M. Pantzaris, and C. S. Pattichis, *Media and Intima Thickness and Texture Analysis of the Common Carotid Artery*, pp. 99–128. Boston, MA: Springer US, 2012.

[12] C. Errico, J. Pierre, S. Pezet, Y. Desailly, Z. Lenkei, O. Couture, and M. Tanter, "Ultrafast ultrasound localization microscopy for deep super-resolution vascular imaging," *Nature*, vol. 527, pp. 499–504, 2015.

[13] W. Allison, *Fundamental Physics for Probing and Imaging.* Oxford University Press, Incorporated, 2006.

[14] N. de Jong, F. T. Cate, C. Lancée, J. Roulandt, and N. Bom, "Principles and recent developments in ultrasound constrast agents," *Ultrasonics*, vol. 29, no. 4, pp. 324–330, 1991.

[15] J. W. Goodman, *Speckle Phenomena in Optics: Theory and Applications.* Roberts & Co, 2007.

[16] T. J. Klein, *Statistical Image Processing of Medical Ultrasound Radio Frequency Data.* PhD thesis, Technische Universität München, 2012.

[17] U. Soergel, *Review of Radar Remote Sensing on Urban Areas*, p. 117. Dordrecht: Springer Netherlands, 2010.

[18] P. M. Shankar, "A general statistical model for ultrasonic backscattering from tissues," *IEEE transactions on ultrasonics, ferroelectrics, and frequency control*, vol. 47, no. 3, pp. 727–736, 2000.

[19] V. Perrot, M. Polichetti, F. Varray, and D. Garcia, "So you think you can das? a viewpoint on delay-and-sum beamforming," *Université de Lyon*, 2020.

[20] J. Kirkhorn, "Introduction to iq-demodulation of rf-data," , Norwegian University of Science and Technology, Trondheim, Norway, 1999. [Online; last accessed 29-April-2021].

[21] G. Montaldo, M. Tanter, J. Bercoff, N. Benech, and M. Fink, "Coherent plane-wave compounding for very high frame rate ultrasonography and transient elastography," *IEEE Transactions on Ultrasonics, Ferroelectrics, and Frequency Control*, vol. 56, no. 3, pp. 489–506, 2009.

[22] C. Chen, H. H. G. Hansen, G. A. G. M. Hendriks, J. Menssen, J.-Y. Lu, and C. L. de Korte, "Point spread function formation in plane-wave imaging: A theoretical approximation in fourier migration," *IEEE Transactions on Ultrasonics, Ferroelectrics, and Frequency Control*, vol. 67, no. 2, pp. 296–307, 2020.

[23] A. Bar-Zion, O. Solomon, C. Tremblay-Darveau, D. Adam, and Y. C. Eldar, "Sushi: Sparsity-based ultrasound super-resolution hemodynamic imaging," *IEEE Transactions on Ultrasonics, Ferroelectrics, and Frequency Control*, vol. 65, no. 12, pp. 2365–2380, 2018.

[24] R. Cobbold, *Foundations of biomedical ultrasound.* Oxford University Press, New York, 2007.

[25] E. Macé, G. Montaldo, I. Cohen, M. Baulac, M. Fink, and M. Tanter, "Functional ultrasound imaging of the brain," *Nature Methods*, vol. 8, no. 8, pp. 662–666, 2011.

[26] K. Christensen-Jeffries, R. J. Browning, M.-X. Tang, C. Dunsby, and R. J. Eckersley, "In vivo acoustic super-resolution and super-resolved velocity mapping using microbubbles," *IEEE Transactions on Medical Imaging*, vol. 34, no. 2, pp. 433–440, 2015.

[27] M. Lelek, M. T. Gyparaki, G. Beliu, F. Schueder, J. Griffié, S. Manley, R. Jungmann, M. Sauer, M. Lakadamyali, and C. Zimmer, "Single-molecule localization microscopy," *Nature Reviews Methods Primers*, vol. 1, no. 1, 2021.

[28] I. M. Khater, I. R. Nabi, and G. Hamarneh, "A review of super-resolution single-molecule localization microscopy cluster analysis and quantification methods," *Patterns*, vol. 1, no. 3, p. 100038, 2020.

[29] R. S. O. W. L. S. O. J. S. B. M. W. D. J. L.-S. H. F. H. Eric Betzig, George H. Patterson, "Imaging intracellular fluorescent proteins at nanometer resolution," *Science*, vol. 313, no. 5793, pp. 1642–1645, 2006.

[30] W. E. Moerner and L. Kador, "Optical detection and spectroscopy of single molecules in a solid," *Phys. Rev. Lett.*, vol. 62, pp. 2535–2538, May 1989.

[31] O. Couture, M. Tanter, and M. Fink, "Method and device for ultrasound imaging," 2010.

[32] P. Song, A. Manduca, J. D. Trzasko, R. E. Daigle, and S. Chen, "On the effects of spatial sampling quantization in super-resolution ultrasound microvessel imaging," *IEEE Transactions on Ultrasonics, Ferrroelectrics and Frequency control*, vol. 65, no. 12, pp. 2264–2276, 2018.

[33] C. Huang, M. R. Lowerison, J. D. Trzasko, A. Manduca, Y. Bresler, S. Tang, P. Gong, U.-W. Lok, P. Song, and S. Chen, "Short acquisition time super-resolution ultrasound microvessel imaging via microbubble separation," *Scientific Reports*, vol. 10, no. 1, 2020.

[34] K. Christensen-Jeffries, O. Couture, P. A. Dayton, Y. C. Eldar, K. Hynynen, F. Kiessling, M. O'Reilly, G. F. Pinton, G. Schmitz, M.-X. Tang, M. Tanter, and R. J. van Sloun, "Super-resolution ultrasound imaging," *Ultrasound in Med. & Biol.*, vol. 46, no. 4, pp. 865–891, 2020.

[35] B. Schrope, V. Newhouse, and V. Uhlendorf, "Simulated capillary blood flow measurement using a nonlinear ultrasonic contrast agent," *Ultrasonic Imaging*, vol. 14, no. 2, pp. 134–158, 1992.

[36] L. Milecki, J. Porée, H. Belgharbi, C. Bourquin, R. Damseh, P. Delafontaine-Martel, F. Lesage, M. Gasse, and J. Provost, "A deep learning framework for spatiotemporal ultrasound localization microscopy," *IEEE Transactions on Medical Imaging*, vol. 40, no. 5, pp. 1428–1437, 2021.

[37] R. J. G. van Sloun, O. Solomon, M. Bruce, Z. Z. Khaing, H. Wijkstra, Y. C. Eldar, and M. Mischi, "Super-resolution ultrasound localization microscopy through deep learning," *IEEE Transactions on Medical Imaging*, vol. 40, no. 3, pp. 829–839, 2021.

[38] V. Hingot, C. Errico, B. Heiles, L. Rahal, M. Tanter, and O. Couture, "Microvascular flow dictates the compromise between spatial resolution and acquisition time in ultrasound localization microscopy," *Scientific Reports*, vol. 9, p. 2456, 2019.

[39] C. Iadecola, "The neurovascular unit coming of age: A journey through neurovascular coupling in health and disease," *Neuron*, vol. 96, no. 1, pp. 17–42, 2017.

[40] X. Chen, M. R. Lowerison, Z. Dong, N. C. Sekaran, C. Huang, S. Chen, T. M. Fan, D. A. Llano, and P. Song, "Localization free super-resolution microbubble velocimetry using a long short-term memory neural network," *bioRxiv*, 2021.

[41] C. Demené, T. Deffieux, M. Pernot, B.-F. Osmanski, V. Biran, J.-L. Gennisson, L.-A. Sieu, A. Bergel, S. Franqui, J.-M. Correas, I. Cohen, O. Baud, and M. Tanter, "Spatiotemporal clutter filtering of ultrafast ultrasound data highly increases doppler and fultrasound sensitivity," *IEEE Transactions on Medical Imaging*, vol. 34, no. 11, pp. 2271–2285, 2015.

[42] Y. Desailly, A.-M. Tissier, J.-M. Correas, F. Wintzenrieth, M. Tanter, and O. Couture, "Contrast enhanced ultrasound by real-time spatiotemporal filtering of ultrafast images," *Physics in Medicine & Biology*, vol. 62, pp. 31–42, 2017.

[43] D. Simpson, C. T. Chin, and P. Burns, "Pulse inversion doppler: a new method for detecting nonlinear echoes from microbubble contrast agents," *IEEE Transactions on Ultrasonics, Ferroelectrics, and Frequency Control*, vol. 46, no. 2, pp. 372–382, 1999.

[44] O. M. Viessmann, R. J. Eckersley, K. Christensen-Jeffries, M. X. Tang, and C. Dunsby, "Acoustic super-resolution with ultrasound and microbubbles," *Physics in Medicine and Biology*, vol. 58, pp. 6447–6458, p 2013.

[45] R. Parthasarathy, "Rapid, accurate particle tracking by calculation of radial symmetry centers," *Nature Methods*, vol. 9, no. 7, pp. 724–728, 2012.

[46] D. Ackermann and G. Schmitz, "Detection and tracking of multiple microbubbles in ultrasound b-mode images," *IEEE Transactions on Ultrasonics, Ferroelectrics and Frequency Control*, vol. 63, pp. 72–82, jan 2016.

[47] T. Opacic, S. Dencks, B. Theek, M. Piepenbrock, D. Ackermann, A. Rix, T. Lammers, E. Stickeler, S. Delorme, G. Schmitz, and F. Kiessling, "Motion model ultrasound localization microscopy for preclinical and clinical multiparametric tumor characterization," *Nature Communications*, vol. 9, no. 1, p. 1527, 2018.

[48] O. Solomon, R. J. G. van Sloun, H. Wijkstra, M. Mischi, and Y. C. Eldar, "Exploiting flow dynamics for superresolution in contrast-enhanced ultrasound," *IEEE Transactions on Ultrasonics, Ferroelectrics, and Frequency Control*, vol. 66, no. 10, 2019.

[49] S. Tang, P. Song, J. D. Trzasko, M. Lowerison, C. Huang, P. Gong, U.-W. Lok, A. Manduca, and S. Chen, "Kalman filter-based microbubble tracking for robust super-resolution ultrasound microvessel imaging," *IEEE Transactions on Ultrasonics, Ferroelectrics, and Frequency Control*, vol. 67, no. 9, pp. 1738–1751, 2020.

[50] J. Foiret, H. Zhang, T. Ilovitsh, L. Mahakian, S. Tam, and K. W. Ferrara, “Ultrasound localization microscopy to image and assess microvasculature in a rat kidney,” *Scientific Reports*, vol. 7, p. 13662, 2017.

[51] K. Jaqaman, D. Loerke, M. Mettlen, H. Kuwata, S. Grinstein, S. L. Schmid, and G. Danuser, “Robust single-particle tracking in live-cell time-lapse sequences,” *Nature methods*, vol. 5, no. 8, 2008.

[52] P. Song, J. D. Trzasko, A. Manduca, R. Huang, R. Kadirvel, D. F. Kallmes, and S. Chen, “Improved super-resolution ultrasound microvessel imaging with spatiotemporal nonlocal means filtering and bipartite graph-based microbubble tracking,” *IEEE Transactions on Ultrasonics, Ferroelectrics, and Frequency Control*, vol. 65, no. 2, pp. 149–167, 2018.

[53] B. Heiles, M. Correira, V. Hingot, M. Pernot, J. Provost, M. Tanter, and O. Couture, “Ultrafast 3d ultrasound localization microscopy using a 32 × 32 matrix array,” *IEEE Transactions on Medical Imaging*, vol. 38, no. 9, pp. 2005–2015, 2019.

[54] H. W. Kuhn, “The hungarian method for the assignment problem,” *Naval Research Logistics Quarterly*, vol. 2, no. 1-2, pp. 83–97, 1955.

[55] W. Walker and G. Trahey, “A fundamental limit on delay estimation using partially correlated speckle signals,” *IEEE Transactions on Ultrasonics, Ferroelectrics, and Frequency Control*, vol. 42, no. 2, pp. 301–308, 1995.

[56] V. Hingot, C. Errico, M. Tanter, and O. Couture, “Subwavelength motion-correction for ultrafast ultrasound localization microscopy,” *Ultrasonics*, vol. 77, pp. 17–21, 2017.

[57] H. Foroosh, J. Zerubia, and M. Berthod, “Extension of phase correlation to subpixel registration,” *IEEE Transactions on Image Processing*, vol. 11, no. 3, pp. 188–200, 2002.

[58] S. Uchida, “Image processing and recognition for biological images,” *Development, Growth & Differentiation*, vol. 55, pp. 523–549, 2013.

[59] O. Couture, B. Besson, G. Montaldo, M. Fink, and M. Tanter, “Microbubble ultrasound super-localization imaging (musli),” in *2011 IEEE International Ultrasonics Symposium*, pp. 1285–1287, 2011.

[60] Y. Desailly, O. Couture, M. Fink, and M. Tanter, “Sono-activated ultrasound localization microscopy,” *Applied Physics Letters*, vol. 103, no. 17, p. 174107, 2013.

[61] M. A. OReilly and K. Hynynen, “A super-resolution ultrasound method for brain vascular mapping,” *Medical Physics*, vol. 40, no. 11, p. 110701, 2013.

[62] F. Lin, S. E. Shelton, D. Espíndola, J. D. Rojas, G. Pinton, and P. A. Dayton, “3-d ultrasound localization microscopy for identifying microvascular morphology features of tumor angiogenesis at a resolution beyond the diffraction limit of conventional ultrasound,” *Theranostics*, vol. 7, no. 1, pp. 196–204, 2017.

[63] S. Harput, K. Christensen-Jeffries, J. Brown, Y. Li, K. J. Williams, A. H. Davies, R. J. Eckersley, C. Dunsby, and M.-X. Tang, “Two-stage motion correction for super-resolution ultrasound imaging in human lower limb,” *IEEE Transactions on Ultrasonics, Ferroelectrics, and Frequency Control*, vol. 65, no. 5, pp. 803–814, 2018.

[64] C. Demené, J. Robin, A. Dizeux, B. Heiles, M. Pernot, M. Tanter, and F. Perren, “Transcranial ultrafast ultrasound localization microscopy of brain vasculature in patients,” *Nature Biomedical Engineering*, vol. 5, pp. 219—-228, 2021.

[65] B. Heiles, A. Chavignon, A. Bergel, V. Hingot, H. Serroune, D. Maresca, S. Pezet, M. Pernot, M. Tanter, and O. Couture, “Volumetric ultrasound localization microscopy of the whole brain microvasculature,” *bioRxiv*, 2021.

[66] O. Demeulenaere, A. Bertolo, S. Pezet, N. Ialy-Radio, B. Osmanski, C. Papadacci, M. Tanter, T. Deffieux, and M. Pernot, “In vivo whole brain microvascular imaging in mice using transcranial 3d ultrasound localization microscopy,” *eBioMedicine*, vol. 79, p. 103995, 2022.

[67] N. Blanken, J. M. Wolterink, H. Delingette, C. Brune, M. Versluis, and G. Lajoinie, “Super-resolved microbubble localization in single-channel ultrasound rf signals using deep learning,” *IEEE Transactions on Medical Imaging*, pp. 1–1, 2022.

[68] M. Zamir, *Physics of pulsatile flow.* Springer New York, 2000.

[69] J. Womersley, “Method for the calculation of velocity, rate of flow and viscous drag in arteries when the pressure gradient is known,” *The Journal of Physiology*, vol. 127, pp. 553–563, 1955.

[70] R. Parthasarathy, “Rapid, accurate particle tracking by calculation of radial symmetry centers,” *Nature Methods*, vol. 9, no. 7, pp. 724–728, 2012.

[71] C. G. Caro, T. Pedley, R. Schroter, and W. Seed, *The mechanics of the circulation.* Cambridge University Press, 2012.

[72] S. S. Segal, “Regulation of blood flow in the microcirculation,” *Microcirculation*, vol. 12, no. 1, pp. 33–45, 2005.

[73] M. Wang, C. V. Krishna, M. Luhar, and M. S. Hemati, “Model-based multi-sensor fusion for reconstructing wall-bounded turbulence,” *Theoretical and Computational Fluid Dynamics*, no. 35, pp. 683–707, 2021.

[74] O. Ronneberger, P. Fischer, and T. Brox, “U-net: Convolutional networks for biomedical image segmentation,” in *Medical Image Computing and Computer-Assisted Intervention – MICCAI 2015* (N. Navab, J. Hornegger, W. M. Wells, and A. F. Frangi, eds.), (Cham), pp. 234–241, Springer International Publishing, 2015.

Glossary

List of Acronyms

ULM	Ultrasound Localization Microscopy
MB	microbubble
SNR	signal to noise ratio
RF	radio frequency
FOV	field of view
VRUS	Verasonics Research Ultrasound Simulator
fUS	functional ultrasound imaging
PSF	point spread function
SVD	singular value decomposition
MLD	maximum linking distance

List of Symbols

Δl	MB localization error in l (in m)
$\Delta u_n^{\mathrm{f}}(r)$	Error in smoothed velocity measurement induced by localization error (in m)
$\Delta u_n(r)$	Error in raw velocity measurement induced by localization error (in m/s)
Δx	MB localization error in x (in m)
Δz	MB localization error in z (in m)
$\hat{x}$	Estimated x-coordinate of MB position (in m)
$\hat{z}$	Estimated z-coordinate of MB position (in m)
λ	Wavelength (in m)
λ	Wavelength (in m)
μ_x	Mean of localization error in x (in m)
μ_z	Mean of localization error in z (in m)

σ	Induced localization precision for simulation in the No-Localization scenario (equal in x and z) (in m)
σ_x	Found localization precision in x (in m)
σ_z	Found localization precision in z (in m)
σ_u	Derived standard deviation of $\Delta u_n^{\mathrm{f}}(r)$ (in m)
θ	Vessel or blood flow orientation w.r.t. the x-axis (CCW) (in rad)
c	Speed of sound (in m/s)
d	Vessel diameter (in m)
dt	Timestep between two B-mode frames (in s)
dx	Beamformed pixel size (in m)
f	Transmit frequency (in Hz)
f_{dx}	Frequency range corresponding to a MB passing beamformed pixels (in Hz)
L	Vessel length (in m)
l	Axial local coordinate (in m)
n	Time index or frame number
P_f	Pulsatility fraction
r	Lateral local coordinate (in m)
s	Span of moving average filter (in number of frames)
$u_n^{\mathrm{f}}(r)$	Filtered velocity measurement (in m/s)
$u_n^{\mathrm{GTf}}(r)$	Filtered ground truth flow (in m/s)
$u^{\mathrm{GTss}}(r)$	Ground truth flow for steady-state scenario (in m/s)
$u_n^{\mathrm{GT}}(r)$	Ground truth flow (in m/s)
$u_n(r)$	Raw velocity measurement (in m/s)
x	Coordinate parallel to tissue surface (in m)
z	Coordinate perpendicular to tissue surface (in m)